BremHLR

Kompetenzzentrum für Höchstleistungsrechnen Bremen

Statusbericht 2015

des

Kompetenzzentrums

für

Höchstleistungsrechnen Bremen

–BremHLR–

Bremen, Juni 2016

Universität Bremen

JACOBS UNIVERSITY

ALFRED-WEGENER-INSTITUT HELMHOLTZ-ZENTRUM FÜR POLAR- UND MEERESFORSCHUNG

Hochschule Bremerhaven

HLRN

Norddeutscher Verbund für Hoch- und Höchstleistungsrechnen

www.bremhlr.uni-bremen.de

Das Berichtsjahr 2015 in Stichpunkten

- Weitere Steigerung der Bremer Nutzung der Computer des Norddeutschen Verbunds für Hoch- und Höchstleistungsrechnen(HLRN)
- 10. Workshop zur Einführung in die parallele Programmierung
- Stabiler Produktionsbetrieb des Rechnersystems HLRN-III

Inhaltsverzeichnis

1 BremHLR: Aufgaben und organisatorische Struktur

1.1 Aufgaben

Das Land Bremen beteiligt sich am Norddeutschen Verbund für Hoch- und Höchstleistungsrechnen – HLRN – um an dem rasanten Fortschritt der Computer- und Softwaretechnologie Teil zu haben. Das Kompetenzzentrum für Höchstleistungsrechnen Bremen – BremHLR – unterstützt dazu Wissenschaftler im wissenschaftlichen Rechnen insbesondere im Land Bremen. Die Fachberater des BremHLR leisten Unterstützung für Projekte sowohl in der Konzeption, der Antragstellung als auch der Durchführung. Der Schwerpunkt der Unterstützung liegt hierbei auf Projekten auf dem HLRN-System. Seit 2005 wurde die Betreuung aber auch auf Rechenprojekte an den nationalen Höchstleistungsrechenzentren wie z. B. dem Jülich Supercomputing Centre (JSC) ausgeweitet.

Als Bestandteil im Kompetenznetzwerk des HLRN beteiligt sich BremHLR unter anderem an der fachspezifischen Nutzerberatung, der Pflege von Software-Paketen und der Veranstaltung überregionaler Nutzerworkshops. Die Geschäftsstelle des BremHLR ist an der Universität Bremen im Zentrum für Technomathematik angesiedelt.

Das BremHLR wurde am 1. Juli 2003 als Kooperation zwischen der Universität Bremen (UB), der Jacobs University Bremen (JUB) und dem Alfred-Wegener-Institut für Polar- und Meeresforschung (AWI) gegründet. Seit April 2008 ist auch die Hochschule Bremerhaven (HBHV) Kooperationspartner des BremHLR. Das Kompetenzzentrum wird von den beteiligten Kooperationspartnern sowie der Bremer Senatorin für Bildung und Wissenschaft (SfBW) anteilig finanziell getragen. Seit Januar 2014 ist die JUB als ideelles Mitglied beitragsfrei gestellt.

1.2 Struktur

Dem Lenkungsausschuss des BremHLR als oberstes beschlussfassendes und steuerndes Gremium gehören in der Berichtsperiode folgende Vertreter der kooperierenden Einrichtungen an. Im Einzelnen sind dies:

- Prof. Dr. Alfred Schmidt (UB/Zentrum für Technomathematik ZeTeM)
- Prof. Dr. Wolfgang Hiller (AWI/Rechenzentrum)
- Prof. Dr. Ulrich Kleinekathöfer (JUB)
- Prof. Dr. Stephan Frickenhaus (HBHV)
- Helmuth Wolf (SfBW)

Die fachspezifische Betreuung der Projekte am Norddeutschen Verbund für Hoch- und Höchstleistungsrechnen (HLRN) sowie von Projekten an anderen nationalen Höchstleistungsrechenzentren wird von den Fachberatern des BremHLR geleistet, die ebenfalls den Einrichtungen der Kooperationspartner angehören. Im Berichtszeitraum waren folgende Fachberater tätig:

- Dr. Lars Nerger (AWI/Rechenzentrum, UB/ZeTeM, Leiter Geschäftsstelle)
- Thorsten Coordes (UB/ZARM)
- Dr. Achim Geleßus (JUB/CLAMV)
- Dr. Natalja Rakowsky (AWI/Rechenzentrum)
- Dr. Dirk Barbi (AWI/Rechenzentrum)

Die Geschäftsstelle ist verantwortlich für die Organisation der Workshops (siehe Abschnitt Veranstaltungen) und die Unterstützung der Nutzer, insbesondere im Antragsverfahren. Das Sekretariat der Geschäftsstelle wird betreut von

- Julitta von Deetzen.

2 Tätigkeitsprofil des BremHLR im Berichtszeitraum

2.1 Unterstützung der HLRN-Nutzung im Land Bremen

Ein Schwerpunkt der Aktivitäten des BremHLR lag auch in diesem Berichtszeitraum in der Unterstützung der HLRN-Nutzung. Neben den Tätigkeiten von Prof. Dr. Wolfgang Hiller als Mitglied der Technischen Kommission sowie Prof. Dr. Alfred Schmidt als Mitglied des Wissenschaftlichen Ausschusses bestand die Unterstützung des HLRN durch das BremHLR hauptsächlich in der Fachberatung für Bremer Projekte am HLRN von der Antragstellung bis zur Begleitung rechenintensiver Projekte während der gesamten Projektlaufzeit.

Eine wesentliche Aufgabe im Berichtsjahr war die weitere Unterstützung der Bremer Nutzer des HLRN bei der effizienten Nutzung des HLRN-III Hochleistungsrechnersystems.

2.2 Weitere Aktivitäten des BremHLR

Im Veranstaltungsjahr 2015 wurde vom BremHLR der *10. Workshop zur Einführung in die parallele Programmierung mit MPI und OpenMP* organisiert und durchgeführt. Mit 24 Teilnehmern war dieser Workshop wieder sehr gut besucht. Mit dem gleichen Kursinhalt wurde im März 2015 ein Workshop an der Universität Bremen als Lehrveranstaltung im Fachbereich Mathematik/Informatik angeboten, der von 8 Teilnehmern besucht wurde.

Der Workshop wurde in der Zeit vom 12. bis zum 16. Januar 2015 an der JUB abgehalten. Als Referent konnte wie bereits bei bisherigen Workshops Dr. Hinnerk Stüben vom Regionalen Rechenzentrum der Universität Hamburg gewonnen werden, der den Workshop gemeinsam mit dem BremHLR-Fachberater Dr. Lars Nerger abhielt. Für die Studenten der JUB wurde der Workshop auch wieder als offizielle Lehrveranstaltung angeboten. Durch die Bearbeitung eines abschließend bewerteten Programmierprojekts konnten die Studenten Kreditpunkte für ihr Bachelor- und Masterstudium erlangen.

Der sehr gute Zuspruch und der große Erfolg der Veranstaltungen zeigt deutlich den dringenden Bedarf zur Ausbildung im Hoch- und Höchstleistungsrechnen und gibt Anlass dazu solche Workshops auch weiterhin als regelmäßige Ausbildungs- und Schulungsmaßnahme anzubieten.

Neben dem Workshop zur Einführung in die parallele Programmierungbeteiligten sich Fachberater des BremHLR an einem mehrtägigem Workshop zur optimalen Nutzung der Cray-MPP-Komponente des HLRN-III in Hannnover. Weiterhin beteiligten sich die Fachberater an Fachberaterworkshops des HLRN-Kompetenznetzwerks in Kiel und Warnemünde. Bei diesen Workshops wurden unterschiedliche Themen des HLRN-Betriebs und der Nutzerbetreuung besprochen. Eine Übersicht über die Veranstaltungen ist in Abschnitt 4 zu finden.

Des Weiteren waren Mitglieder des BremHLR an der Diskussion zu einem HPC-Konzept der Universität Bremen beteiligt.

3 Statistische Angaben zu den Bremer Höchstleistungsprojekten

Auch im Jahr 2015 wurde der HLRN intensiv durch Bremer Projekte genutzt. Im Jahresdurchschnitt wurde auf dem HLRN-III System ein prozentualer Anteil von 11,9 % an der gesamten am HLRN-III abgenommenen Rechenleistung erreicht. Dieses liegt deutlich über dem investiven Anteil von etwa 3,5% des Landes Bremen am HLRN. Über die gesamte Laufzeit seit Einrichtung des HLRN-Verbunds wurde durch Bremer Projekte ein Anteil von 6,5% der verfügbaren Rechenzeit abgenomen.

Nach den Anfangsproblemen nach der Installation des HLRN-III Systems im September 2013 und einer längeren Ausfallzeit während und nach der Installation der zweiten Ausbaustufe des HLRN-III Systems im vierten Quartal 2014 war das Jahr 2015 durch einen stabilen Betrieb des HLRN-III Systems ohne längere Ausfallzeiten geprägt.

Insgesamt wurden im Jahr 2015 etwa 4.563.000 NPL[1] durch Bremer Projekte am HLRN-III System abgenommen. **Dieses ist die größte Nutzung seit Einrichtung des HLRN-Verbunds.** Abbildung 3.1 zeigt den monatlichen Verbrauch der Bremer Projekte an den HLRN-II und HLRN-III Systemen. Deutlich sichbar ist die starke Zunahme der genutzen Rechenzeit im Jahr 2015 die durch die Verfügbarkeit der zweiten Ausbaustufe von HLRN-III möglich wurde.

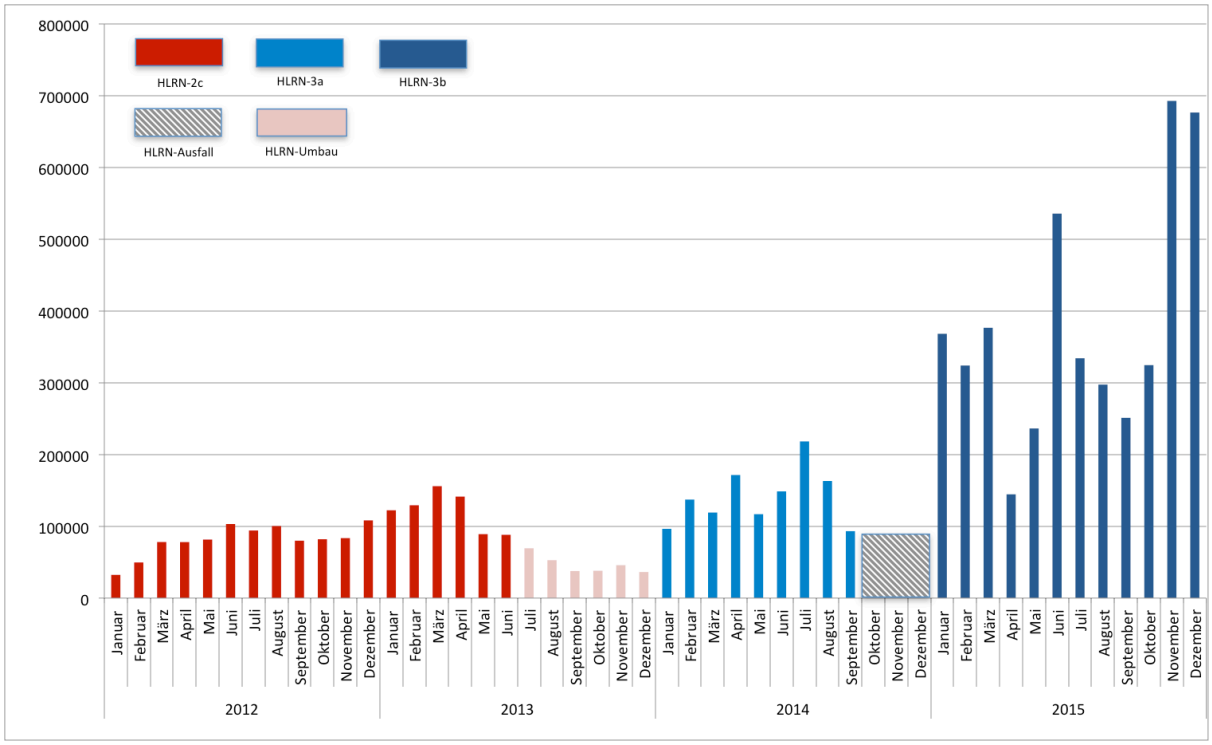

Abbildung 3.1: Grafische Darstellung der monatlichen Rechenzeitnutzung der Bremer HLRN-Großprojekte auf den HLRN-II (bis Dezember 2013) und seit Januar 2014 HLRN-III Systemen in der HLRN-Leistungseinheit NPL. Die Farben zeigen die Verfügbarkeit der unterschiedlichen Ausbaustufen der HLRN-Systeme. Von Oktober bis Dezember 2014 waren die HLRN-Systeme nicht bzw. nur teilweise nutzbar.Von Juli bis Dezember 2013 kam es zu Einschränkungen durch den Aufbau des neuen HLRN-III Systems.

[1]Norddeutsche Parallelrechner-Leistungseinheit: Auf den Systemen der ersten Ausbaustufe des HLRN-III entspricht 1 NPL einer halben CPU-h auf einem Knoten mit je 24 Prozessorkernen.

Eine Übersicht zu allen vom BremHLR betreuten Projekten gibt Tabelle 3.1. Im Jahr 2014 wurden vom BremHLR 34 Projekte am HLRN betreut. Die Projekte werden von etwa 100 akkreditierten Nutzern durchgeführt. 13 neue Projekte mit teilweise sehr großem Rechenzeitbedarf wurden im Jahr 2014beantragt und vom Wissenschaftlichen Ausschuss des HLRN bewilligt. Acht Projekte wurden im Berichtsjahr beendet.

4 Veranstaltungen mit Beteiligung des BremHLR

10. BremHLR-Workshop *Einführung in die Programmierung mit MPI und OpenMP*

Veranstalter: BremHLR

Datum: 12. – 16. Januar 2015

Ort: Jacobs University Bremen

Beschreibung: In dem Workshop wurden die Grundlagen der parallelen Programmierung vermittelt. Der Schwerpunkt lag auf den Programmiermodellen MPI und OpenMP. Praktische Übungen bildeten einen wesentlichen Teil des Workshops.

Referenten: Dr. Hinnerk Stüben (Regionales Rechenzentrum der Universität Hamburg) und Dr. Lars Nerger (BremHLR).

Teilnehmerzahl: 24

Teilnehmende Institutionen: AWI, JUB, HS Bremen, UB (BIPS, IUP, Physik, PPEP, ZeTeM)

27. HLRN-Fachberater-Workshop

Veranstalter: Rechenzentrum Universität Kiel

Datum: 4. – 5. Mai 2015

Ort: Universität Kiel

Teilnehmerzahl: 15

Teilnehmende Institutionen: BremHLR (ZARM), BTU Cottbus - Senftenberg, Cray Inc., HU Berlin, IOW, LUIS Uni Hannover, RZ Uni Hamburg, RZ Uni Kiel, TU Braunschweig, ZIB

28. HLRN-Fachberater-Workshop

Veranstalter: Institut für Ostseeforschung (IOW) Warnemünde

Datum: 24. – 25. November 2015

Ort: IOW Warnemünde

Teilnehmerzahl: 27

Teilnehmende Institutionen: BremHLR (AWI, ZARM), BTU Cottbus - Senftenberg, Cray Inc., GWDG Göttingen, HU Berlin, IOW, LUIS Uni Hannover, RZ Uni Hamburg, RZ Uni Kiel, Uni Oldenburg, Uni Potsdam, Uni Rostock, ZIB

Tabelle 3.1: Übersicht der Bremer HPC-Projekte, die innerhalb des Berichtszeitraums vom BremHLR betreut wurden. Status: F = Fortsetzung, E = Erstantrag; NPL: Kontingent in NPL im Jahr 2015

Kennung	Projektleiter	Institut	Laufzeit	NPL	Status
hbc00011	Prof. Dr. P. Deák	UB/BCCMS	II/12 – III/15	105000	F
hbc00012	Prof. Dr. L. Colombi-Ciacchi	UB/BCCMS	IV/12 – IV/16	45670	F
hbc00013	Dr. J. Larrucea	UB/BCCMS	IV/12 – IV/16	90000	F
hbc00014	Prof. Dr. L. Colombi-Ciacchi	UB/BCCMS	IV/13 – II/16	327000	F
hbc00015	Dr. M. Fischer	UB/FB 5	II/15 – I/16	77932	E
hbc00016	Dr. S. Köppen	UB/BCCMS	II/15 – I/16	133215	E
hbc00017	Prof. Dr. P. Deák	UB/BCCMS	IV/15 – III/16	45000	E
hbi00024	Dr.-Ing. R. Groll	UB/ZARM	II/14 – II/16	181000	F
hbi00025	Prof. Dr. U. Fritsching	UB/FB 4	IV/14 – III/15	22000	E
hbi00026	Dr.-Ing. R. Groll	UB/ZARM	II/15 – I/16	107885	E
hbi00027	Dr.-Ing. R. Groll	UB/ZARM	IV/15 – III/16	32000	E
hbk00018	Dr. K. Weigel	UB/IUP	I/11 – IV/16	29000	F
hbk00021	Prof. Dr. T. Jung	AWI &UB	II/09 – III/15	150000	F
hbk00028	Prof. Dr. P. Lemke	AWI & UB	IV/11 – I/16	60000	F
hbk00032	Prof. Dr. T. Jung	AWI & UB	II/12 – II/16	1031770	F
hbk00034	Prof. Dr. T Kanzow	AWI & UB	III/13 – III/16	482092	F
hbk00037	Prof. Dr. M. Schulz	UB/MARUM	III/14 – IV/15	245000	E
hbk00038	Prof. Dr. T. Kanzow	AWI & UB	III/14 – III/16	131000	F
hbk00039	Prof. Dr. M. Schulz	UB/MARUM	III/14 – III/15	45000	E
hbk00040	Prof. Dr. T. Jung	AWI & UB	III/14 – II/16	347488	F
hbk00041	Prof. Dr. W. Hiller	AWI & UB	IV/14 – IV/15	188000	E
hbk00042	Prof. Dr. G. Lohmann	AWI & UB	I/15 – IV/16	270369	E
hbk00044	Prof. Dr. T. Jung	AWI & UB	II/15 – III/16	302345	E
hbk00045	Dr. A. Rozanov	UB/IUP	IV/15 – I/16	260000	E
hbk00046	Prof. Dr. A Bracher	AWI & UB	IV/15 – III/16	19000	E
hbp00003	Prof. Dr. C. Lämmerzahl/ Prof. Dr. S. Rosswog	UB	IV/10 – IV/16	242000	F
hbp00019	Dr. P. Lorke	UB/BCCMS	IV/13 – IV/15	202447	F
hbp00021	Dr. L.-M. Yang	UB/BCCMS	IV/14 – I/16	160000	F
hbp00024	Prof. Dr. T. Wehling	UB/Physik	IV/14 – III/16	79000	F
hbp00027	Dr. L. Zhou	UB/BCCMS	I/15 – IV/15	241784	E
hbp00028	Prof. Dr. T. Frauenheim	UB/BCCMS	III/15 – II/16	94000	E
hbp00029	Dr. M. Lorke	UB/Physik	IV/15 – III/16	100000	E
hbp00030	Prof. Dr. T. Wehling	UB/Physik	IV/15 – III/16	44000	E

5 Informationen zur Infrastruktur: Das HLRN-III System im Endausbau

Das HLRN-III System wurde im September 2013 mit der ersten Ausbaustufe in Betrieb genommen und für die Nutzer geöffnet. Die zweite Ausbaustufe wurde ab September 2014 installiert und hat die verfügbare Rechenleistung um einen Faktor von etwa 3 vergrößert. Das neue HLRN-III System ist ein massiv paralleler (MPP) Hochleistungsrechner der Typen Cray XC30 und XC40. Ferner sind in Hannover 64 Rechenknoten des Herstellers MEGWARE mit großem Hauptspeicher installiert.

Das MPP-System der ersten Ausbaustufe besteht pro Standort aus:

- 744 Dual-Socket Knoten, jeweils mit Intel Xeon IvyBridge (E5-2695v2) Prozessoren mit 2,4 GHz Taktung und jeweils 12 Prozessorkernen
- 17856 Prozessorkerne pro Standort
- 64GB Hauptspeicher pro Knoten (46,5 TByte Gesamtspeicher)
- Netzwerk: Cray Aries Interconnect mit Dragonfly Topologie
- Peak-Performance: 342,8 TFlop/s
- 1,4 PB paralleles Lustre-Dateisystem (“WORK” zur Speicherung von Simulationsdaten) über FDR Infiniband-Netzwerk
- 0,5 PB Heimat-Dateisystem angebunden an die Knoten per NFS über 10 Gigabit-Ethernet Netzwerk.

Die MPP-Systeme der zweiten Ausbaustufe sind pro Standort leicht unterschiedlich ausgebaut:

- Rechenknoten:
  - Berlin: 1128 Dual-Socket Knoten, jeweils mit Intel Xeon Haswell (E5-2680v3) Prozessoren mit 2,4 GHz Taktung und jeweils 12 Prozessorkernen
  - Hannover: 936 Dual-Socket Knoten, jeweils mit Intel Xeon Haswell (E5-2680v3) Prozessoren mit 2,4 GHz Taktung und jeweils 12 Prozessorkernen
- Gesamtanzahl Prozessorkerne:
  - Berlin: 27072 Prozessorkerne
  - Hannover: 22464 Prozessorkerne
- 64GB Hauptspeicher pro Knoten:
  - Berlin: 117 TByte Gesamtspeicher
  - Hannover: 105 TByte
- Netzwerk: Cray Aries Interconnect mit Dragonfly Topologie
- Peak-Performance:
  - Berlin: 1,1PFlop/s
  - Hannover: 0,9 PFlop/s
- 2,3 PB paralleles Lustre-Dateisystem (“WORK” zur Speicherung von Simulationsdaten) über FDR Infiniband-Netzwerk

In Hannover wurde zusätzlich in der ersten und zweiten Ausbaustufe SMP-Systeme der Firma Megware mit großem RAM-Speicher installiert. Sie bestehen aus

- 1. Ausbaustufe:
  - 32 Quad-Socket Knoten mit Intel Xeon SandyBridge (E5-4650) Prozessoren mit 2,7 GHz Taktfrequenz und jeweils 8 Prozessorkernen
  - 256 GB Arbeitsspeicherpro Knoten
- 2. Ausbaustufe:
  - 32 Quad-Socket Knoten mit Intel Xeon IvyBridge (E5-4650v2) Prozessoren mit 2,4 GHz Taktfrequenz und jeweils 10 Prozessorkernen
  - 512 GB Arbeitsspeicherpro Knoten
- Dual FDR InfinibandNetzwerk

In der Top500 Liste der weltweit schnellsten Supercomputer vom November 2015 befinden sich die beiden MPP-Systeme auf den Plätzen 83 und 100. In Deutschland finden sich die beiden Systeme auf den Plätzen 9 und 10.

Abbildung 5.1: Frontansichten der Cray XC30/XC40 Systeme nach der zweiten Ausbaustufe des HLRN-III. Oben: System „Konrad“ am ZIB in Berlin; unten: System „Gottfried“ an der Universität Hannover

6 Projektberichte[2]

6.1 *hbc00011:* Theoretical investigation of luminescent defects in diamond

HLRNProject ID:	hbc00011
Run time:	II/2012 – III/2015
Project Leader:	Prof. Dr. Peter Deák
Project Scientists:	Dr. Bálint Aradi, Ms. Moloud Kaviani
Affiliation:	Bremen Center for Computational Materials Science University of Bremen

Overview

The development of low-pressure low-cost synthesis methods to produce diamond layers, and the detonation method to produce large quantities of nano-sized diamond particles, have made diamond available to many new applications. Diamond is not only very stable itself, it can have very stable crystal defects, too. Certain crystal defects of diamond emit strong visible light due to electronic transitions between different paramagnetic states. The magnetic states of remote defects can be entangled through optical excitation/recombination processes. Such systems near the diamond surface are today the most viably candidates to build an architecture of qubits forquantum computing. The light emitted by these defects is sensitive to external electric and magnetic fields, or to the chemical environment, and can be used for sensing at the nanoscale. Since such defects can also be produced in biocompatible diamonds of nanometer size, they can be used also for bio-labeling.

The so far most efficient color center in diamond is the NV(-) defect: a substitutional N atom next to a negatively charged vacancy (missing atom). The controlled production of such defects in high concentration and in appropriate charge state is crucial for all applications. While direct monitoring of the formation procedure is hardly possible, computer simulations may help to optimize the synthesis. The charge state of the defects is also influenced by interactions with the surface, since optically addressable qubits have to be near the surface and nanodiamonds are all but surfaces. These interactions can be investigated in detail also only by quantum mechanical calculations. Therefore, our project has addressed these two issues. In order to calculate the formation energy, chargestate, and optical spectrum of such systems, methods beyond standard density functional theory (DFT) are needed, and such calculations have to be carried out on models containing over 2000 valence electrons, making the use of super computers inevitable.

Results

The NV center has a low concentration in N-doped natural orsynthetic diamonds, due to the low vacancy (V) concentration. So the usual way to create the misirradiating N-doped diamond. A subsequent heat treatment heals irradiation defects (which would quench any

[2] Für den Inhalt der Projektberichte sind ausschließlich die genannten Projektleiter bzw. die Projektbearbeiter verantwortlich.

luminescence otherwise), and it was assumed that NV centers also arise during this process by substitutional N atoms capturing mobile V defects. We have calculated the ground state, charge transition levels, and the diffusion of the most important defects (N, V, NV, NVH, N_2, N_2V and V_2), which are expected to form in this process and may compete for an extra electron. We have used a 512-atom supercell as model and found good agreement between theory and experiment for the previously well-established data, and predicted missing ones. Based on the calculated properties of these defects we have concluded that the formation of the NV defects through the diffusion of V is unlikely. Instead, NV defects are predominantly created directly by irradiation, i.e., by creating a vacancy next to a substitutional N. Simultaneously produced vacancies form V_2 pairs during the post-irradiation annealing, and these outcompete the NV defect in acquiring the available extra electrons. Based on our results we were able to suggest the proper temperature range of annealing, which would produce a higher concentration of NV(-) defects. Our predictions have been confirmed experimentally (T. Yamamoto at al., Phys. Rev. B *90*, 08117(R) (2014); F F de Oliveira et al, Nano Letters, DOI: 10.1021/acs.nanolett. 5b04511). Our (yet unpublished) diffusion studies on nanodiamonds have corroborated that NV defects must form primarily during irradiation.

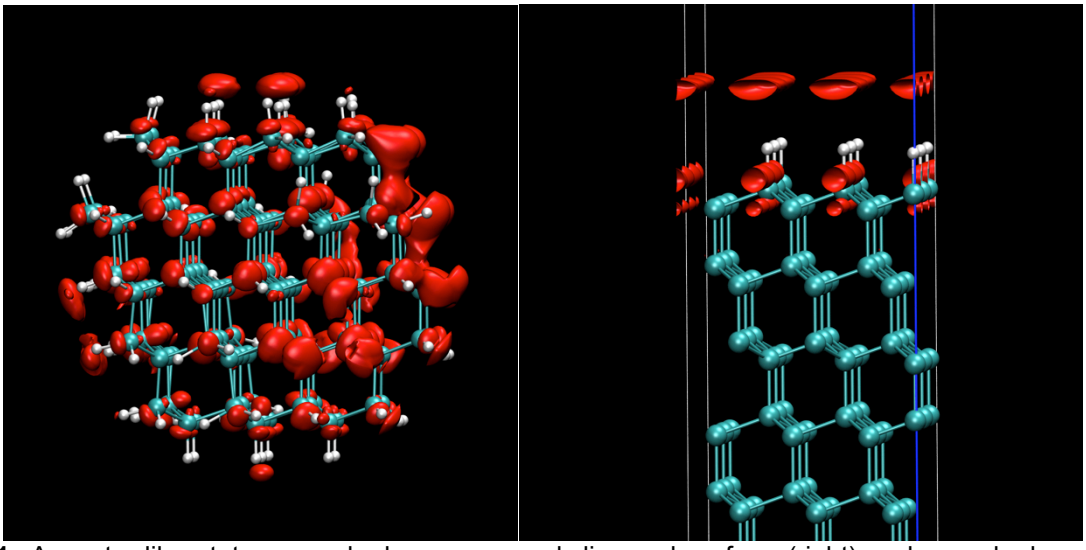

Fig.1: Acceptor-like states on a hydrogen-coeverd diamond surface (right) and on a hydrogenated nano-diamond (left).

Almost all applications of the NV(-) color centers require them to be very near the surface, where they can interact with surface states. Indeed, blinking and even bleaching of the luminescence has been observed, depending on the conditions of the surface. Our studies have shown that the most common surface terminations of diamond, hydrogenation or hydroxylation, lead to surface related empty states (Fig. 1) with negative electronaffinity. This leads to electron emission and loss of the luminescence, i.e., to bleaching. Highly oxidized or fluorinated surfaces, on the other hand, exhibit surface electron traps temporarily „shelving“ the electron of the NV(-) center after luminescence excitation. We have shown, that partial oxidation of a hydrogenated surface ensures positive electron affinity, no surface states, and so stable luminescence of the NV(-) defects.

Our results are also important for nano-diamonds applied in bio-labeling, because hydrogenation leads to the same surfacestates (Fig.1). We have also invetsigated the structural stability of nano-diamonds, and found that nano-diamonds with a core of only 0.8 nm can be kinetically stable up to 1500 K even in an oxygen-conatining environmeny. This is significantly less than the lower limit of the thermodynamic stability (~1.9 nm).

Outlook

Since the publication of our papers, we have been contacted by several experimental groups, asking for our opinion regarding new ways of creating stable NV(-) centers in high concentration. Following these discussions, we are now making calculations regarding the effect of doping on the NV formation, and on possibilities of surface doping to stabilize the negative charge state.

Publications

1. P. Deák, B. Aradi, M. Kaviani, T. Frauenheim, A. Gali, *The formation of NV centers in diamond: A theoretical study based on calculated transitions and migration of nitrogen and vacancy related defects,* Phys. Rev. B*, 89, 075203 (2014)*
2. M. Kaviani, P. Deák, B. Aradi, T. Frauenheim, J.-P. Chou, and A. Gali, *The proper surface termination for luminescent near-surface NV-centres in diamond*, Nano Letters *14*, 4772 (2014)
3. M. Kaviani, P. Deák, B. Aradi, T. Köhler, and T. Frauenheim, *How small nanodiamonds can be? MD study of the stability against graphitization,* Diam. Rel. Mater. *33*, 78 (2013)

Presentations

4. M. Kaviani, Oral presentation at the Spring Meeting of the European Materials Research Society, Symposium P: *Carbon materials: surface chemistry and biomedical applications*. Lille, May 26-30, 2014
5. M. Kaviani, Oral presentation at the International Conference of Diamond and Carbon Materials, Granada, Sept. 2-6, 2012
6. P. Deák, Invited talk at the 9th International Conference on Computational Physics, Symposium C5: *Computational Materials Science*, Singapore, January 7-11, 2015.
7. P. Deák, Invited talk at the international workshop GADEST, Bad Staffelstein, Sept. 20-25, 2015.

6.2 HLRN Projects of the Hybrid Materials Interfaces Group (HMI)

HLRN Project IDs: hbc00012, hbc00013, hbc00014, hbc00016

Runtimes: IV/2012-IV2015; IV/2012-IV/2016; IV/2013 – II/2016; II/2015-I/2016

Working on the projects: Jens Laube, Steffen Lid, Nils Hildebrand, Christian Perl, Susan Köppen, Lucio Colombi Ciacchi

Affiliation: Hybrid Materials Interfaces Group
Bremen Center for Computational Materials Science
Faculty of Production Engineering, University of Bremen, Germany

Motivation:

In the last decades the development of conventional basic materials has changed into complex materials consisting of anorganic and organical components. The combination of organic compound with classical metal or ceramics based materials can lead to optimized mechanical properties of the bulk (composite materials) as well as fine tuned properties of the materials surface (functionalized materials). However, the technical success or usage of such complex structures in any field of application strongly depends on the possibility of efficient fabrication pathways.

Independent from the macroscopic complexity of these materials, the first step to build up such structures is the interaction of the first two molecules. These molecules can be a water molecule adsorbed on a ceramics particle surface, a peptide or protein in contact with a metal oxide surface, two nano particles in a suspension or even Ions in aqueous particle solution.

In the Hybrid Materials Interfaces Group, we aim to solve the atomistic picture of such hybrid materials with the focus on the combination of the knowledge coming from the atomistic simulation with observations from experimental measurements. This toolbox gives us a strong instrument to understand interface processes sometimes beyond the textbook knowledge. In the following, recent results of the actual running “interface” projects will be highlighted.

Results:

In one of our projects (hbc00012) we aim to understand the mechanical behavior of TiO_2 nano particle films by extensive molecular dynamic (MD) and discrete element modeling (DEM) simulations in comparison to AFM force-spectroscopy and combined AFM/TEM experiments. In the first phases of that project, it could be estimated, that the particle particles contacts with a diameter below 10nm in humid air are crucially dominated by the nature of the surface adsorbed water shell (Figure 1, top) as well as In one of our projects (hbc00012) we the surface roughness and that the macroscopic adhesion force models have to be modified to account precisely for this effect [1,2]. In recent studies, these atomistic findings of the inter particle forces are transferred into a coarse grained inter particle contact model for the DEM simulation of entire nano particle films (Figure 1, middle). In atomistic simulation, this model has been validated against the mechanical behavior of entire nano

particle agglomerates, the results of AFM force spectroscopy and AFM/TEM experiments. In a next step, the application of this model should be used to investigate and improve a particle film lamination process, which is used for the fabrication of compact and stable nano particle films for sensor and catalytic technology (Figure 1, bottom).

In a second project (hbc00013), the growing of ferrihydrite crystals with the help of ferritin (Fn) subunits as a basis of 2D magnetic materials offered more than one interesting interfaces in a very complex system. In an earlier stage of this project, stable ferrihydrite structure and cluster models were established and parameterized for following force field simulations [3]. The next project phase focused on the ferritin subunit – iron oxide cluster interaction and significant protein – cluster contacts were determined. Extended simulations according the crystallization process are still in progress.

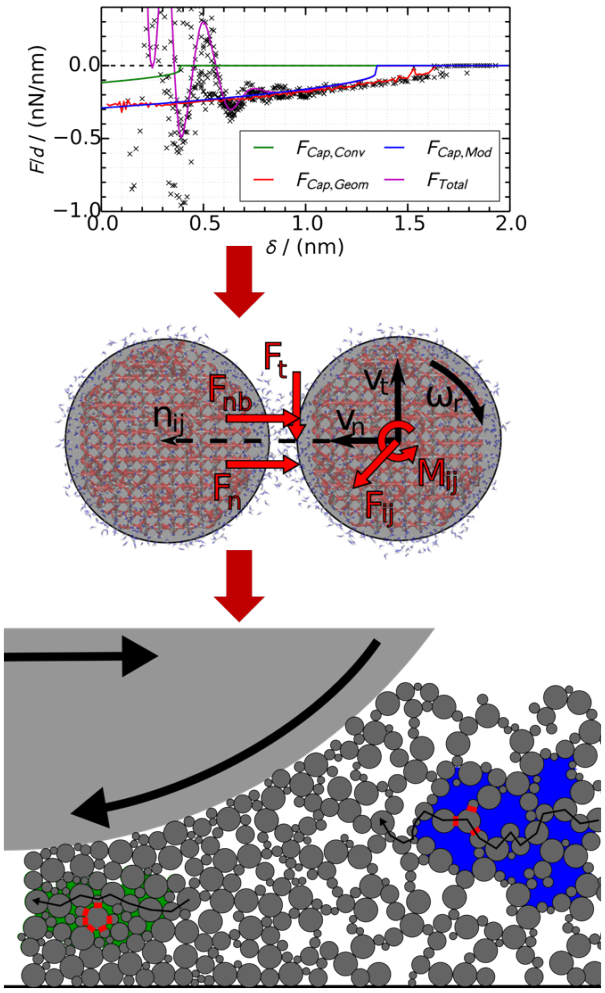

Figure 1: (top) comparison of the resulting capillary forces (blue line) added to water structure dependent solvation forces (purple line) to the computationally calculated interparticle forces from the same simulations (black crosses). **(middle)** Coarse graining approach from atomistic insights for the Discrete Element Modelling (DEM) simulation of the mechanic interactions between entire nanoparticles under ambient conditions. In the discrete model the share of the repulsive normal forces Fn, the non-bonding forces Fnb and the tangential forces Ft in the total interparticle forces have to be considered as well as the share of tangential forces and the rolling torque in the interparticle torque Mij. **(bottom)** Application of the DEM-simulations to investigate and improve the lamination process of nanoparticle films for the fabrication of compact and stable nanoparticle films in sensor and catalytic technology.

Furthermore, the interface of the protein subunits to a certain substrate material has been investigated on different substrate materials (SiO_2 and Al_2O_3). Detailed orientation analysis of different species of Fn subunits (which build up a protein cage for crystallization inside) revealed a slight preference of the so called outer sides (of the virtual protein cage) towards the silica surface (Figure 2). Nevertheless, the attractive forces between Fn subunits and silica are in the range of -5 pN in comparison with received forces of -20 or -60 pN between Chymotrypsin or Lysozyme and silica surfaces described in Ref. [4] which were also

calculated at the HLRN in project hbc00014. We concluded, the orientations of the outer side of the Fn subunits pointed to the surface to be energetically favorable but the received forces are too small for stable immobilization by physisorption. As a consequence, our experimental collaborators follow a route for covalent linked Fn subunits, now.

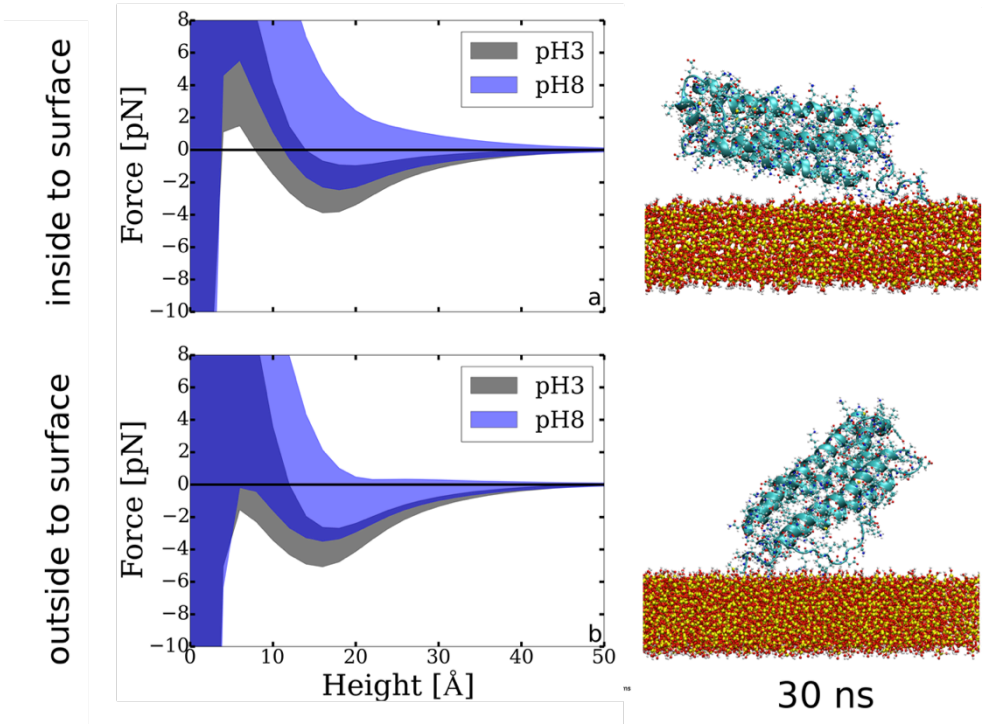

Figure 2: (left) interaction forces between H (top) and L (bottom)) ferritin subunits with an amorphous SiO2 surface model, **(right)** Snapshots of Fn subunits on a silica surface after 30 ns of molecular dynamics simulation

Another project focuses on the interplay of ceramic surfaces and two protein molecules, namely lysozyme and chymotrypsin (hbc00014). Previous studies reveal that chymotrypsin as a model enzyme adsorbs with its dipole moment facing a silica surface [4]. Furthermore the two helix structures are in direct contact with the surface in this adsorption orientation. The goal of the recent project phase is the development and evaluation of a simulation method to analyze possible surface-induced conformational changes of parts of proteins during adsorption on oxides. The well established enzyme-surface system is used for the investigations of the denaturation of the helices of chymotrypsin during adsorption on different metal oxide surfaces. A key question is if the denaturation affects the enzymes activity. The preserved protein activity is crucial for the usage of a technical enzyme functionalized surfaces.

In a preliminary first simulation the system temperature is increased to 500 K to accelerate the simulation and to overcome local barriers (Fig. 3 a). The interpretation of the performed classical molecular dynamics simulation at this temperature has to be taken with care. Still, they reveal first insights in more and less stable regions of the protein.

A more sophisticated simulation to capture the helix denaturation is a self consistent solute tempering replica exchange simulation in combinations with metadynamics [5]. The choice of a collective variable, in this case the helicity, allows a very effective sampling along this

variable. Whereas moderate unattached barriers are compensated by the solute tempering approach, the sampling efficiency increases in comparison to one of the advanced methods alone (Fig. 3 b)). The activity of the enzyme is rated by the distance change between the three amino acids involved in the native catalytic active site of the enzyme (Fig. 3 c) and d)).

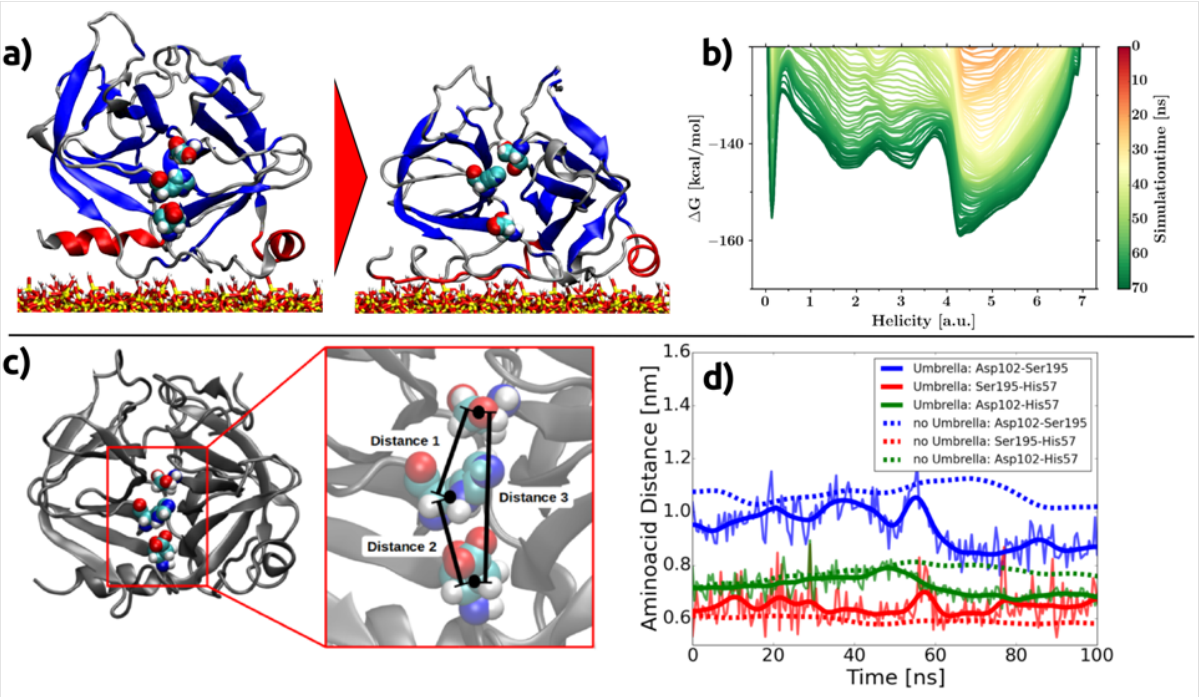

Figure 3: a) Adsorption induced denaturation of chymotrypsin on silica b) Free energy profile of one helix structure of chymotrypsin as a function of its helicity c) Active side of chymotrypsin including three amino acids highlighted in colored atom style d) The time evolution of the distances of the amino acids shown in c) are used as an indicator of the denaturation influence on the active side and therefore on the activity of the whole protein.

In a recent project (hbc00016), the same combination of advanced techniques has been used to determine stable conformations of adsorbed peptides which are known to be strong binders on certain metal oxide surfaces and being different from the native structure in solution. It turned out, that the degree of freedom for the favorable peptide structure is much higher than for proteins, which often have a specific energy landscape and minimum in its native state. However, only a few peptides show strong secondary structure motifs like alpha helix or beta sheet configuration. In most cases some unspecified coil structure is the dominated native state. The choice of the collective variable (CV) strongly influences the successes of these simulations, which has to end up in a converged energy profile. The helicity, which was the right choice for the project hbc00014, failed for coiled peptides. Therefore, in the recent project different possible CV's (helicity, radius of gyration, multi dimensional torsion angle combinations) have been tested first.

References:

[1] J. Laube, S. Salameh, M. Kappl, L. Mädler, L. Colombi Ciacchi, Contact forces between TiO2 nanoparticles governed by an interplay of adsorbed water layers and roughness, Langmuir 31, 11288-11295 (2015)

[2] S. Salameh, J. Schneider, J. Laube, A. Alessandrini, P. Facci, J. W. Seo, L. Colombi Ciacchi, L. Mädler, Adhesion mechanisms of the contact interface of TiO2 nanoparticles in films and aggregates, Langmuir 28, 11457-11464 (2012)

[3] J. Larrucea, S. Lid, L. Colombi Ciacchi, Parametrization of a classical force field for iron oxyhydroxide/water interfaces, Computational Materials Science 92, 343-352 (2014)

[4] Hildebrand, N.; Köppen, S.; Derr, L.; Li, K.; Koleini, M.; Rezwan, K.; Colombi Ciacchi, L., Adsorption orientation and binding motifs of lysozyme and chymotrypsin on amorphous silica. The Journal of Physical Chemistry C 119, 7295-7307 (2015)

[5] R.H Meißner, J. Schneider, P. Schiffels, L. Colombi Ciacchi, Computational prediction of circular dichroism spectra and quantification of helicity loss upon peptide adsorption on silica Langmuir 30, 3487-3494 (2014)

Funding:

The project **hbc00012** (“All-atom moleculardynamic investigations of the adhesion mechanisms at the contact interface of TiO2 nanoparticles in films and aggregates “) will be worked out within the framework of the DFG priority program SPP 1486 "Partikel im Kontakt (PIKO) – Mikromechanik, Mikroprozessdynamik und Partikelkollektive". The project **hbc00013** (“Fabrication of 2D magnetic nanostructures via a knowledge-based biomimetic approach”) is embedded within the framework of the DFG priority programme SPP 1569, entitled: “Generation of multifunctional inorganic materials by molecular bionics”. The project **hbc00014** (“Molecular Dynamic Simulations of the Adsorption of Lysozyme and Chymotrypsin on Silica and Titania: Conformational changes in proteins by adsorption on oxides using classical molecular dynamics”) is funded by the DFG with the project ID: KO3811/3-1 and is entitled “Theoretical investigation of the adsorption of lysozyme on different oxide materials for the development of antibacterial hybrid materials”. The HLRN provides computational resources for several projects in the hybrid materials interfaces group in the **magnitude of 2000 kCPU-hours/year**.

6.3 *hbc00015:* Structure and dynamics of ammonium cations in NH_4-exchanged zeolites

HLRNProject ID:	hbc00015
Run time:	II/2015 – I/2016
Project Leader:	Dr. Michael Fischer
Project Scientists:	Dr. Iris Spieß, Prof. Dr. Reinhard X. Fischer
Affiliation:	Fachgebiet Kristallographie, Fachbereich Geowissenschaften, Universität Bremen

Overview

In this project, the behavior of ammonium cations (NH_4^+) in zeolites is studied with molecular dynamics calculations based on density-functional theory (DFT). A particular emphasis is placed on the development of an atomistic explanation for the observed instability of NH_4-exchanged zeolite LTA towards deammoniation.

Introduction

Zeolites are crystalline inorganic materials with intrinsic porosity which have found a number of technological applications, e.g. in catalysis, adsorption, and ion exchange. Structurally, zeolites consist of a three-dimensional framework of tetrahedrally coordinated atoms (T atoms, primarily silicon and aluminium), which are connected by oxygen atoms. More than 200 different zeolite frameworks have been reported to date, with each topologically distinct system being designated by a three-letter code like LTA, FAU, or RHO. In most cases, the zeolite framework is negatively charged, and the structure contains extra-framework cations to balance the charge.

Ammonium-exchanged zeolites (NH_4-zeolites) are of particular interest as precursor materials for the production of protonated zeolites (H-zeolites). H-zeolites are very important catalysts that are employed on an industrial scale in a variety of processes, e.g. in the fluid catalytic cracking of heavier oil fractions to produce lighter hydrocarbons.[1] The crystal structures of approximately twenty NH_4-zeolites with distinct framework topologies have been reported.[2] It has been found that structurally different systems differ considerably in their behaviour upon the removal of the ammonium cations from the structure (deammoniation): For example, deammoniation of NH_4-RHO at high temperatures produces highly crystalline H-RHO,[3] whereas fully ammonium-exchanged LTA is unstable towards deammoniation.[4]

Motivation and computational approach

Current experimental efforts in our group aim at a detailed characterisation of the deammoniation behaviour of partially and fully ammonium-exchanged LTA, as well as some other NH_4-zeolites (e.g. chabazite, merlinoite). The portfolio of experimental methods comprises X-ray diffraction using single crystal and powder samples, thermal analysis, and spectroscopic measurements. Our investigations have corroborated the previously observed instability of NH_4-LTA towards deammoniation, with amorphisation occurring at moderate temperatures.

Since none of the experimental methods can deliver direct insights into the structural changes that occur upon deammoniation, computational chemistry methods are used in this project to develop an atomic-level understanding of the underlying processes. The calculations are performed in the framework of density-functional theory (DFT). DFT has developed into a powerful and versatile electronic structure method that is particularly well suited for the treatment of periodic systems. With efficient DFT codes like the program CP2K, which is used in this project, systems that contain thousands of atoms per unit cell can be treated when using high-performance computing facilities.[5]

The calculations carried out within the project focused on two different zeolites, zeolite LTA and zeolite RHO. The structure of LTA contains larger *grc* cages, connected by windows formed of eight T atoms (eight-ring windows), and smaller *toc* cages, bordered by six-ring windows. In zeolite RHO, *grc* cages are connected by double-eight-ring units (Fig. 1). Along with fully ammonium-exchanged LTA (NH_4-LTA), potassium-exchanged LTA (K-LTA) was studied as reference system. Furthermore, a (hypothetical) model of protonated LTA was constructed (H-LTA), and the energetically most favourable proton position was determined from structure optimisations of different models (the oxygen atom to which the proton is attached is referred to as O_H). Additional calculations consideredammonium-exchanged and protonated zeolite RHO (NH_4-RHO and H-RHO).To start with, DFT structure optimisations were performed for systems with and without adsorbed water molecules. In the following, DFT-based Molecular Dynamics (MD) calculations were run for temperatures of 100 K, 298 K, and 500 K (total duration 5 ps, timestep 0.5 fs) in order to model the dynamic behavior of these systems.

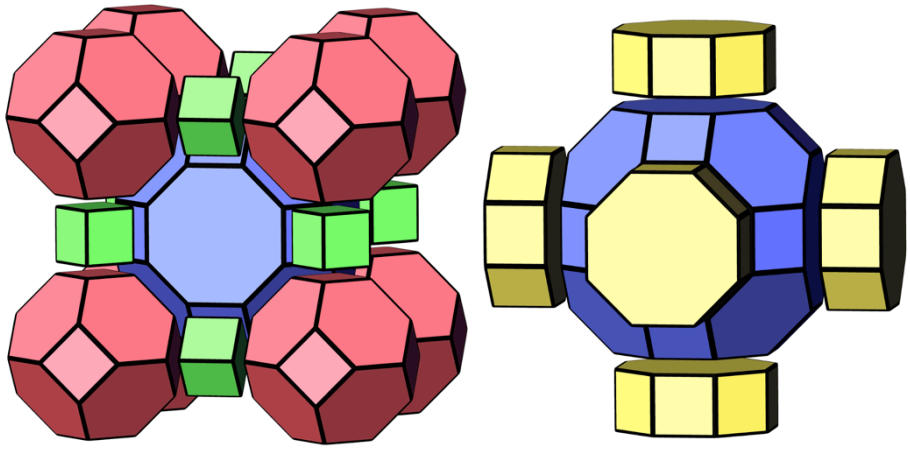

Fig. 1: Natural tiling representation of LTA (left) and RHO (right) frameworks. The *grc* cages are shown in blue, *toc* cages are shown in red, double four-ring units are green and double eight-ring units are yellow. The full unit cell of LTA used in the simulations contains a 2x2x2 array of *grc* cages.

Results

The comparative MD simulations for water-free models of NH_4-LTA and NH_4-RHO reveal a much higher mobility of the cations in the former system: While the ammonium cations in NH_4-RHO mainly oscillate about their equilibrium positions, the cations in NH_4-LTA exhibit a larger freedom of movement. During the simulation run performed for the highest temperature (500 K), some of the ammonium cations in NH_4-LTA dissociate into a framework proton and an ammonia (NH_3) molecule. Such dissociation constitutes the first step of deammoniation, which would then be followed by the diffusion of ammonia molecules out of the structure (however, this second step is not accessible with the current modelling strategy). In NH_4-RHO, no dissociation is observed at the timescale of the simulation, even at

a temperature of 500 K. This is in accordance with the rather high temperatures needed for the deammoniation of this material (which are in the range of 700 to 1000 K).[3]

In the simulations for water-free models of LTA, no breaking of T-O bonds (intra-framework bonds) is observed throughout the MD simulations: The T-O bond lengths oscillate about their equilibrium value due to thermal motion, but no exceptionally large elongation occurs. Even at an elevated temperature of 500 K, thewater-free form of H-LTA should be stable according to the MD simulations. At first sight, this observation appears to be in disagreement with the experimentally observed instability of NH_4-LTA towards deammoniation. However, it has to be considered that an as-synthesised sample of NH_4-LTA will also contain water, and that the presence of water might promote the amorphisation upon ammonia removal. To study the effect of water in more detail, additional MD simulations were run for models of K-LTA, NH_4-LTA, and H-LTA with 96 water molecules per unit cell (equivalent to 12 molecules per *grc* cage). For K-LTA and NH_4-LTA, no breaking of intra-framework bonds is observed. For H-LTA, the first set of simulations was run for a model in which water is located exclusively in the large *grc* cages. Again, no unusual elongation of the T-O bonds occurred. However, simulations for a second model, in which some of the water molecules were placed in the smaller *toc* cages, showed a completely different behavior: Here, some of the water molecules located at the inside of the *toc* cages coordinate to framework aluminiumatoms. Concomitantly, one of the Al-O intra-framework bonds, more specifically the bond to the oxygen atom that carries the framework proton (Al-O_H bond), is strongly elongated. In many cases, the Al-O_H distance becomes so large that the bond can be considered as broken. The breaking of Al-O_H bonds is accompanied by a reorientation of the framework proton, which tends to form an intra-framework hydrogen bond. A representative example is shown in Fig. 2. As is visible in this figure, the whole structural environment is strongly distorted after the H_2O-Al coordination has occurred. This distortion can be interpreted as the very onset of the amorphisation of the structure, which would be observed on a longer timescale.

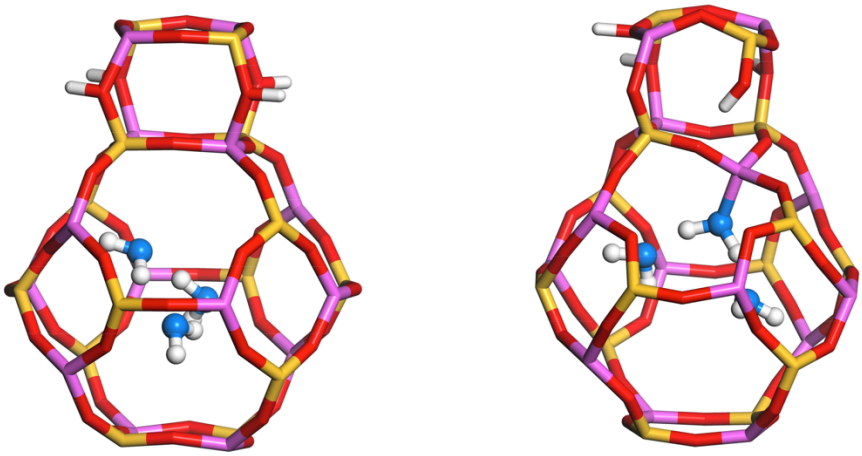

Fig. 2: Visualisation of a water-containing*toc* cage in H-LTA at the beginning of an MD run (left) and after a run of 5 ps (right). The coordination of one water molecule to a framework Al atom, with the concomitant breaking of the Al-O_H bond and reorientation of the framework proton, is clearly visible in the upper right-hand corner.

While the MD simulations as such cannot model the full process of the structural decomposition of NH_4-LTA upon deammoniation, they help to propose a model that is based on two central steps:

1) Initially, some of the NH_4 cations dissociate into framework protons and ammonia molecules. The presence of framework protons is a prerequisite for step 2.
2) If water is present in the small *toc* cages, some of the water molecules will coordinate to framework aluminium atoms, provided that these are also bonded to an O_H oxygen atom. Upon formation of the H_2O-Al bond, the Al-O_H bond is broken, leading to severe structural distortions.

With increasing temperature, the probability of both steps increases, explaining – at least qualitatively – the observed amorphisation of NH_4-LTA upon heating to relatively mild temperatures.

In zeolite H-RHO, no significant elongation of the intra-framework bonds is observed, even in the presence of 12 water molecules per unit cell. This finding points to a rather high stability of the deammoniated zeolite, in line with experimental observations.

Outlook

In addition to the different topology of LTA and RHO, the models used for the two zeolites also have different Si:Al ratios. While the LTA models contain equal amounts of silicon and aluminium, RHO has an Si:Al ratio of 3:1. Therefore, H-LTA contains a considerably larger number of protons (per formula unit) than H-RHO. The present study points to a crucial role of the topology, as only water molecules confined to the small toc cages in LTA are observed to coordinate to framework Al atoms. However, an additional impact of the Si:Al ratio cannot be ruled out on the basis of the present results. Therefore, a subsequent study that includes a series of models of LTA with different Si:Al ratios could be envisaged for future work.

Additionally, it is planned to extend the present study to other ammonium-exchanged that are currently investigated in our lab (chabazite, merlinoite) once a complete solution of the structure from experimental data has been accomplished.

Presentations

I. Spieß, M. Fischer, L. Wang, W. H. Baur, R. X. Fischer, Crystallographic characterization and thermal decomposition behavior of ammonium exchanged zeolites, presented at the 24th Annual Meeting of the German Crystallographic Society (DGK), Stuttgart, March 2016

References

(1) Rabo, J. A.; Schoonover, M. W. *Appl. Catal. A***2001**, *222*, 261–275.

(2) Baur, W. H.; Fischer, R. X. In *Proc. 16th Int. Zeolite Conf.*; De Frede, A., (Editor); Sorrento, Italy, 2010.

(3) Fischer, R. X.; Baur, W. H.; Shannon, R. D.; Staley, R. H.; Vega, A. J.; Abrams, L.; Prince, E. *J. Phys. Chem.***1986**, *90*, 4414–4423.

(4) Kühl, G. H. *J. Catal.***1973**, *29*, 270–277.

(5) Hutter, J.; Iannuzzi, M.; Schiffmann, F.; VandeVondele, J. *WIREs Comput. Mol. Sci.***2014**, *4*, 15–25.

6.4 *hbi00024:* 3D Simulation einer kompressiblen Edelgasströmung innerhalb eines thermischen Lichtbogentriebwerks

HLRN-Projektkennung:	hbi00024
Laufzeit:	II/2014 – II/2016
Projektleiter:	PD Dr.-Ing. habil. Rodion Groll
Projektbearbeiter.	Juan Gomez
Institut / Einrichtung:	ZARM - Center of Applied Space Technology andMicrogravity, Universität Bremen

Überblick

Im vorliegenden Forschungsprojekt wird das Verhalten eines Lichtbogentriebwerks, welches mit den Edelgasen Neon, Argon, Krypton und Xenon betrieben wird, sowohl experimentell als auch numerisch untersucht. In der laufenden Phase des Projektes wird der Fokus auf das Verhaltender kompressiblen Strömung im Kaltgas-Betrieb gelegt. Der experimentelle Versuchsaufbau wird in Abb. 1 schematisch dargestellt. Das Kaltgas-Triebwerk wird unter Vakuumbedingungen betrieben. Dabei wird der Druckverlust für die jeweiligen Gase bei verschiedenen Massenstromwerten zwischen 0,178 mg/s und 3,568 mg/s gemessen. Die Knudsen-Zahlen der untersuchten Betriebspunkte liegen oberhalb der Kontinuumsgrenze 0,01, was zum Auftreten von Verdünnungseffekten führt. Bei höheren Massenstromwerten befinden sich die Strömungen im Slip-Flow-Bereich, während bei den niedrigen Massenstromwerten der Transitionsbereich erreicht wird. Die experimentell ermittelten Druckwerte werden mit numerischen Simulationsergebnissen verglichen. Als numerischer Ansatz werden sowohl die kompressible Form der Navier-Stokes-Gleichungen mit gewöhnlichen Haftbedingungen, als auch die kinetische Direct-Simulation-Monte-Carlo (DSMC) Methode berücksichtigt. Mit steigenden Werten der Knudsen-Zahl (Kn) können starke Abweichungen für die Navier-Stokes-Ergebnisse im Vergleich zu den experimentellen und den DSMC-Ergebnissen festgestellt werden. Diese Beobachtung lässt sich durch die Diskrepanz zwischen der angewendeten Haftbedingung und den auftretenden Verdünnungseffektenerklären, welche mit sinkenden Massenstromwerten dominant werden.

Aus dem Vergleich zwischen den experimentellen Ergebnissen und den Navier-Stokes-Simulationen wird eine von der Knudsen-Zahl abhängige Korrekturfunktion entwickelt, welche auf vier gasunabhängigen Koeffizienten basiert.Die Knudsenfunktion ermöglicht es, aus Navier-Stokes-Simulationen mit gewöhnlichen Haftbedingungen, die deutlich niedrigere Rechenanforderungen im Verglich mit DSMC-Simulationen haben, den korrekten Druckverlust in Abhängigkeit von der Knudsen-Zahl zu bestimmen. Der entwickelte Ansatz ist somit hilfreich für die Untersuchung von Versuchsaufbauten, welche in einem großen Massenstrombereich betrieben werden und bei denen unterschiedliche Strömungsbereiche auftreten können, vorausgesetzt, dass auf eine gründliche, numerische Unterscheidung zwischen dem Kontinuums-, dem Slip-Flow- und dem Transitionsbereich verzichtet werden kann. Die Ergebnisse tragen dazu bei, die Zusammenhänge innerhalb einer Mikrodüseim Slip-Flow- und Transitionsbereich zu verstehen und bilden die Grundlagen für die Auswertung eines mathematischen Modells für den Heißgas-Betrieb des Lichtbogentriebwerks.

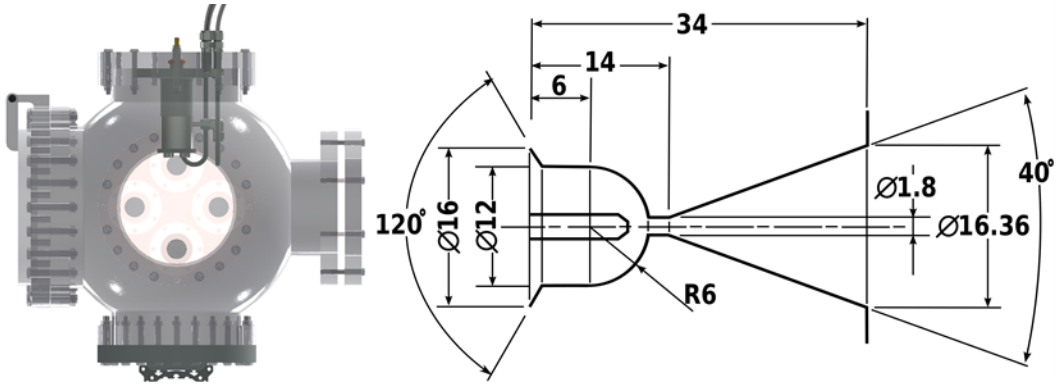

Abb. 1: Schematische Darstellung des Versuchsaufbaus (links) und der eingesetzten Lavaldüse (rechts) mit geometrischen Maßen in mm.

Ergebnisse

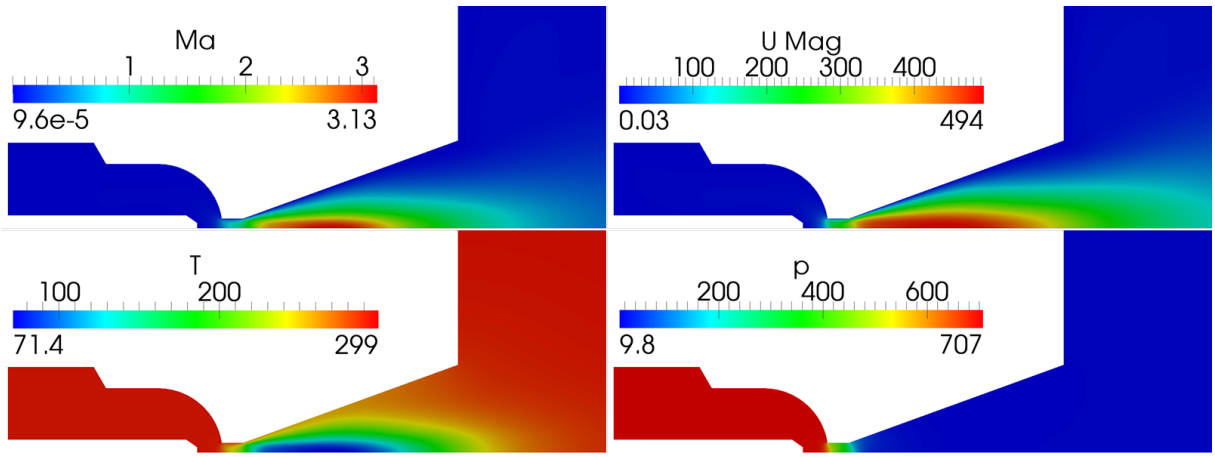

Abb. 2: Strömungsfelder für Argon, Massenstrom=3.568 mg/s, Re=240. Ma: Mach-Zahl; Umag: Geschwindigkeit [m/s]; T:Temperatur [K]; p: Druck [Pa].

Abb. 2 zeigt als Beispiel die Strömungsfelder für die Simulation mit Argon als Treibgas und einem Massenstrom von 3,558 mg/s. Das Gas wird vom Inlet (auf der linken Seite der Abbildung) durch die Lavaldüse und zum Outlet hin beschleunigt. Im Düsenhals wird die Schallgeschwindigkeit erreicht. Nach dem Wirkungsprinzip der Lavaldüse nehmen Mach-Zahl und Strömungsgeschwindigkeit im Diffusor der Lavaldüse zu. Die maximale Geschwindigkeit beträgt in dem dargestellten Fall ca. 494 m/s. Die anhand experimenteller Ergebnisse ermittelten Knudsen-Zahlen für die untersuchten Betriebspunkte liegen zwischen 0,02 und 0,33, d. h., in dem Slip-Flow- und Transitionsbereich. Darüber hinaus liegen die numerisch ermittelten Reynolds-Zahlen zwischen 8 und 256. Wie aus Abb. 2 ersichtlich ist, wird eine maximale Mach-Zahl von 3,13 im Diffusor der Lavaldüse, relativ weit entfernt vom Düsenausgang, erreicht. Anschließend nimmt die Mach-Zahl in Richtung Ausgang ab. Dabei kann ein Abstieg der Strömungsgeschwindigkeit und ein Anstieg der Strömungstemperatur beobachtet werden, was ohne das Auftreten eines Verdichtungsstoßes stattfindet.Dieses Ergebnis resultiert aus der Umwandlung von kinetischer Energie in thermische Energie innerhalb der Lavaldüse. Der Vorgang kann durch die niedrige Reynolds-Zahl des Systems (Re=240) und die damit verbundene, dicke viskose Grenzschicht erklärt werden. Diese steht wiederum im Zusammenhang mit dem bei Mikrodüsen typisch hohen Verhältnis von

Wandfläche zu Volumen. Man beachte, dass die Geschwindigkeitsabnahme im Diffusor eine Reduzierung der vom Triebwerk erzeugten Schubkraft zur Folge hat und somit einer suboptimalen Nutzung der im Treibgas enthaltenen Energie entspricht.

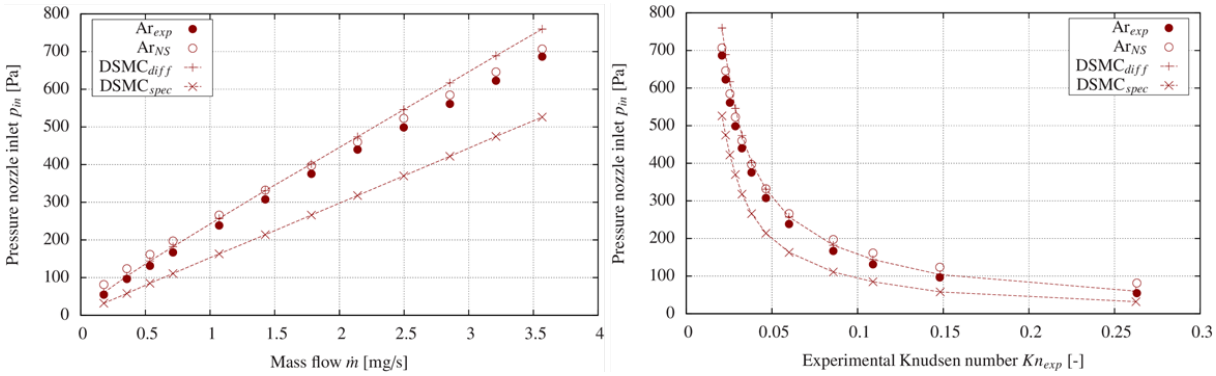

Abb. 3: Inletdruck vs. Massenstrom (links) und Knudsen-Zahl (rechts) für Argon.

Die Druckergebnisse am Inlet der Lavaldüse werden in Abb. 3 für Argon in Abhängigkeit von dem Massenstrom und der Knudsen-Zahl dargestellt. Dabei werden die experimentellen, die Navier-Stokes-, die DSMC-Ergebnisse mit direkter Reflektion als Modell für die Wechselwirkung zwischen Atomen und Wänden ($DSMC_{spec}$) und die DSMC-Ergebnisse mit dem diffusen Reflektionsmodell ($DSMC_{diff}$) gezeigt. Aus Abb. 3 ist ersichtlich, dass die DSMC-Ergebnisse mit direkter Reflektion deutlich unter den experimentellen Werten liegen. Grund hierfür ist die Unterschätzung der Impulsverluste an den Düsenwänden und somit der Druckverluste im System. Bei niedrigen Massenstromwerten und hohen Knudsen-Zahlen im Transitionsbereich (Kn>0,1) stimmen die DSMC-Ergebnisse mit dem diffusen Reflektionsmodell (Maxwell-Modell) gut mit den experimentellen Werten überein. Darüber hinaus liefert der Ansatz mit den Navier-Stokes-Gleichungen gute Ergebnisse für hohe Massenstromwerte und niedrige Knudsen-Zahlen (Kn<0,05), obwohl der Kontinuumsbereich noch nicht erreicht wird.

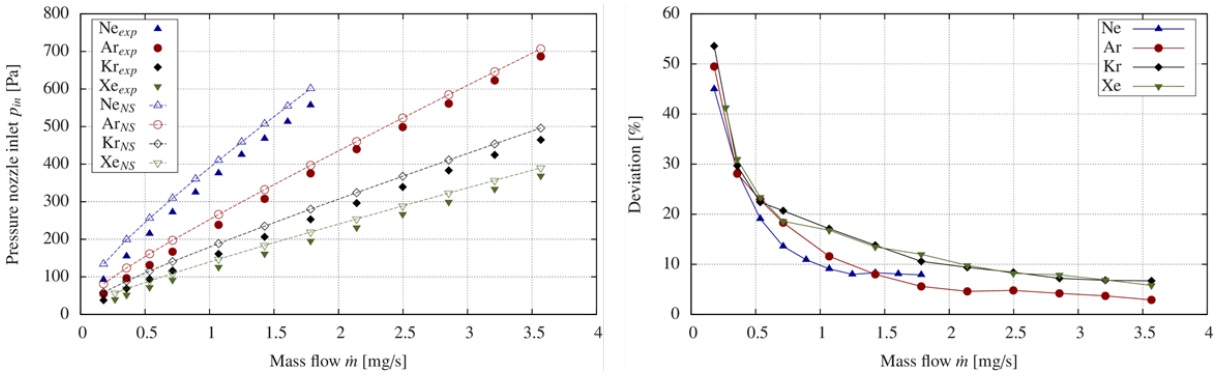

Abb. 4: Experimentelle und Navier-Stokes-Ergebnisse für den Inletdruck in Abhängigkeit vom Massenstrom.Links: Absolute Druckwerte; rechts: Relative Abweichungen.

Die experimentellen und Navier-Stokes-Ergebnisse für den absoluten Inletdruck werden in Abb. 4 für die untersuchten Gase dargestellt. Bei niedrigen Massenstromwerten und hohen Knudsen-Zahlen können starke Abweichungen zwischen den experimentellen und den Navier-Stokes-Ergebnissen festgestellt werden. Die relativen Abweichungen steigen mit

abnehmenden Massenstromwerten zu, was durch die Diskrepanz zwischen den für die Simulationen angewendeten Haftbedingungen und dem verdünnten Charakter der Strömungen erklärt werden kann.

Auf Basis des Vergleiches zwischen den experimentellen und den numerischen Druckergebnissen wird eine von der Knudsen-Zahl abhängige Korrekturfunktion entwickelt, welche auf vier gasunabhängigen Koeffizienten basiert. Die Knudsen-Funktion beschreibt die Abweichung zwischen den experimentellen und den numerischen Ergebnissen in Abhängigkeit von der numerisch ermittelten Knudsen-Zahl. Darüber hinaus kann eine Korrelation zwischen den ermittelten Knudsen-Koeffizienten und der Molmasse der eingesetzten Gase festgestellt werden. Demzufolge lässt sich die Knudsen-Funktion als eine von der Molmasse abhängige Funktion aufstellen.

Die entwickelte Funktion kann anschließend dazu genutzt werden, die Ergebnisse der Navier-Stokes-Simulationen mit Haftbedingungen zu korrigieren. Wie aus Abb. 5 ersichtlich ist, können durch diesen Ansatz die relativen Abweichungen der Druckergebnisse von über 50 % auf unter 5 % reduziert werden. Dabei ist der Ansatz sowohl vom untersuchten Gas als auch vom Strömungsbereich (Kontinuums- Slip-Flow- oder Transitionsbereich) unabhängig. Da die Knudsen-Koeffizienten aus dimensionslosen Zahlen ermittelt werden, wird die qualitative Gültigkeit des entwickelten Ansatzes für vergleichbare Lavaldüsengeometrien erwartet.

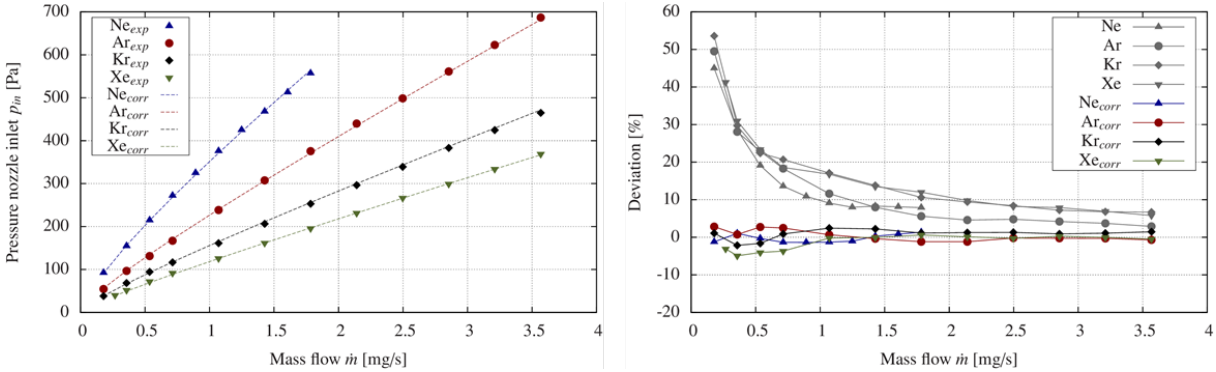

Abb. 5: Experimentelle und korrigierte Navier-Stokes-Ergebnisse für den Inletdruck in Abhängigkeit vom Massenstrom.Links: Absolute Druckwerte; rechts: Relative Abweichungen.

Ausblick

Mit Hinblick auf das Verhalten des Kaltgas-Triebwerks ist der Einfluss von geometrischen Parametern, wie dem Öffnungswinkel des Diffusors und dem Düsenhalsdurchmesser, Bestandteil zukünftiger Untersuchungen. Darüber hinaus ist die Übertragbarkeit der ermittelten Knudsen-Koeffizienten aufzweiatomige Gase, Hydrazin oder Ammoniak von Interesse. Des Weiteren bilden die Kaltgas-Ergebnisse die Grundlagen für die Auswertung eines mathematischen Modells für den Heißgas-Betrieb des Lichtbogentriebwerks.

Publikationen

J. Gomez, R. Groll, *Pressure drop and thrust predictions for transonic micronozzle flows*, Physics of Fluids (1994-present), *28*, *022008* (*2016*)

6.5 *hbi00025:* Large Eddy simulation of bounded spray flow / Large-Eddy-Simulation zur Vorhersage von engberandeten Sprühstrahlen

HLRNProject ID:	hbi00025
Run time:	IV/2014 – III/2015
Project Leader:	Prof. Dr.-Ing. habil. Udo Fritsching
Project Scientists:	M.Sc. Aljoscha Lampa
Affiliation:	Particles and Process Engineering, University Bremen

Overview

For flow configurations with a strong counter stream component, like in bounded spray flow, the instability of the spray jet could be crucially affected. The result is a global instability of the spray jet resulting in strong flapping and precession. Groups of droplet clusters are slung into the recirculation zone. The result is an inhomogeneous spray flow and drying process. Large-Eddy-Simulation and RANS model are used to simulate the droplet and the gas flow structures in a bounded spray.

Results

It is possible to simulate two-phase flows with transient turbulence resolving simulation methods (e.g. Large-Eddy-Simulation). The high mesh resolution and the small time-step necessary in LES two-phase flow modeling with lagrangian tracking of particles make such simulations reasonably applicable to low Reynolds number flows. Thus, the influence of the spray chamber boundaries on the mean spray flow has been investigated also with time-averaged simulations (RANS). By changing the shape and the size of the spray tower, the effect on the entrainment has been analyzed. Here, a conical part and an orifice have been integrated into the spray chamber model. Variations of the spray tower width at different flow rates of the atomizer are also studied.

The flow inside the spray tower is characterized by a large recirculation zone which is also found in similar studies of concurrent tall-form spray dryer. Through the large recirculation zone the mixing inside the spray tower is enhanced. Air laden with moisture and small particles is recirculated upwards and is entrained into the spray. The result is a relatively homogeneous temperature and species distribution inside the spray tower at $z > 200$ mm.

The recirculation/entrainment rate can be evaluated from the simulations by integrating the velocity profile of the upwards directed gas flow. The resulting can be divided by the volumetric flow rate of air through the hot gas nozzle. There is a recirculation maximum in the center of the recirculation zone. From the reattachment point the flow profile is unidirectional. The position of the reattachment could be determined in experiments (Variant A) and agrees with the simulation results ($z_{reattachment} \approx 2.5$ m). The air close to the wall, which is recirculated, heats up the spray tower walls. The Variant A is without any modifications of the spray chamber design. Variant B is equipped with a conical part in the spray tower to make the recirculation zones close to the nozzle smaller to avoid accumulation of material in these areas. The case number C is investigated to show the change of entrainment flow close to the nozzle in dependence of the spray tower height. The Variant D is a mixture of variant B and C.

The variant A shows a flow pattern that is related to concurrent spray drying processes with pneumatic nozzle systems. The flow from the air dispenser is centered and pointing downwards to adapt the direction of the heat flow to the low expansion angle of the spray flow. In some applications the air stream has a swirl component to avoid the uncontrolled deflection of the spray onto the spray chamber walls. In the hot gas atomization process swirl is not necessary because of the strong axial momentum flux from the nozzle.

In variant B the recirculation zones close to the nozzle are minimized by limiting the cross-sectional area. This variant is already used in many spray dryers. The entrainment flow profile is not changed in comparison with variant A. A strong deflection of the gas flow (and thereby also of the particles) in the spray towards the wall is found for variant C showing that hot gas atomization demands tall spray towers. Here, the axial momentum flux of the spray flow is higher than for a conventional concurrent spray drying process. The entrainment flow in front of the orifice is increased because of the strong deflection of the gas, but close to the nozzle the entrainment flow is the same as for variant A and B. Variant D combines the effects of Variant B and C.

Outlook

Analysis of spray structures in two-phase flow will be extended to other applications and systems. The specific demands from LES simulations need to be adopted in order to study even unsteady spray structures in bounded spray flows. This will be an important topic for further investigations.

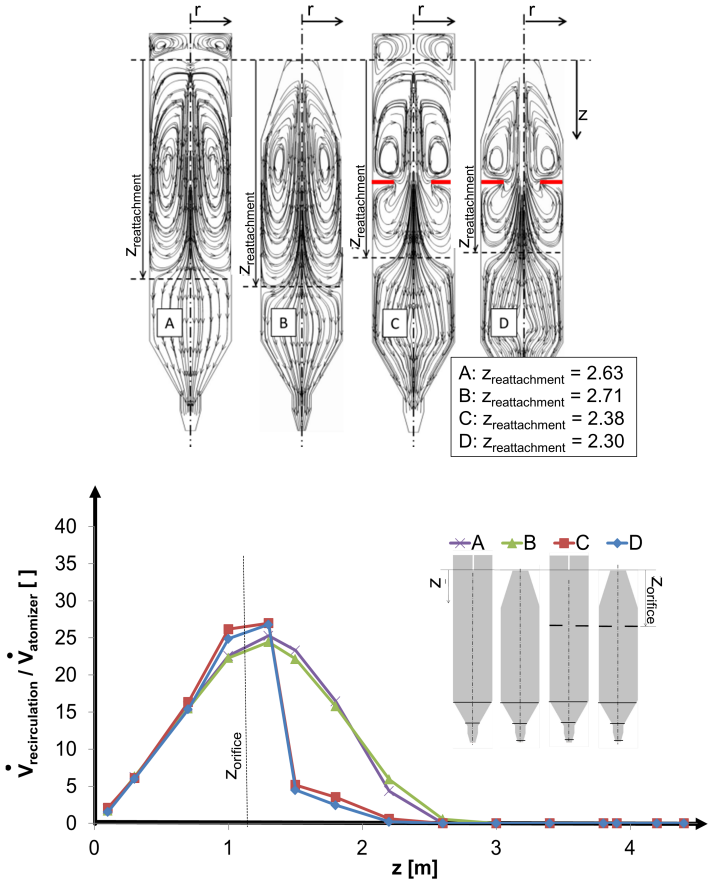

Fig. 1: Recirculation gas flow pattern for different tower geometries and entrainment volumetric gas flow dependent on the distance from the atomizer (atomizer = 200 m3/h, only gas phase)

Publications

1. Lampa, A.; Fritsching, U.: Impact of Droplet Clustering on Heat Transfer in Spray Processes; ASME 2014 4th Joint US-European Fluids Engineering Division Summer Meeting, FEDSM2014, paper FEDSM2014-21562, August 3-7, 2014, Chicago, Illinois, USA; doi:10.1115/FEDSM2014-21562

Presentations

1. Lampa, A., Fritsching, U.: Impact of Droplet Clustering on Heat Transfer in Spray Processes; Proc. ILASS 2014 – 26th European Conference on Liquid Atomization & Spray Systems, Bremen, Germany, 8-10 Sep. 2014
2. U. Fritsching, A. Lampa: Droplet Clustering in Spray Processes; ICLASS 2015, 13th Triennial International Conference on Liquid Atomization and Spray Systems, Tainan, Taiwan, August 23-27, 2015
3. Lampa, A.; Sander, S.; Schwenck, D.; Fritsching, U.:Recirculation, Entrainment and Cluster Formation in bounded Sprays; Proc. 9th International Conference on Multiphase Flow (ICMF 2016), May 22 to 27, 2016, Firenze, Italy

Acknowledgement

The project has been funded by the German Research Foundation (DFG) within the SPP 1423 “Process-Spray”.

6.6 *hbi00026:* DSMC-Simulation einer verdünnten Edelgasströmung innerhalb eines Kaltgas-Arcjets

HLRN-Projektkennung:	hbi00026
Laufzeit:	II/2015 – I/2016
Projektleiter:	Dr.-Ing. habil. Rodion Groll
Projektbearbeiter.	Till Frieler, M. Sc.
Institut / Einrichtung:	ZARM – Zentrum für angewandte Raumfahrttechnologie und Mikrogravitation, Universität Bremen

Motivation und Projektbeschreibung: MOLETHRUSTBALANCE

Elektrische Raumfahrtantriebe sind heutzutage bereits in einer Vielzahl von Weltraummissionen erfolgreich im Einsatz und werden beispielsweise zur Bahn- und Lageregelung auf geostationären Kommunikationssatelliten oder für interplanetare Langzeitmission genutzt. Für die Entwicklung neuer Triebwerke sind unter anderem Leistungsmerkmale, wie Antriebsleistung (spezifischer Impuls), Treibstoffverbrauch (Treibstoffeffizienz) und Regelverhalten (Schubcharakteristik) von großer Bedeutung.

In thermischen Lichtbogentriebwerken, welche innerhalb der elektrischen Antriebe eine eigene Klasse von Triebwerken darstellen, wird das Antriebsgas aus einem Überdruckreservoir über die Lavaldüsen-Geometrie des Triebwerks beschleunigt und somit Schub in Form von kinetischer Energie der Gasteilchen erzeugt. Zusätzlich wird im Heißgasbetrieb dem strömenden Gas zusätzlich thermische Energie über einen Lichtbogen zugeführt, um die Austrittsgeschwindigkeit und den spezifischen Impuls zu erhöhen. Bei gleichbleibendem Massenstrom kommt es so zu einer Steigerung der Antriebsleistung und zu einer Verbesserung der Treibstoffeffizienz.

Um eine Aussage über die Treibstoffeffizienz und die Schubcharakteristik eines Triebwerks machen zu können, ist es sinnvoll die Schubkraft F_s bestimmen zu können. Im Rahmen des Forschungsprojektes MOLETHRUSTBALANCE wird einerseits ein Versuchsstand zur experimentellen Messung und Untersuchung der Schubkraft von elektrischen Triebwerken niedriger Leistungsklasse entwickelt und aufgebaut, sowie andererseits numerische Kaltgas-Simulationen mittels DSMC-Methoden durchgeführt. Die Ergebnisse aus den Simulationen und den durchgeführten Versuchen sollen anschließend verglichen werden, um so Erkenntnisse für die weitere Optimierung des Triebwerks sammeln zu können.

Das in dem Projekt MOLETHRUSTBALANCE untersuchte Triebwerk ist das am ZARM neu entworfene Lichtbogentriebwerk INGA IV. Ein Querschnitt des Triebwerks mit Bezeichnungen für alle wichtigen Komponenten ist in Abbildung 1 dargestellt. Mit dem vorgestellten Triebwerk INGA IV können Differenzdrücke zwischen dem Inneren des Triebwerks und der Vakuumkammer aufgezeichnet und Untersucht werden. Aus den gemessenen Drücken und dem Massenstrom des eingeleiteten Gases können, unter Verwendung der numerischen Methoden, Rückschlüsse auf die Antriebsleistung gezogen werden. Zusätzlich wird in dem Projekt eine Schubwaage zur experimentellen Untersuchung der Antriebsleistung entwickelt, ausgelegt und aufgebaut. Auf Details der Schubwaage soll an dieser Stelle nicht näher eingegangen werden.

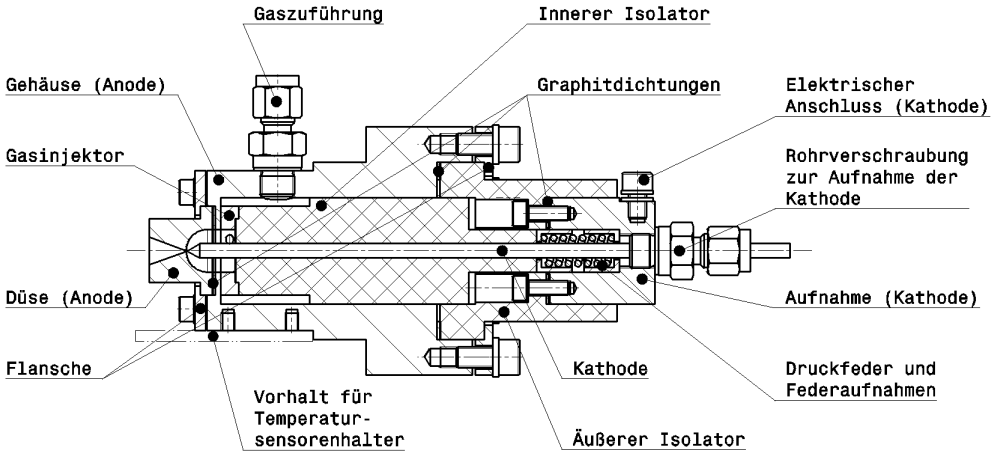

Abb. 1: Querschnittsdarstellung des INGA IV Lichtbogentriebwerk.

Technische und mathematische Aspekte

Für die, in dem Projekt MOLETHRUSTBALANCE durchgeführten, numerischen Berechnungen wurden an der Standardimplementierung des DSMC-Solvers in dem Softwarepaket OpenFOAM einige Änderungen vorgenommen. Die Änderungen beinhalteten die Implementierung eines neuen Inflowmodells *ZARMInOutflow,* welches auf dem *InOutflow*-Modell der Standardimplementierung aufbaut. Es ermöglicht dem Nutzer die, aus den Experimenten genau definierten, Massen- oder Volumenströme über die Volumenränder des Inlets vorzugeben. Für die Randflächen des Outletvolumens ist der Druck die vorgegebene makroskopische Größe aus den Experiemten. Dieser wird als Absolutdruck durch die Drucksensoren der Vakuumanlage gemessen und stellt den, sich im stationären Betriebszustand eingestellten, Umgebungsdruck in einiger Entfernung zum Diffusorende (Düsenauslass) dar.

Anders als bei Finite-Volumen-Solvern hängt bei statistischen Methoden, wie der DSMC-Methode, der Rechenaufwand stark von der Gesamtanzahl der simulierten Testpartikel im Simulationsvolumen ab. Der Rechenaufwand für die einzelnen Testpartikel lässt sich hierbei nochmals in die Anteile Molekülbewegung und Kollisionsberechnung unterteilen. Abhängig von der Art der Implementierung der Kollisionsroutine in den numerischen Solver nimmt nach Titov [1] die Berechnung der Kollisionen bis zu 60% der Rechenzeit in Anspruch. Um den numerischen Aufwand der Kollisionsberechnung bei hohen Drücken zu reduzieren, wurde die Anzahl der möglichen Kollisionen pro Zelle und Zeitschritt begrenzt. Hierbei wurde ein Wert von zwei Kollisionen pro Testpartikel nach Titiov [1] gewählt.

Ergebnisse: Vergleich mit Finiter Volumen Methode

Um die molekulare Charakteristik der simulierten Strömung zu verdeutlichen und um eine erste Validierung der Ergebnisse durchzuführen, wurden die numerischen Ergebnisse der DSMC-Methode mit einer kontinuierlichen Finite-Volumen-Methode (FVM) verglichen. Als Solver für die kontinuierliche Simulation wurde FVM-Solver *rhoCentralFoam* verwendet, welcher ebenfalls im Softwarepaket OpenFOAM zur Verfügung steht. Aus Stabilitätsgründen wurde das Outletvolumen in seinen Abmessungen vergrößert, die übrigen Maße blieben identisch. Das Gitter wurde feiner vernetzt, wobei jedoch auf eine Verfeinerung der

Gitterstruktur in den Bereichen Brennkammer- und Outletvolumen verzichtet wurde, so dass die absolute Zellenzahl ungefähr konstant blieb.

Als Betriebsgas für den Vergleichsfall wurde das Edelgas Argon ausgewählt, welches mit $3{,}6 \cdot 10^{-7}$kg/s die Massenstromrandbedingung am Inlet darstellt. Am Outletrand wurde als Randbedingung ein Druck von 1Pa festgelegt, sowie die Temperatur der Gasströmung durch das Volumen auf eine Raumtemperatur von 300K.

Die Verläufe des Drucks *p*, der Temperatur *T* und der Geschwindigkeit *U* über die Düsengeometrie sind für die beiden Methoden in Abbildung 2 dargestellt. Um einen besseren Vergleich der molekülbasierenden DSMC-Methode mit der finite Volumen Methode zu ermöglichen, sind in der Abbildung noch zwei blaue Linien eingezeichnet, welche aus dem Knudsen-Zahl-Feld der DSMC-Rechnung ermittelt wurden. Die linke Linie stellt mit einer Knudsen-Zahl von 0,02 den Übergangsbereich von der Kontinuumsströmung zur Gleitströmung dar, während die rechte Linie bei einer Knudsen-Zahl von 0,1 den Übergangsbereich zur nahezu freien Molekülströmung darstellt. Gut zu erkennen ist, dass im Anfangsbereich der Brennkammer die Größen Druck, Temperatur und Geschwindigkeit der DSMC- und der FVM-Methode nahezu identisch sind. Mit Erreichen des Übergangsbereichs bei einer Knudsen-Zahl von 0,02 beginnen sich die Verläufe der Kurven für *p*, *T* und *U* zu unterscheiden.

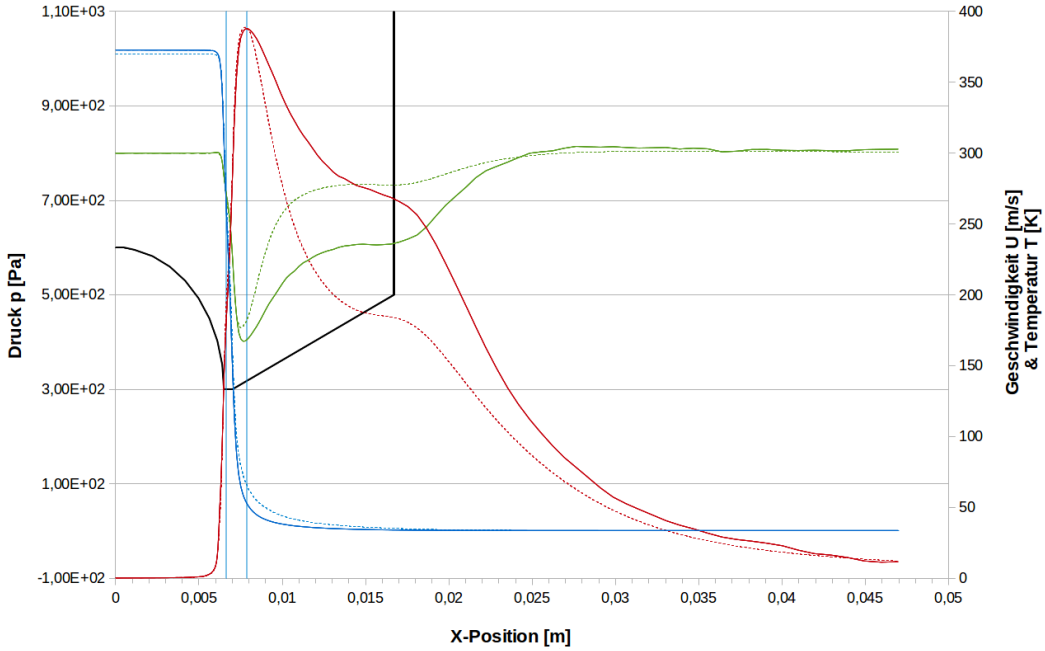

Abb. 2: Verläufe für Druck *p* (blaue Kurven), Temperatur *T* (grüne Kurven) und Geschwindigkeit *U* (rote Kurven) über die Düsengeometrie für die DSMC-Methode (kontinuierliche Linien) und die FVM-Methode (gestrichelte Linien).

Kurz vor Erreichen des Düsenhalses beginnen die mit den beiden Methoden ermittelten Strömungsgeschwindigkeiten stark anzusteigen, wobei sich ihre Verläufe bei einer Knudsen-Zahl von 0,02 noch nahezu decken. Dieser Anstieg erfolgt bis kurz hinter dem Ende des Düsenhalses, wo bei einer Knudsen-Zahl von 0,1 und somit am Übergangsbereich zur nahezu freien Molekülströmung die maximalen Geschwindigkeiten erreicht werden. Nach dieser Stelle kommt es zu über den Verlauf des Diffusors zu einem Abfall beider Geschwindigkeitskurven, jedoch mit stark unterschiedlichem Verlauf. So liegt über die gesamte Diffusorlänge die, mit der DSMC-Methode ermittelte, Geschwindigkeit oberhalb der

Geschwindigkeit der FV-Methode. Diese Differenz wird in Richtung des Diffusorendes und mit steigenden Knudsen-Zahlen größer und erreicht ihr Maximum kurz vor dem Düsenauslass. Hier liegt die mit der DSMC-Methode ermittelte Geschwindigkeit über 70m/s oder 28% über der Geschwindigkeit der FV-Methode. Nach dem Austritt der Strömung aus der Düse gleichen sich die beiden Geschwindigkeitskurven bis zum Ende des Outlets wieder aneinander an. Die unterschiedlichen Geschwindigkeiten der beiden Methoden werden deutlich, wenn man die Geschwindigkeitsfelder des Diffusors miteinander vergleicht. Die Geschwindigkeitsfelder sind in Abbildung 3 a) dargestellt. Gut zu erkennen ist, dass bei der DSMC-Methode die Geschwindigkeit an der Wand des Diffusors nicht null ist und gleichzeitig die Geschwindigkeiten zur Mittelachse hin größer sind als bei der FV-Methode. Dieser Umstand ist auf den molekularen Charakter der Strömung bei den erreichten hohen Knudsen-Zahlen zurückzuführen, welche durch die DSMC-Methode besser abgebildet werden. Er kommt besonders an der Diffusorwand zum Tragen, da hier geringere Reibungsverluste auftreten, als bei einer Kontinuumsbetrachtung der Strömung vorhergesagt wird.

Die für die beiden Methoden dargestellten Temperaturverläufe sind im Kontinuumsbereich ebenfalls nahezu deckungsgleich. Kurz vor Erreichen des Übergangs zur nahezu freien Molekülströmung sinkt die Temperatur der DSMC-Methode jedoch stärker ab, als bei der FV-Methode. Die Differenz der Temperaturen steigt im Diffusor weiter an, so dass amDiffusorende die Temperatur der FV-Methode um ca. 42K bzw. 15% über den Werten der DSMC-Methode liegt. Am Outletrand gleichen sich die Temperaturverläufe wieder an. Der Unterschied der Temperaturverläufe ist nochmals in Abbildung 3 b) verdeutlicht. Er lässt sich aus der Zerlegung der Molekülgeschwindigkeit in Strömungs- und Eigengeschwindigkeit herleiten. Da die Strömungsgeschwindigkeit der DSMC-Methode höhere Werte erreicht, muss gleichzeitig die Eigengeschwindigkeit und somit Temperatur sinken.

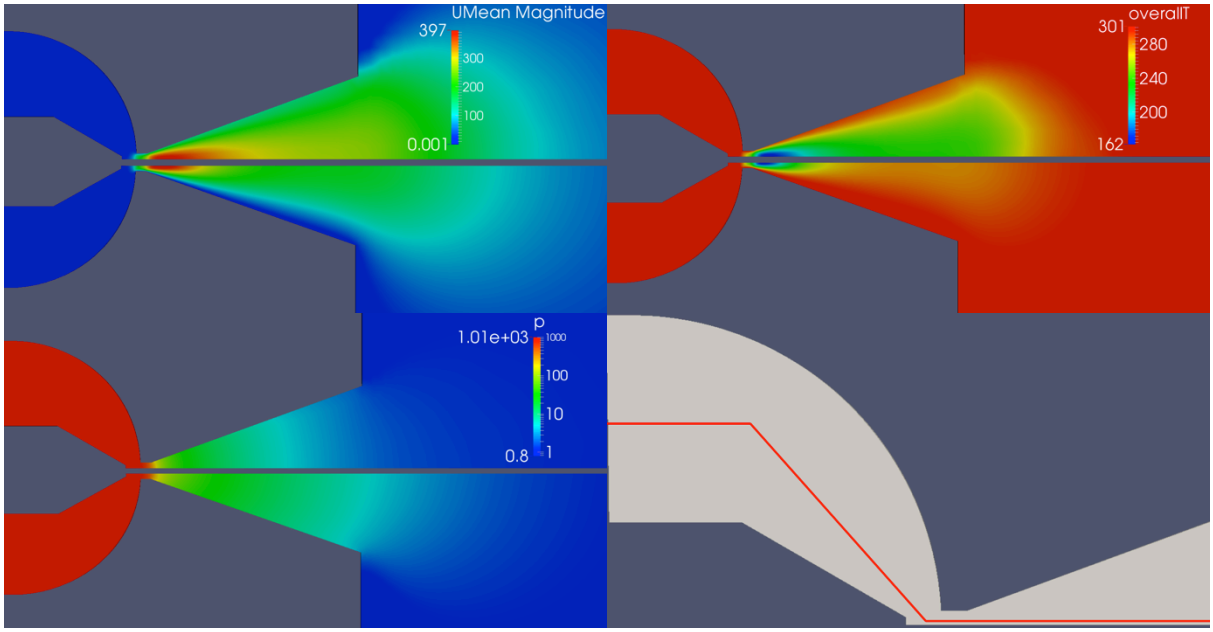

Abb. 3: Oben links: a) Geschwindigkeitsfelder der Rechnung, Ergebnisse des DSMC-Solvers über denen der FV-Methode. Oben rechts: b) Temperaturfelder der Rechnung, Ergebnisse des DSMC-Solvers über denen der FV-Methode. Unten links: c) Druckfelder der Rechnung, Ergebnisse des DMSC-Solvers über denen der FV-Methode. Unten rechts: Verdeutlichung der für die Darstellung der Werte in Abbildung 2 benutzten Linie durch das Simulationsvolumen.

Zuletzt ist noch die Betrachtung der Druckverläufe von Interesse. Hier liegen die Werte im Kontinuumsbereich ebenfalls nahezu deckungsgleich. Ab dem Düsenhalsanfang kommt es bei beiden Methoden zu einem starken Druckabfall, welcher bei der DSMC-Methode stärker ausgeprägt ist und bezogen auf die x-Richtung der Geometrie schon früher niedrigere Drücke erreicht werden, als bei der FV-Methode. Im Bereich des Übergangs zur nahezu freien Molekülströmung bzw. am Beginn des Diffusors ist die Differenz der Druckverläufe mit bis zu 35Pa für die beiden Methoden am größten. Nach dem Übergang der Strömung in den Diffusor gleichen sich die beiden Druckurven bis zum Outlet wieder an. Zur besseren Verdeutlichung der unterschiedlichen Druckverläufe ist Abbildung 3 c) logarithmisch skaliert.

Ausblick

In dem Forschungsprojekt MOLETHRUSTBALANCE sollen aus numerischen Bestimmung des Schubs, sowie experimentellen Schubmessungen Erkenntnisse für die Optimierung des INGA IV Triebwerks gesammelt werden. Hierfür sollen sowohl im experimentellen Aufbau, sowie bei den numerischen Berechnungen eine Reihe von Parametern innerhalb einer Parameterstudie variiert und deren Einfluss ausgewertet werden. Im letzten Antragszeitraum wurden bereits einige Parameter anhand einer Argon-Gas Strömung untersucht. In der zukünftigen Parameterstudie sollen nun diese Berechnungen auch für die anderen, im experimentellen Aufbau INGA IV zur Verfügung stehenden, Edelgase erweitert werden. Hierfür wurden als weitere zu untersuchende Gase Neon, Krypton und Xenon ausgewählt. Sie eignen sich aufgrund ihrer unterschiedlichen physikalischen Eigenschaften (wie zb. Molekülmasse) gut, um exemplarisch Strömungseigenschaften unterschiedlicher Gase zu untersuchen und ihren Einfluss auf die Effizienz des Lichtbogentriebwerks zu bestimmen.

Publikationen

T.Frieler, R. Groll: Using DSMC collision limiter for micronozzle thrust predictions with high density ratios. (in Vorbereitung)

WWW

https://www.zarm.uni-bremen.de/

WeitereInformationen/ Literatur

[1] Titov, Evgeny V., and Deborah A. Levin. "Extension of the DSMC method to high pressure flows." International Journal of Computational Fluid Dynamics 21.9-10 (2007): 351-368.

6.7 *hbk00018:* Berechnung der Wasserdampfkonzentrationen aus Limb-Messungen des Satelliteninstruments SCIAMACHY

HLRN-Projektkennung:	hbk00018
Laufzeit:	I/2012 – IV/2016
Projektleiter:	Dr. K. Weigel
Projektbearbeiter.	Dr. A. Rozanov, Dr. M. Vountas
Institut / Einrichtung:	Institut für Umweltphysik (IUP), Universität Bremen

Überblick

Im Rahmen der DFG-Forschergruppe SHARP (engl.: Stratospheric Change and its Role for Climate Prediction) und des ESA-Projekte SPIN (engl: ESA SPARC Initiative) und SQWG (engl: SCIAMACHY Quality Working Group) arbeiten wir an einer neuen Version für einen Wasserdampfdatensatz der oberen Troposphäre und unteren Stratosphäre. Grundlage der Berechnung sind SCIAMACHY (engl.: Scanning Imaging Absorption spectroMeter for Atmospheric CHartographY) Messungen. SCIAMACHY, ein Instrument auf dem europäischen Satelliten Envisat, lieferte von August 2002 bis April 2012 Messungen. Die veröffentliche Datenversion V3.01 wurde teilweise auf dem HLRN berechnet, beinhaltet aber nur einen Teil der auswertbaren Daten. Diese Zeitserie wird auch durch die Initiativen SPARC-DI (engl.: Stratospheric Processes and their Role in Climate - Data Initiative) und SPARC - WAVAS (engl.: Water Vapour Assessment) genutzt. Zurzeit arbeiten wir an einer Verbesserung der Rechenmethode insbesondere hinsichtlich der vertikalen Auflösung und der Aerosolkorrektur. Im Jahr 2015 wurde SCIATRAN so erweitert, dass zusätzlich zu OpenMP auch MPI genutzt werden kann. Dadurch können wesentlich größere Datenmengen parallel berechnet werden und es könnte nun erstmalig möglich sein, den kompletten Datensatz auszuwerten.

Ergebnisse

Wasserdampf in der Atmosphäre ist im Gegensatz zu Wassertröpfchen, die man als Wolken oder Nebel sehen kann, für das menschliche Auge unsichtbar. Trotzdem spielt er eine wichtige Rolle für den Strahlungstransport in der Atmosphäre, denn er absorbiert besonders gut Strahlung im infraroten Bereich und somit z.B. die von der Erde emittierte Wärmestrahlung. Für das kurzwelligere, sichtbare Licht ist er dagegen fast vollständig transparent. Dadurch ist er das wichtigste natürliche Treibhausgas. Der Wasserdampfgehalt der Atmosphäre schwank stark, sowohl örtlich als auch zeitlich. Den höchsten Wasserdampfgehalt findet man üblicherweise nahe dem Erdboden. An der Tropopause, d.h. am Übergang zwischen Troposphäre und Stratosphäre gibt es meist besonders wenig Wasserdampf. Die Troposphäre reicht bis in eine Höhe von etwa 10 bis 18 km und ist die Schicht, in der sich die meisten Wetterphänomene abspielen. Wolken findet man beispielsweise meist in der Troposphäre und nur unter bestimmten Bedingungen in der Stratosphäre. Das Wasserdampfminimum an der Tropopause hat aber einen großen Einfluss auf den Strahlungstransport, Modellstudien haben gezeigt, dass Änderungen des Wasserdampfgehaltes dort auch das Klima am Boden beeinflussen können. Ziel des DFG Projektes SHARP (siehe auch: www.fu-berlin.de/sharp/) ist es, zu einem besseren

Verständnis über die Verteilung und die zeitliche Änderung des Wasserdampfgehaltes in der Atmosphäre und dessen Wirkung auf das Klima beizutragen.

Um diese Wasserdampfminimum beobachten zu können braucht man sehr empfindliche Instrumente. Bodengebundene Messverfahren erreichen diesen Höhenbereich oft nur schlecht, Messungen von Ballonen und Flugzeugen sind nicht global und regelmäßig in ausreichender Qualität verfügbar. Limb-Messverfahren von Satelliteninstrumenten sind besonders gut geeignet um den Bereich der Tropopause zu beobachten. Bei diesem Messverfahren schaut das Instrument durch die Atmosphäre über den Erdboden hinweg in Richtung des Weltraumes und kann so verschiedene Höhen abtasten. Solche Messungen wurden, neben anderen Messverfahren, von SCIAMACHY (engl.: Scanning Imaging Absorption spectroMeter for Atmospheric CHartographY) durchgeführt, einem Spektrometer an Bord des europäischen Satelliten Envisat. Beim Limb-Messverfahren tastet SCIAMACHY die Atmosphäre mit Höhenschritten von jeweils 3.3 km ab. Bei jedem Höhenschritt wird das Spektrum des in der Atmosphäre gestreuten Sonnenlichts über einen breiten Wellenlängenbereich aufgezeichnet. Absorbtionslinien des Wasserdampfes im infraroten Bereich des Spektrums ermöglichen es den Wasserdampfgehalt der Atmosphäre zu bestimmen. Das gemessene Spektrum wird außer vom Wasserdampfgehalt auch durch Druck, Temperatur und die Streuung in der Atmosphäre z.B. an Aerosolen und Wolken beeinflusst.

Um Wasserdampfprofile aus den gemessen Spektren zu bestimmen verwenden wir SCIATRAN (Rozanov et al., 2011). Dabei wird mit einem Strahlungstransportmodell aus einer gegebenen Atmosphäre ein solches Spektrum berechnet, wobei auch die Mehrfachstreuung modelliert wird. Um aus den Messungen und den modellierten Spektren auf Wasserdampfprofile in der Atmosphäre zu schließen sind aufwändige, inverse mathematische Verfahren nötig. Das Ergebnis sind Wasserdampfprofile zwischen ca. 10 und 25 km Höhe. Die Berechnungen erfolgen iterativ und der Zeitaufwand ist groß, unter anderem weil ein breiter Spektralbereich und ein dichtes Höhengitter verwendet werden müssen. Dazu kommt die große Zahl von Profilen, die berechnet werden kann. SCIAMACHY Messungen gibt es von August 2002 bis zum plötzlichen Kontaktverlust mit Envisat im April 2012. In diesem Zeitraum gibt es etwa 4,5 Millionen Limb-Messungen bei Tageslicht, die sich prinzipiell für die Berechnung des Wasserdampfgehaltes eignen. Das sind über 1000 Profile pro Messtag. Mit einem Wolkenfilter werden zunächst die Profile identifiziert, bei denen hohe Wolken eine Auswertung erschweren. Nach der Filterung bleiben etwa 700 Profile pro Messtag übrig, die Zahl der Profile reduziert sich besonders in der Nähe des Äquators. Deshalb wurde für die letzte Datenversion V3.01 nur jeder 8. Tag global und jeder 2.Tag zwischen 45°N und 45°S ausgewertet.

Die Datenversion V3.01 haben wir mit verschiedenen Datensätzen von anderen Satelliteninstrumenten und Ballonmessungen verglichen und die Berechnung anhand von simulierten Messungen überprüft, siehe Weigel et al. (2016). Die Wasserdampfdaten werden im Rahmen internationaler Initiativen wie SPARC-DI (engl.: Stratospheric Processes and their Role in Climate - Data Initiative) und SPARC - WAVAS (engl.: Water Vapour Assessment) zur Erforschung der Stratosphäre genutzt und mit anderen Daten verglichen, siehe Hegglin et al. (2013) und Hegglin et al. (2014). Der Datensatz wird auch bei einer Studie zu Polaren Stratosphärenwolken verwendet (Khosrawi et al., 2016).

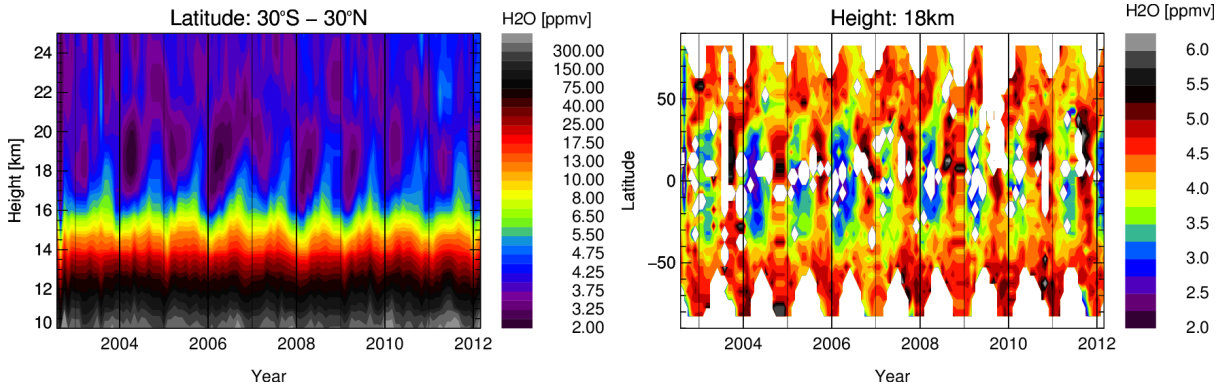

Abb. 1: Zeitserien des zonal gemittelten Wasserdampfes aus den SCIAMACHY Limb-Messungenaus der Testdatenversion V4.0, gemittelt für 30°N-30°S (links) und auf 18 km Höhe (rechts).

Mit der neuen SCIATRAN Version 3.5 ist es nun möglich, zusätzlich zur bisher verwendeten OpenMP Parallelisierung auch eine Parallelisierung mit Hilfe von MPI (engl.: message passing interface) zu verwenden. Dadurch konnten die Berechnung auf dem HLRN deutlich besser organisiert werden und es könnte nun erstmals möglich sein, den kompletten Datensatz auszuwerten. Gleichzeitig wurden Verbesserungen an der eigentlichen Rechenmethode implementiert, besonders hinsichtlich der Aerosolkorrektur und der Höhenauflösung. Abb. 1 zeigt Zeitserien des zonal gemittelten Wasserdampfes für einen ersten Testdatensatz, bei dem jeder 32. Tag ausgewertet wurde.

Ausblick

Eine erste Analyse des Testdatensatzes hat ergeben, dass weiter Verbesserungen der insbesondere der Aerosolkorrektur nötig sind. Dazu werden momentan Tests durchgeführt. Das Ziel ist, im Laufe des Jahres 2016 möglichst den gesamten Datensatzes auszuwerten.

Publikationen

- Rozanov, A., Weigel, K., Bovensmann, H., Dhomse, S., Eichmann, K.-U., Kivi, R., Rozanov, V., Vömel, H., Weber, M., and Burrows, J. P., *Retrieval of water vapor vertical distributions in the upper troposphere and the lower stratosphere from SCIAMACHY limb measurements*, Atmos. Meas. Techn., 4, 933-954, doi:10.5194/amt-4-933-2011, 2011.
- Hegglin, M. I., Tegtmeier, S., Anderson, J., Froidevaux, L., Fuller, R., Funke, B., Jones, A., Lingenfelser, G., Lumpe, J., Pendlebury, D. , Remsberg, E., Rozanov, A., Toohey, M., Urban, J., von Clarmann, T., Walker, K. A., Wang, R., Weigel, K.: *SPARC Data Initiative: Comparison of water vapourclimatologies from international satellite limb sounders*, J.Geophys. Res.,118, 20, 11824–11846, doi: 10.1002/jgrd.50752, 2013.
- Hegglin, M. I., Plummer, D. A., Shepherd, T. G., Scinocca, J. F., Anderson, J., Froidevaux, L. Funke, B., Hurst, D., Rozanov, A., Urban, J., von Clarmann, T., Walker, K. A., Wang, H. J., Tegtmeier, S., and Weigel, K.: *Vertical structure of stratospheric water vapour trends derived from merged satellite data*, Nature Geosc., 7, 768–776, doi:10.1038/ngeo2236, 2014.
- Khosrawi, F., Urban, J., Lossow, S., Stiller, G., Weigel, K., Braesicke, P., Pitts, M. C., Rozanov, A., Burrows, J. P., and Murtagh, D.*: Sensitivity of polar stratospheric cloud formation to changes in water vapour and temperature*, Atmos. Chem. Phys., 16, 101-121, doi:10.5194/acp-16-101-2016, 2016.

- Weigel, K., Rozanov, A., Azam, F., Bramstedt, K., Damadeo, R., Eichmann, K.-U., Gebhardt, C., Hurst, D., Kraemer, M., Lossow, S., Read, W., Spelten, N., Stiller, G. P., Walker, K. A., Weber, M., Bovensmann, H., and Burrows, J. P.: *UTLS water vapour from SCIAMACHY limb measurementsV3.01 (2002–2012)*, Atmos. Meas. Tech., 9, 133-158, doi:10.5194/amt-9-133-2016, 2016.

Vorträge / Poster

1. Weigel, A. Rozanov, S. Kowalewski, F. Azam, K. Bramstedt, K.-U. Eichmann, C. Gebhardt, P. Joeckel, M. Weber, G.P. Stiller, H. Bovensmann, and J.P. Burrows: *SCIAMACHY Limb Wasserdampf, Übersicht für V3.01 und Vorbereitungen für eine neue Datenversion*, SHARP Annual Meeting, Bremen, 14.07.2015

6.8 *hbk00021:* Understanding the dynamics and change in the Arctic Ocean

HLRN Project ID:	hbk00040
Run time:	II/2009 – III/2015
Project Leader:	Prof. Dr. Thomas Jung
Project Scientists:	Qiang Wang, Sergey Danilov
Affiliation:	Alfred Wegener Institute for Polar and Marine Research

Introduction

Sea ice is an important component of the Earth System, which is often being discussed in terms of integrated quantities such as Arctic sea ice extent and volume. Sea ice deformation characteristics such as leads, on the other hand, have attracted relatively little attention thus far. Leads may play an important role, despite of the fact that they cover only a relatively small fraction of the total Arctic sea ice area. Air-sea interaction is significantly reduced by sea ice, leaving the fluxes mainly in the area of leads, where there is open water or thin ice. In fact, turbulent heat transfer between the ocean and atmosphere is known to depend on the property of leads with small changes in the lead fraction having the potential to induce sizable temperature changes in the atmospheric boundary layer (Lupkes et al., 2008). Information on sea ice deformation, including leads, are also important for Arctic shipping (Jung et al., 2016).

Despite of the importance of sea ice leads, relatively little is known on how well they can be represented by commonly used sea ice models. The goal of this work is to show that sea ice linear kinematic features can be simulated by the traditional sea ice models with a certain skill. The prerequisite is a sufficiently high horizontal resolution along with numerical convergence of sea ice solvers, which is frequently neglected. We simulate Arctic sea ice using the elastic-visco-plastic (EVP) approach in a global sea ice ocean model at a local resolution of 4.5 km and show that many characteristics of the simulated 'cracks' agree with the available observations already at this resolution. This allows us to discuss the variability and trend of the lead features from long model-generated time series.

Method

The simulations were performed with the Finite Element Sea-ice Ocean Model (FESOM, see Wang et al., 2014, Danilov et al., 2015), which is the first mature global sea ice-ocean model that is formulated on unstructured meshes. We used a global configuration with nominal horizontal resolution of about 1 degree for most of the global ocean; north of 45^{o}N the horizontal resolution was increased to 24 km; and starting from the Arctic gateways (Fram Strait, Barents Sea Opening, Bering Strait, and the Canadian Arctic Archipelago) the resolution was further refined to 4.5 km. An updated version of the EVP method was used in this study in which all the components of the stress tensor are relaxed to their viscous-plastic state at the same rate (see Danilov et al., 2015). And we used 800 subcycling time steps in the EVP solver to warrant noise-free ice velocity divergence and shear.

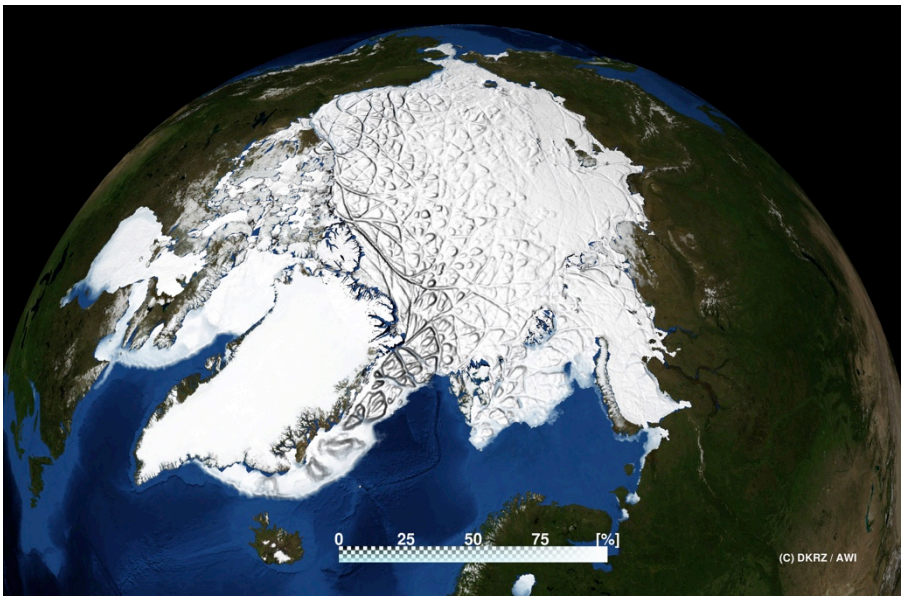

Figure 1: Simulated sea ice concentration on 1 January 2004 at horizontal resolutions of 4.5 km. Sea ice concentration is shown with color and thickness with shading (The figure is taken from Wang et al., 2016).

The model was forced using atmospheric state variables from the NCEP/NCAR Reanalysis. The spinup was done for the period 1948 to 1977 on another, coarser mesh without refinement to 4.5 km in the Arctic Ocean. At the end of the spin-up the data were interpolated to the fine mesh and the model was further run until 2014. The results of this study are based on the last 30 years (1985—2014) of the high-resolution simulation with Arctic refinement.

Results

A snapshot of the simulated sea ice concentration and thickness on 1 January 2004 is shown in Fig. 1. Evidently, the model captures many long and narrow cracks, which are typical features observed in sea ice (e.g., Wernecke and Kaleschke, 2015; Willmes and Heinemann, 2016). For this particular case, cracks are mainly located in Beaufort Sea and near Fram Strait. Very long cracks are also visible in the region of thick sea ice north of the Canadian Arctic Archipelago (CAA). The high resolution (4.5 km) used in the simulation is crucial for the model's capability to generate these small scale features.

Time series of monthly mean sea ice divergence and lead area fraction averaged over the Beaufort Sea are shown in Fig. 2a for the months when observations are available. Sea ice divergence shows pronounced variability, both on monthly and interannual time scales, which is very well reproduced by the model. The simulated lead area fraction variability also shows a relatively good agreement with the observed time series. Interestingly, neither the observations nor the model simulation shows any evidence for significant trends in lead area fraction during the winter season. Further analysis indicates that this is true also for other Arctic regional seas.

In February 2013, a pronounced fracturing event occurred in the Beaufort Sea. This event, which has attracted considerable attention (Wernecke and Kaleschke, 2015), was a result of strong storms leaving vast parts of the Beaufort Sea covered by leads. Hence, this event provides a good test case for assessing the fidelity of the high-resolution model. Evidently, the model is capable of reproducing the anomalous sea ice conditions, given that the highest lead area fraction is simulated in March 2013 relative to the same months of the other years (Fig. 2a, shown by blue squares).

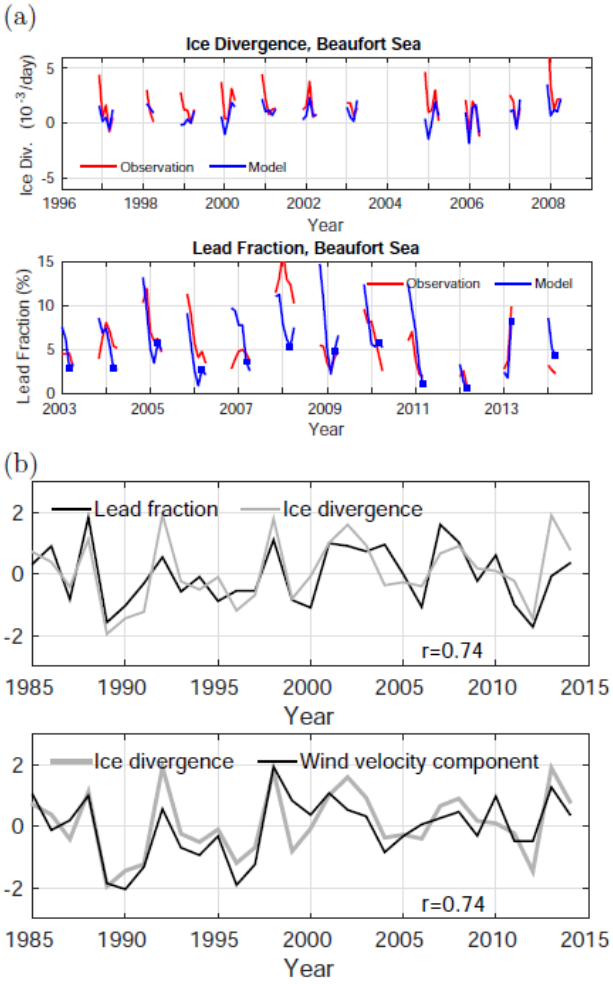

Figure 2: (a) Monthly time series of sea ice divergence and lead area fraction in Beaufort Sea. Only those months are shown for which observations are available. Simulated lead area fraction in March is shown by blue squares. (b) Simulated lead area fraction and sea ice divergence (upper panel) and sea ice divergence and the wind velocity component in the "favourable" direction (i.e. -74° relative to the meridional direction) (lower panel) in Beaufort Sea. The time series in (b) are based on wintertime (January through March) means and normalized by their respective standard deviations. (taken from Wang et al., 2016).

The fact that the model successfully simulates many of the observed features allows us to use the model results for an analysis of the sea ice lead variability. It turns out that on interannual time scalesthe simulated wintertime lead area fraction in Beaufort Sea is significantly correlated with the ice divergence (Fig. 2b). Furthermore, the correlation between ice divergence and wind velocity components at different direction has been calculated and the largest correlation coefficient is found for wind component in the direction about 74 degree to the northwest. At this direction the correlation coefficient amounts to 0.74. Finally, it is found that the correlation between ice divergence and sea level pressure (slp) is highest at the location of Beaufort High. Therefore, it can be concluded that a stronger (weaker) Beaufort High results in stronger (weaker) southeasterly winds in Beaufort Sea and thus higher (lower) ice divergence and lead area fraction.

Discussion and Conclusion

At 4.5 km resolution the EVP sea ice rheology can reproduce certain characteristics of observed sea ice deformation and lead area fraction, including their spatial distribution and temporal variability. However, the resolution used by us is not sufficient to model all aspects of real leads, many of which are typically much narrower (Tschudi et al., 2002). It is rather the resolution starting from which the models begin to demonstrate certain skill in representing the phenomenon – provided measures are taken to improve the convergence of their solutions. The results presented in this work are an important indication that there is hidden potential in traditional sea ice models.

Our simulation confirms that winter ice leads are mainly formed in marginal seas and near Fram Strait. The interannual variability of winter lead area fraction in Beaufort Sea can be largely explained by sea ice divergence changes, which are driven by southeasterly winds associated with variations in the strength of Beaufort High. The close relationship between wind speed, ice divergence and winter lead area fraction is also found in other Arctic regions, indicating that the wintertime lead area fraction variability can generally be explained by the variation of winds.

According to the simulations and observational data there is little evidence for the presence of significant trends in lead area fraction during wintertime. This is linked to the fact that Arctic wind stress has no significant trend so far. In summer, on the other hand, substantial positive trends in lead area fraction are found in the simulation (not shown). Summer sea ice concentration is low where the lead area fraction trends are found, so the potential climate impact of the trends is presumably less significant than winter trends would have. It remains to see whether lead area fraction in winter will increase in projected climate simulations.

Details of this work are described in Wang et al. (2016).

References

Danilov, S., Q.Wang, R. Timmermann, N. Iakovlev, D. Sidorenko, M. Kimmritz, T. Jung, and J. Schröeter (2015), Finite-Element Sea Ice Model (FESIM), version 2, Geoscientic Model Development, 8, 1747-1761.

Lüpkes, C., T. Vihma, G. Birnbaum, and U. Wacker (2008), Inuence of leads in sea ice on the temperature of the atmospheric boundary layer during polar night, Geophysical Research Letters, 35, L03,805.

Jung, T., and co-authors (2016), Advanced polar prediction capabilities on daily to seasonal time scales, Bulletin of the American Meteorological Society, accepted, doi:10.1175/BAMS-D-14-00246.1.

Tschudi, M. A., J. A. Curry, and J. A. Maslanik (2002), Characterization of springtime leads in the Beaufort/Chukchi Seas from airborne and satellite observations during FIRE/SHEBA, Journal of Geophysical Research-oceans, 107, 8034.

Wang, Q., S. Danilov, D. Sidorenko, R. Timmermann, C. Wekerle, X. Wang, T. Jung, and J. Schröter (2014), The Finite Element Sea Ice-Ocean Model (FESOM) v.1.4: formulation of an ocean general circulation model, Geosci. Model Dev., 7, 663-693.

Wang Q., S. Danilov, T. Jung, L. Kaleschke, and A. Werneck (2016), Sea ice leads in the Arctic Ocean: Modelling, interannual variability and trends, Geophys. Res. Lett., submitted.

Wernecke, A., and L. Kaleschke (2015), Lead detection in Arctic sea ice from CryoSat-2: quality assessment, lead area fraction and width distribution, The Cryosphere, 9, 1955-1968.

Willmes, S., and G. Heinemann (2016), Sea-IceWintertime Lead Frequencies and Regional Characteristics in the Arctic, 2003-2015, Remote Sens., 8, 4.

6.9 *hbk00032*: Evaluation of the multi-resolution global climate model ECHAM6-FESOM

HLRN Project ID:	hbk00032
Run time:	III/2015–II/2016
Project Leader:	Prof. Dr. Thomas Jung[1]
Project Scientists:	Dmitry Sidorenko[2], Dirk Barbi, Sergey Danilov, Helge Gößling, Sven Harig, Jan Hegewald, Thomas Rackow, Natalja Rakowsky, Dmitry Sein, Tido Semmler, Qiang Wang, Xuezhu Wang, Claudia Wekerle
Affiliation:	[1] also at University of Bremen [2] Alfred Wegener Institute for Polar and Marine Research

Summary

Most of climate models used at present for climate research use a spatial resolution of 1 degree in the atmosphere and ocean. Such models, as indicated by Climate Model Intercomparison Project (CMIP) 3 and 5 suffer from imperfect parameterizations of relevant processes, which is partly the consequence of their by far insufficient spatial resolution. The associated model biases are large and are often attributed in literature to the lack of oceanic resolution. Going beyond the coarse resolution of present-day climate models presents a challenge, because resolving all processes involving mesoscale dynamics over centennial time intervals would require enormous computational resources which are difficult to afford. This explains the interest in the climate modelling community in a new-generation of multi-resolution climate models, which allow one to increase the resolution locally where it is needed.

In this project, we use the AWI-CM climate model developed at the AWI, which is the first model of its kind available at present. It employs a mature sea ice-ocean component based on unstructured mesh technique – the Finite Element Sea Ice-Ocean Model (FESOM, Timmermann et al., 2009, Wang et al., 2014). The scientific aims we pursue are (I) to investigate how much the locally increased oceanic resolution can help to alleviate the climate model bias and (II) to compare the different strategies for identifying the areas of high dynamical activity and accordingly designing the computational mesh.

Besides scientific aims, the elaboration of the physical core of FESOM also includes seeking for cheaper numerical solutions in order to get most out of existing computer resources.

1 AWI-CM descripton

The sea ice-ocean component (FESOM v.1.4), which is based on unstructured mesh technique has been already described and validated in numerous studies with prescribed atmospheric forcing (see e.g. Danilov et al., 2004; Wang et al., 2008; Timmermann et al., 2009, Sidorenko et al., 2011, Wang et al., 2014). AWI-CM climate model is built upon FESOM and coupled with the latest version of ECHAM6.3 atmosphere from the Max Planck

Institute for Meteorology, Hamburg. The coupling between FESOM and ECHAM6 is achieved via the parallel OASIS3-MCT coupler.

Earlier versions of AWI-CM are described in *Sidorenko et al., 2014* and *Rackow et al., 2015* and the system is currently used in a broad spectrum of research activities starting with the analysis of the modeled El Niño-Southern Oscillation (ENSO) and ending with the analysis of biases in the Labrador Sea and sensitivity experiments on the response of the climate system to vanishing Arctic sea-ice *(Semmler et al., 2016)*.

2 AWI-CM results

It has been shown (see eg. *Sidorenko et al., 2014*) that under the moderate oceanic resolution of 1° AWI-CM shares similar biases with most of the climate models participating in CMIP5. Because of this, a few FESOM configurations with different resolutions have been tested with AWI-CM in order to investigate the influence of local refinement onto the climate model bias. Two of these ocean configurations are shown in Figure 1.

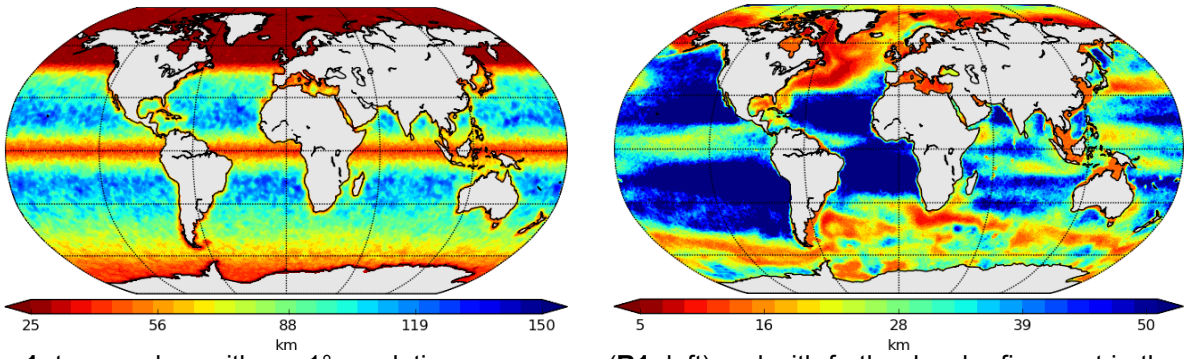

Fig. 1: two meshes with ca. 1° resolution on average (**R1**, left) and with further local refinement in the dynamically active regions (**R2**, right). The colorbar range is different!

The R1 mesh has been used by us for the comparison of FESOM with other ocean-only models under Coordinated Ocean-ice Reference Experiments - Phase II (CORE2) forcing. It has been demonstrated that FESOM performs well in this configuration compared to other participating ocean models (Griffies et al., 2014; Danabasoglu et al., 2014).

The R2 mesh has been refined in dynamically active regions which are identified from the mean variance of the sea surface height from altimetry products. The ocean-only simulations with FESOM using numerical grids based on such approach have a good potential to improve the simulated ocean state as has been shown in *Sein et al. 2016.*

Figure 2 depicts the departure of the global mean profiles of simulated hydrography from the WOA2005 climatology for the AWI-CM model runs using R1 and R2 meshes. It shows that the bias in R2 is partially reduced compared to R1 and suggests, that the coupled modelling may benefit from properly resolved oceanic features. The identification of key regions which need to be refined and the required resolution in those regions is still under debate.

The R2 mesh design was constrained by the total amount of surface nodes because of efficiency reasons. In view of this, the Rossby radius of deformation is still not fully resolved in most of the ocean and the model bias does not fully vanish.

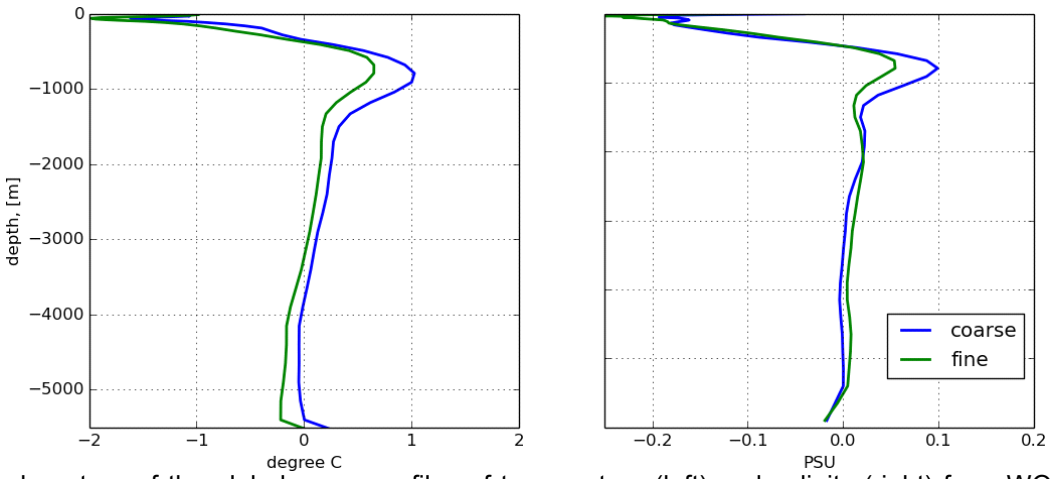

Fig. 2: departure of the global mean profiles of temperature (left) and salinity (right) from WOA2005 climatology. The increased resolution in the ocean reduces the bias in hydrography.

3 Technical achievements

A new dynamical core for FESOM v.2.0 based on the finite volume approach with the cell centered placement of horizontal velocities (quasi-B-grid) has been implemented and promises a significant improvement in the performance of the ocean component (a factor of 3 model speedup is expected). At the moment, FESOM v.2.0 is used in the ocean-only setting and has been run under CORE II forcing (60 years of surface data) using different ocean grids. The comparison of FESOM v.2 against v1.4 shows that the physics of the new version is properly reproduced. However, in order to use the full potential of the new setup it is still required to test its performance on meshes which are too large and expensive for being used with FESOM v.1.4. As soon as all necessary validations are made, FESOM v.2.0 will replace v.1.4 in AWI-CM.

4. Works published within the project

The validation of earlier versions of AWI-CM in simulating mean climate and variability has been summarized in Sidorenko et al., 2015 and Rackow et al., 2016. The ongoing work and debates on designing ocean meshes with variable resolution led to a recently summarized study by Sein et al. 2016. Besides that, AWI-CM is used in various research activities one of them being the influence of Arctic sea ice on the atmosphere and ocean circulation (Semmler et al., 2016; Campos et al., 2016). Two masters theses have been carried out on this topics (Stulic, 2015; Campos, 2015). Furthermore, predictability studies have been performed in the framework of the Arctic Predictability and Prediction On Seasonal to Inter-annual Timescales (APPOSITE) project (Goessling et al., 2016; Day et al., 2015). Lastly, we are part of the High Resolution Model Intercomparison Project (HighResMIP) within the Coupled Model Intercomparison Project 6 (CMIP6) (Haarsma et al., 2016) for which we carried out preparatory simulations on HLRN.

References

Campos, C. (2015), *Assessment of Arctic Ocean Circulation Sensitivity to Sea Ice Decline. Thesis paper at the University of Bremen.*

Campos, C., Semmler, T., Jung, T. (2016), *Influence of Arctic sea ice decline on the global ocean circulation. In preparation for Journal of Climate.*

Danabasoglu, G. and others (2014), North Atlantic simulations in Coordinated Ocean-ice Reference Experiments phase II (CORE-II). Part I: Mean states, Ocean Modelling, 73 , pp. 76-107. doi:10.1016/j.ocemod.2013.10.005

Danilov S., G. Kivman, and J. Schröter (2004), *A finite-element ocean model: principles and evaluation, Ocean Modell.*, 6(2):125–150

Day, J. J., Tietsche, S., Collins, M., Goessling, H. F., Guemas, V., Guillory, A., Hurlin, W. J., Ishii, M., Keeley, S. P. E., Matei, D., Msadek, R., Sigmond, M., Tatebe, H., and Hawkins, E. (2015), *The Arctic Predictability and Prediction on Seasonal-to-Interannual TimEscales (APPOSITE) data set. Geosci. Model Dev. Discuss.,* 8, 8809-8833, 2015.

Goessling, H. F., Tietsche, S., Day, J. J., Hawkins, E., and Jung, T. (2016), *Predictability of the Arctic sea ice edge. Geophysical Research Letters,* doi: 10.1002/2015GL067232.

Griffies, S. and others (2014) , *An assessment of global and regional sea level for years 1993–2007 in a suite of interannual CORE-II simulations, Ocean Modelling*, 78 , 35-89 . doi:10.1016/j.ocemod.2014.03.004

Haarsma, R. J., Roberts, M., Vidale, P. L., Senior, C. A., Bellucci, A., Corti, S., Fuckar, N. S., Guemas, V., von Hardenberg, J., Hazeleger, W., Kodama, C., Koenigk, T., Leung, L. R., Lu, J., Luo, J.-J., Mao, J., Mizielinski, M. S., Mizuta, R., Nobre, P., Satoh, M., Scoccimarro, E., Semmler, T., Small, J., and von Storch, **J.-S.** (2016), *High Resolution Model Intercomparison Project (HighResMIP). Submitted to Geophysical Model Development.*

Rackow, T., Goessling, H., Jung, T., Semmler, T., Sidorenko, D., Barbi, D., Handorf, D., 2015. *Towards multi-resolution global climate modeling with ECHAM6-FESOM. Part II: Climate variability. Submitted to Clim. Dyn.*

Sein, D., Danilov, S., Biastoch A., Durgadoo J., Sidorenko D., Harig S., Wang Q., (2016), *Designing variable ocean model resolution based on the observed ocean variability. Submitted to JAMES.*

Semmler, T., L. Stulic, T. Jung, N. Tilinina, C. Campos, S. K. Gulev, and D. Koracin (2016), *Seasonal atmospheric responses to reduced Arctic sea ice in an ensemble of coupled model simulations. Journal of Climate, in press.*

Sidorenko, D. , Rackow, T. , Jung, T. , Semmler, T. , Barbi, D. , Danilov, S. , Dethloff, K. , Dorn, W. , Fieg, K. , Gößling, H. F. , Handorf, D. , Harig, S. , Hiller, W. , Juricke, S. , Losch, M. , Schröter, J. , Sein, D. and Wang, Q. (2015), *Towards multi-resolution global climate modeling with ECHAM6–FESOM. Part I: model formulation and mean climate, Climate Dynamics*, doi:10.1007/s00382-014-2290-6

Stulic, L. (2015), *Impact of removed Arctic Summer Sea Ice on atmosphere and ocean circulation in an ensemble of coupled model simulations. Master's thesis at the University of Split, Croatia.*

Timmermann R., S. Danilov, J. Schröter, C. Böning, D. Sidorenko, and K. Rollenhagen (2009), *Ocean circulation and sea ice distribution in a finite element global sea ice-ocean model, Ocean Modell., 27 (3-4), 114-129.*

Wang Q., S. Danilov, and J. Schröter (2008), *Finite element ocean circulation model based on triangular prismatic elements, with application in studying the effect of topography representation, J. Geophys Res., 113, C05015*, doi:10.1029/2007JC004482.

Wang, Q. , Danilov, S. , Sidorenko, D. , Timmermann, R. , Wekerle, C. , Wang, X. , Jung, T. and Schröter, J. (2014) , *The Finite Element Sea Ice-Ocean Model (FESOM) v.1.4: formulation of an ocean general circulation model, Geoscientific Model Development*, 7 (2), 663-693. doi:10.5194/gmd-7-663-2014

6.9.1 *hbk00034:* Ice sheet – ice shelf – ocean interaction in the marginal seas of the Southern Ocean

HLRNProject ID:	hbk00034
Run time:	III/2013-III/2016
Project Leader:	Prof. Dr. Torsten Kanzow
Project Scientists:	Mathias van Caspel, Marta Kasper, Yoshihiro Nakayama, Svenja Ryan, Lukrecia Stulic, Ralph Timmermann
Affiliation:	University of Bremen and Alfred Wegener Institute, Bremerhaven

Overview

In this project, we use a global sea ice – ice shelf – ocean model to study the interaction between the deep Southern Ocean, the ice shelves fringing the Antarctic continent, and the Antarctic Ice Sheet. With its unstructured grid, the Finite Element Sea ice Ocean Model (FESOM) allows for an adequate resolution of the key regions, namely the grounding lines, the ice shelf fronts, and the continental shelf break. Special emphasis is laid on a correct representation of water mass exchange between the deep ocean and the continental shelf in the Weddell Sea, and the pathways of water in the cavity beneath Filchner-Ronne Ice Shelf (FRIS). Coupling with an efficient ice sheet/shelf model is one of the focus activities in this project and will allow for a complete and consistent representation of ocean – ice sheet interaction in decadal to centennial-scale simulations. With the high computational burden imposed by the use of a finite-element ocean model (to which there is no alternative if local processes are to be represented in a global system), the project depends on resources provided through the HLRN.

Results

Substantial progress has been made with respect to coupling FESOM with the Revised Ice Model Based on frAnk pattYn (RIMBAY). Time-slice experiments in which RIMBAY was forced with ice shelf basal melt rates from the FESOM scenario experiments of Timmermann and Hellmer (2013) have been succesfully completed and indicate that the sensitivity of the area-integrated ice shelf basal mass loss to moderate variations of the thickness distribution is lower than is often assumed in the scientific community. We have presented our findings on international conferences; a peer-reviewed paper is currently being prepared.

Experience gained from and the infrastructure developed for these time-slice experiments were utilized in the implementation of the coupled Regional Antarctic and Global Ocean (RAnGO) model. The current RAnGO setup is based on a global FESOM configuration with an eddy-permitting mesh in the Weddell Sea sector of the Southern Ocean and an even further refinement in the sub-ice cavities. It is coupled to a RIMBAY implementation that comprises the Filchner Ronne Ice Shelf (FRIS) and the ice streams in its catchment area up to the ice divides with a terrain-following vertical coordinate and 10 km horizontal resolution. Due to the vast difference between the time scales relevant for ocean and ice sheet processes, coupling is done in an asynchronous way with a one-year interval, using annual mean FESOM melt rates to compute a new RIMBAY ice shelf geometry, which is then passed back to FESOM. The fact that variations of RIMBAY ice thickness distribution,

grounding line location, and melt rate patterns are small for each coupling time step indicates that this coupling strategy is adequate.

While adjustment of the model domain to a modified ice shelf geometry is a natural part of RIMBAY and is rather straightforward for a finite-difference model ocean model with a land-sea mask, the FESOM mesh only exists in the ocean and has to satisfy certain criteria in order to ensure computational stability. To avoid an overly large overhead, we initially generated a grid that covers the full region that may potentially become “ocean” during the course of the integration. Mesh resolution in this potentially ungrounded area is about 1.5 km to describe grounding line migration as smoothly as possible. Model runs are then initialized with a (quasi) steady-state ice shelf geometry from RIMBAY, removing grid nodes in areas with grounded ice, renumbering nodes accordingly, and then subsequently restoring pre-computed elements in areas where thegrounding line retreats (or removing further elements in places where formerly floating ice becomes grounded). During this procedure, the vast majority of finite element mesh nodes keep their position (despite being renumbered), so that no horizontal interpolation is necessary for the ocean state variables, which makes it much easier to ensure the conservation of heat and salt.

Coupling has been implemented in an “offline” way with RIMBAY and the RAnGO coupler running on AWI computers and only FESOM relying on HLRN resources. Given that (1) FESOM output is in any case transfered to AWI computers for postprocessing and analysis and that (2) the updated configuration files are not very big, the overhead arising from the file transfer necessary in the offline approach is in fact very very small.

We are currently running a RAnGO experiment with forcing from the HadCM3 coupled climate model. FRIS basal melt rates from the last decade of a fifty-year present-day FESOM run with BEDMAP-2 ice shelf geometry have been used as a boundary condition to a 1000-yr RIMBAY simulation, providing an ice shelf geometry that is very close to a steady state. This “equilibrium” geometry has been used to restart FESOM with (1) fixed ice shelf geometry and (2) as part of the coupled RAnGO model. The ice thickness distribution after 15 years of coupled simulation with present-day forcing along with the data from BEDMAP-2 are shown in Fig. 1.

Given that (1) model studies have shown that the density distribution on the Weddell Sea continental shelf critically affects the circulation of water between the deep ocean and the sub-ice cavity, and that (2) the properties and thus the density of shelf water masses are largely shaped by the salt input related to sea ice formation, the quantification of sea ice production in the southern Weddell Sea using a synergy of numerical simulations and remote sensing data is another focus effort in this project. We aim to improve estimates of the sea ice production and high salinity shelf water (HSSW) formation in the southern Weddell Sea for the period 2002-2012. Coastal polynyas cover only 1% of the area, but contribute about 10% to the total winter sea ice production; their characteristics and the rate of HSSW formation have been shown to be very sensitive to the atmospheric forcing conditions.

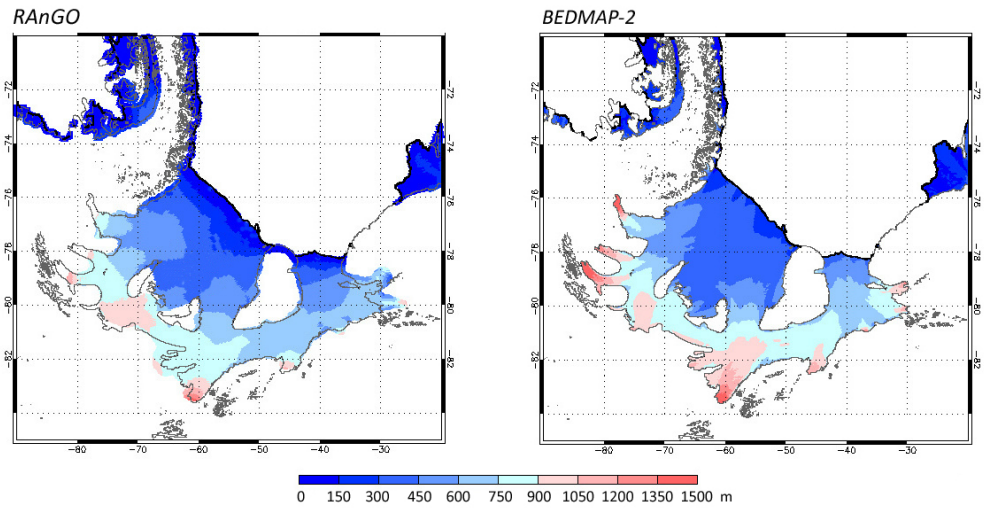

Fig. 1: Ice shelf draft (thickness below sea level) in RAnGO after 15 years of coupled simulation (left panel) and derived from BEDMAP-2 data (right panel). The black lines in both panels represent the BEDMAP-2 ice shelf boundaries and indicate a good agreement between model and observations.

In order to assess the robustness of FESOM simulations of sea ice production, we conducted experiments using ERA-Interim (1979-2012) and NCEP-CFSR (1979-2010) reanalysis data sets as atmospheric forcing data. In all cases, FESOM was run on the same global grid with a resolution varying between 250km in the open ocean and around 10 km at the Weddell Sea coast area.

Simulated sea ice net freezing rates for four months in the freezing seasonsof 2002-2010 are shown in Figures 2 and 3. A persistent band of high growth rates can be seen along the coastline/ice shelf front in the southern Weddell Sea in both cases. However, mean sea ice growth is lower in the CFSR run and more localized along the coastline/ice shelf front when compared to the results from ERA-Interim run. Differences may be attributed to the colder air temperatures and stronger southerly winds over large areas of the southern Weddell Sea in the ERA-Interim forcing that favor more pronounced sea ice growth over a wider area, while the NCEP-CFSR simulation represents the cooling effect of the Antarctic ice sheet much more locally. A combination of different observational data sets will allow us to identfy which of the distributions (and thus which of the forcing data sets) is more realistic.

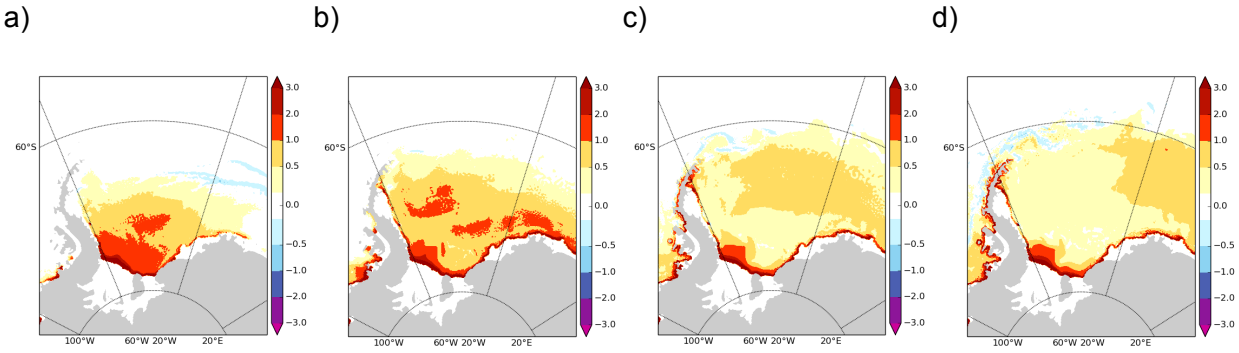

Figure 2: Sea ice net freezing rates [cm/d] from FESOM simulations with ERA-Interim forcing for a) March, b) April, c) May and d) June averaged over 2002-2010.

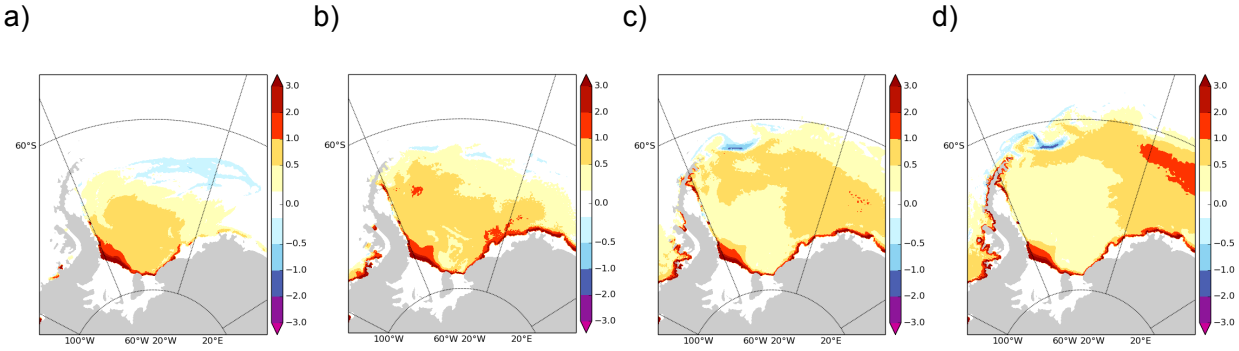

Figure 3: Sea ice net freezing rates [cm/d] from FESOM simulations with NCEP-CFSR forcing for a) March, b) April, c) May and d) June averaged over 2002-2010.

Outlook

RAnGO simulations are being continued using data from the HadCM3-A1B scenario until the end of the 22nd century. Two control simulations with (1) atmospheric forcing of the 20th century and (2) fixed cavity geometry applied throughout the 21st and 22nd centuries of the model simulations will help to separate the effect of climate change from the feedback related to a varying cavity geometry. An analysis of results from the ice sheet component will yield robust estimates of the contribution of this sector of the Antarctic Ice Sheet to future sea level rise. Further effort concentrates on an eddy-resolving model of the Weddell Sea and an assessment of the role of the Larsen A, B and C ice shelves in the western Weddell Sea for the formation of Antarctic Bottom Water.

Publications

- van Caspel, M.R., Absy, J.M., Wang, Q., Hellmer, H.H. and Schröder, M., *The Flow of Dense Water Plumes in the Western Weddell Sea Simulated with the Finite Element Ocean Model (FEOM), in: Towards an Interdisciplinary Approach in Earth System Science, (Springer Earth System Sciences), Heidelberg [u.a.], Springer International Publishing, 251 pp., doi:10.1007/978-3-319-13865-7_14 (2015)*

- Cornford, S.L., Martin, D.F., Payne, A.J., Ng, E.G., Le Brocq, A.M., Gladstone, R.M., Edwards, T.L., Shannon, S.R., Agosta, C., van den Broeke, M.R., Hellmer, H.H., Krinner, G., Ligtenberg, S.R.M., Timmermann, R. and Vaughan, D.G.,*Century-scale simulations of the response of the West Antarctic Ice Sheet to a warming climate, The Cryosphere, 9 (4), pp. 1579-1600 (2015)*
- Danilov, S., Wang, Q., Timmermann, R., Iakovlev, N., Sidorenko, D., Kimmritz, M., Jung, T. and Schröter, J.,*Finite-Element Sea Ice Model (FESIM), version 2 , Geosci. Model Dev., 8 , pp. 1747-1761 (2015)*
- Nakayama, Y., *Analysis and modeling of the distribution of tracers of glacial melt in the Southern Ocean with focus on the Southeast Pacific sector, PhD thesis, University of Bremen* (2015)
- Timmermann, R., Goeller, S. and Grosfeld, K.,*Veränderungen im südlichen Weddellmeer beeinflussen den globalen Meeresspiegel, REKLIM News* (2015)

Presentations

1. van Caspel, M., Timmermann, R., Schröder, M. and Hellmer, H., Formation of Antarctic bottom water on the continental shelf off Larsen Ice Shelf, 26th General Assembly of the International Union of Geodesy and Geophysics (IUGG General Assembly), Prague, 22 June - 2 July 2015
2. Goeller, S., Timmermann, R. and Thoma, M., The response of the West Antarctic Ice Sheet to ocean warming beneath the Filchner-Ronne Ice Shelf, REKLIM Workshop, Neumünster, Germany, 18 May 2015 - 20 May 2015
3. Goeller, S., Timmermann, R., Thoma, M. and Grosfeld, K.,West Antarctic Ice Sheet response to ocean warmin in the Filchner Ronne Ice Shelf Region, 26. Internationale Polartagung, Bayerische Akademie der Wissenschaften, München, 6 September - 11 September 2015
4. M. Kasper, Impact of highly resolved atmospheric forcing on the Southern Ocean circulation using the Finite Element Sea-ice Ocean Model (FESOM), International Symposium on Contemporary Ice-Sheet Dynamics: ocean interaction, meltwater and non-linear effects, Cambridge, Cambridge, UK, 16–21 August 2015
5. Timmermann, R. and Goeller, S.,Sensitivity of ice shelf basal melt rates to a varying thickness distribution, EGU General Assemby, Vienna, 12 April 2015 - 17 April 2015
6. Timmermann, R., Goeller, S. and Thoma, M., Response of the cryosphere to ocean warming below Filchner Ronne Ice Shelf (Antarctica), 26th General Assemby, Prague, 22 June 2015 - 2 July 2015

6.10 *hbk00037:* Schwankungen des tropischen Regengürtels während des mittleren Miozäns

HLRN Projekt-ID:	hbk00037
Laufzeit:	III/2014-II/2015
Projektleiter:	Prof. Dr. M. Schulz
Projektbearbeiter:	A. Frigola, Dr. M. Prange
Institut/Einrichtung:	DFG-Forschungszentrum / Exzellenzcluster „Der Ozean im System Erde“ (MARUM), Universität Bremen

Kurzfassung

- Vor ca. 14 Millionen Jahren wuchs der antarktische Eisschild abrupt an.
- Geologische Befunde zeigen, dass zur selben Zeit starke Veränderungen in tropischen Niederschlägen stattfanden.
- Mit Hilfe eines komplexen Klimamodells wurde untersucht, inwieweit Änderungen des antarktischen Eisschildes die Tropen beeinflussen können.
- Die Untersuchung von Wechselwirkungen zwischen den Tropen und Polarregionen soll helfen, die Bedeutung sich verändernder Eisschilde für das globale Klimasystem in der Zukunft besser zu verstehen.

Wissenschaftlicher Hintergrund

Paläoklimatische Befunde zeigen, dass der tropische Regengürtel in der Erdgeschichte immer wieder erheblichen Schwankungen unterworfen war. Insbesondere deuten geowissenschaftliche Rekonstruktionen begleitet von Klimamodellstudien auf Nord-Süd-Verlagerungen des tropischen Regengürtels auf der Jahrtausend- und der orbitalen Zeitskala hin (z.B. Collins et al., 2011; Schefuß et al., 2011; Zarriess et al., 2011; Bouimetarhan et al., 2012; Handiani et al., 2013; Mohtadi et al., 2014; Steinke et al., 2014; Govin et al., 2014; Rachmayani et al., 2015). Als Ursache für diese Schwankungen wurden, abhängig von der Zeitskala, variierende Sonneneinstrahlung (durch Änderungen der Erdorbitalparameter) und Schwankungen in der großräumigen Ozeanzirkulation identifiziert. Für Zeitskalen von Jahrmillionen wurde die Hypothese aufgestellt, dass asymmetrische Vereisung der Polkappen ebenfalls zu Verlagerung des tropischen Regengürtels geführt haben könnte. Obgleich Hypothesen hinsichtlich des Einflusses unipolarer Vereisung während der Erdgeschichte auf tropische Winde und Niederschläge schon früh formuliert wurden, konnten diese Prozesse in Klimamodellen bislang nur unzureichend untersucht werden. Untermauert wurde die Hypothese einer Verlagerung des tropischen Regenbandes durch die antarktische Vereisung jüngst durch geochemische Untersuchungen an Ablagerungen aus dem Südchinesischen Meer, die das Zeitintervall des mittleren Miozäns (ca. 17 bis 12 Millionen Jahre vor heute) beleuchten (Holbourn et al., 2010). Das mittlere Miozän war geprägt durch global höhere Temperaturen und Treibhausgaskonzentrationen als heute. Eismassen waren auf der Nordhemisphäre kaum vorhanden und der antarktische Eisschild war deutlich kleiner

als heute. Vor ca. 14 Millionen Jahren fand schließlich eine erhebliche Ausdehnung der antarktischen Eismassen statt, begleitet von einer vermuteten Abnahme des atmosphärischen CO_2-Gehalts. Der Meeresspiegel sank entsprechend um mehrere Zehnermeter (Holbourn et al., 2005; Langebroek et al., 2010). Anhand von Oberflächensalzgehaltsrekonstruktionen konnte eine Abnahme der Salzgehalte im Südchinesischen Meer während des mittleren Miozäns festgestellt werden (Holbourn et al., 2010). Die Autoren erklären diese Salzgehaltsabnahme mit erhöhten Niederschlägen aufgrund einer sukzessiven Verlagerung des tropischen Regengürtels nach Norden infolge antarktischen Eiswachstums (unipolare Vereisung) im mittleren Miozän.

Methode

Mit Hilfe von numerischen Experimenten mit dem komplexen Klimamodell CCSM3 (Community Climate System Model version 3) wurde der Einfluss des antarktischen Eisschildes auf den tropischen Regengürtel untersucht. Das voll gekoppelte globale Klimamodell CCSM3 besteht aus Teilkomponenten für die Simulation von Atmosphäre, Ozean, Meereis sowie Landoberflächenprozessen. Aus technischer Sicht ist es ein MPMD-Modell ('Multiple-Program-Multiple-Data'), dass für Hybrid-Parallelisierung unter Verwendung von MPI und OpenMP konzipiert wurde. Zur Simulation des miozänen Klimas wurden Randbedingungen bezüglich Vegetationsbedeckung, Land-See-Verteilung, Eisschildausdehnung, Topografie und atmosphärischer Treibhausgaskonzentrationen zusammengestellt und dem Klimamodell vorgeschrieben. Dabei wurde der neuste geologische und paläozeanografische Kenntnisstand berücksichtigt, insbesondere im Hinblick auf den globalen Meeresspiegel und Gebirgsbildung.

Neben einem Kontrollexperiment für das heutige Klima wurden folgende Experimente zur Untersuchung miozäner Klimaänderungen und den Einflüssen des antarktischen Eisschildes sowie der atmosphärischen Treibhausgaskonzentration wie geplant durchgeführt: (i) Simulation des miozänen Klimas vor dem Schub der antarktischen Eisausdehnung (d.h. partiell vereiste Antarktis mit relativ kleinen Eiskappen über dem Transantarktischen Gebirge und der östlichen Antarktis) mit 400 ppm atmosphärischer CO_2-Konzentration, (ii) Simulation des miozänen Klimas nach der antarktischen Eisausdehnung (d.h. vollständige Vereisung der Antarktis) und CO_2-Abnahme auf 200 ppm, (iii) Sensitivitätsexperiment mit partiell vereister Antarktis und geringer atmosphärischer CO_2-Konzentration (200 ppm), (iv) Sensitivitätsexperiment mit vollständiger antarktischer Vereisung und hoher CO_2-Konzentration (400 ppm). Alle Klimasimulationen wurden hinreichend lang integriert, damit sich klimatische Gleichgewichte einstellen konnten.

Ergebnisse

Abbildung 1a zeigt exemplarisch die Oberflächentemperatur-Differenz zwischen dem Experiment mit vollständiger antarktischer Vereisung und hoher CO_2-Konzentration und dem Experiment mit partieller Vereisung bei gleicher CO_2-Konzentration, d.h. die Antwort der weltweiten Oberflächentemperatur auf eine antarktische Eisausdehnung. Mit dickerem und ausgedehnterem Eisschild findet erwartungsgemäß eine Abkühlung direkt über dem antarktischen Kontinent statt. Die Südhemisphäre und insbesondere das Südpolarmeer erwärmen sich hingegen an der Oberfläche, während die nördlichen Extratropen weitgehend abkühlen. Im tropischen Pazifik fällt eine Temperaturzunahme entlang des Äquators auf, die vermutlich auf Advektion von erwärmten Wassermassen aus höheren südlichen Breiten (Subantarktisches Modewasser und Antarktisches Zwischenwasser) unterhalb der Oberfläche und Aufquellen dieser Wassermassen am Äquator zurückzuführen ist. Die wärmeren Oberflächentemperaturen begünstigen atmosphärische Konvektion und führen

somit zu einer Zunahme äquatorialer Niederschläge wie in Abbildung 1c gezeigt. Eine meridionale (Nord-Süd) Verschiebung des tropischen Regengürtels zeigt sich aber nicht. Abbildung 1b zeigt die Oberflächentemperatur-Differenz zwischen dem Experiment mit vollständiger antarktischer Vereisung und verringerter CO_2-Konzentration (200 ppm) und dem Experiment mit partieller Vereisung und hoher CO_2-Konzentration (400 ppm), d.h. die Antwort der Oberflächentemperatur auf antarktische Eisausdehnung und gleichzeitiger CO_2-Abnahme, so wie es in der Erdgeschichte stattgefunden hat. Aufgrund des verringerten Treibhauseffekts zeigt sich eine globale Abkühlung an der Oberfläche einschließlich des äquatorialen Pazifiks, so dass Niederschläge fast überall (einschließlich der Tropen) abnehmen (Abbildung 1c). Eine meridionale Verlagerung des tropischen Regenbandes findet auch in diesem Experiment nicht statt. Interessanterweise zeigen beide Experimente eine Zunahme der Niederschläge über dem Südchinesischen Meer (ohne Abbildung) infolge der antarktischen Eisausdehnung im Einklang mit Sedimentkerndaten (siehe oben). Allerdings zeigt das Klimamodell, dass diese Niederschlagszunahme lediglich ein regionales Phänomen ist und nicht im Zusammenhang mit einer meridionalen Verlagerung des tropischen Regengürtels steht, wie zuvor postuliert wurde (Holbourn et al., 2010).

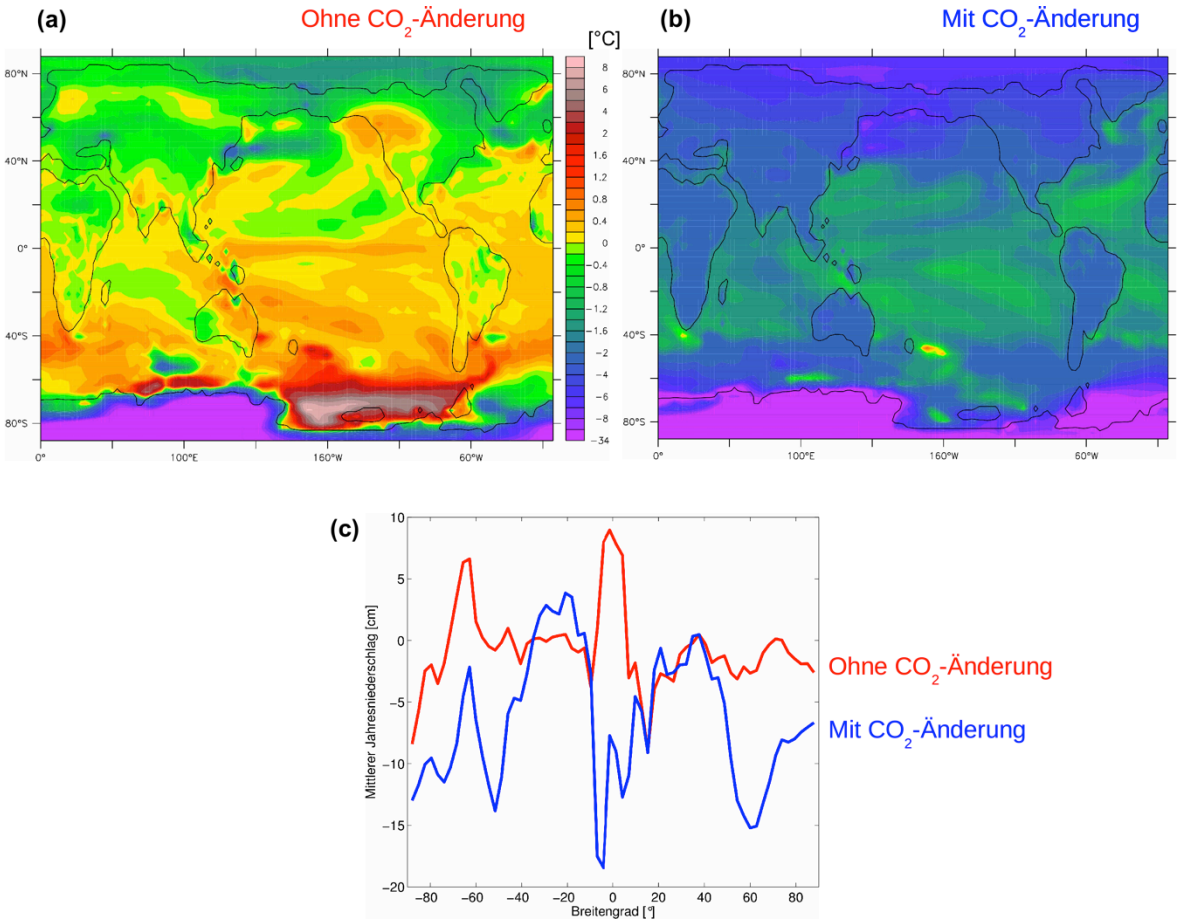

Abbildung 1. (a, b) Differenzen in Oberflächentemperaturen im 30-jährigen Jahresmittel simuliert mit dem globalen Klimamodell CCSM3. **(a)** Temperaturänderungen infolge des Wachsens des antarktischen Eisschildes im mittleren Miozän. **(b)** Wie (a), aber mit zusätzlicher Reduktion der atmosphärischen CO_2-Konzentration von 400 ppm auf 200 ppm. **(c)** Dazugehörige Differenzen in zonal gemittelten Jahresniederschlägen. In (a) und (b) sind die Umrisse der Kontinente vor ca. 15 Millionen Jahren eingezeichnet.

Zurzeit finden detaillierte Analysen der Modelldaten statt (z.B. zur genauen physikalischen Erklärung der Oberflächentemperaturfelder und der Niederschlagsanomalien). Aber schon jetzt zeichnet sich ab, dass die Ausdehnung antarktischer Eismassen während des Miozäns einen anderen Einfluss auf das tropische und extratropische Klima hatte als erwartet, und dass paläoklimatische Rekonstruktionen teilweise neu interpretiert werden müssen. Die Ergebnisse sind insbesondere im Hinblick auf zukünftiges Abschmelzen von Teilen polarer Eisschilde von Bedeutung, um einen möglichen Einfluss z.B. auf den tropischen hydrologischen Zyklus besser bewerten zu können.

Referenzliste (Projektleiter/-bearbeiter **fett** gedruckt)

Bouimetarhan, I., **M. Prange**, E. Schefuß, L. Dupont, J. Lippold, S. Mulitza, and K. Zonneveld, 2012: Sahel megadrought during Heinrich Stadial 1: evidence for a three-phase evolution of the low- and mid-level West African wind system. Quaternary Science Reviews, 58, 66-76.

Collins, J. A., E. Schefuß, D. Heslop, S. Mulitza, **M. Prange**, M. Zabel, R. Tjallingii, T. M. Dokken, E. Huang, A. Mackensen, **M. Schulz**, J. Tian, M. Zarriess, and G. Wefer, 2011: Interhemispheric symmetry of the tropical African rainbelt over the past 23,000 years. Nature Geoscience, 4, 42-45.

Govin, A., V. Varma, and **M. Prange**, 2014: Astronomically forced variations in western African rainfall (21°N-20°S) during the Last Interglacial period. Geophysical Research Letters, 41, 2117-2125, doi:10.1002/2013GL058999.

Handiani, D., A. Paul, **M. Prange**, U. Merkel, L. Dupont, and X. Zhang, 2013: Tropical vegetation response to Heinrich Event 1 as simulated with the UVic ESCM and CCSM3. Climate of the Past, 9, 1683-1696, doi:10.5194/cp-9-1683-2013.

Holbourn, A., W. Kuhnt, M. Regenberg, **M. Schulz**, A. Mix, and N. Andersen, N., 2010: Does Antarctic glaciation force migration of the tropical rain belt? Geology, 38, 783-786, doi:10.1130/G31043.1.

Holbourn, A., W. Kuhnt, **M. Schulz**, and E. Erlenkeuser, 2005: Impacts of orbital forcing and atmospheric carbon dioxide on Miocene ice-sheet expansion. Nature, 438, 483-487.

Langebroek, P., A. Paul, and **M. Schulz**, 2010: Simulating the sea-level imprint on marine oxygen-isotope records during the Middle Miocene using an ice sheet-climate model. Paleoceanography, 25, PA4204, doi:10.1029/2008PA001704.

Mohtadi, M., **M. Prange**, D. W. Oppo, R. De Pol-Holz, U. Merkel, X. Zhang, S. Steinke, and A. Lückge, 2014: North Atlantic forcing of tropical Indian Ocean climate. Nature, 509, 76-80, doi:10.1038/nature13196.

Rachmayani, R., **M. Prange**, and **M. Schulz**, 2015: North African vegetation-precipitation feedback in early and mid-Holocene climate simulations with CCSM3-DGVM. Climate of the Past, 11, 175-185, doi:10.5194/cp-11-175-2015.

Schefuß, E., H. Kuhlmann, G. Mollenhauer, **M. Prange**, and J. Pätzold, 2011: Forcing of wet phases in southeast Africa over the past 17,000 years. Nature, 480, 509-512, doi:10.1038/nature10685.

Steinke, S., M. Mohtadi, **M. Prange**, V. Varma, D. Pittauerova, and H. W. Fischer, 2014: Mid- to Late-Holocene Australian-Indonesian summer monsoon variability. Quaternary Science Reviews, 93, 142-154, doi:10.1016/j.quascirev.2014.04.006.

Zarriess, M., H. Johnstone, **M. Prange**, S. Steph, J. Groeneveld, S. Mulitza, and A. Mackensen, 2011: Bipolar seesaw in the northeastern tropical Atlantic during Heinrich stadials. Geophysical Research Letters, 38, L04706, doi:10.1029/2010GL046070.

6.11 *hbk00038:* Interaction between marine terminating glaciers and the ocean circulation in Northeast Greenland

HLRNProject ID:	hbk00038
Run time:	III/2014 – III/2016
Project Leader:	Prof. Torsten Kanzow[1,2]
ProjectScientists:	Janin Schaffer[2], Ralph Timmermann[2], ClaudiaWekerle[2]
Affiliation:	[1] University of Bremen [2] Alfred Wegener Institute, Helmholtz Centre for Polar and Marine Research

Overview

The ocean plays an important role in modulating the mass balance of the Greenland Ice Sheet by delivering heat to the marine-terminating outlet glaciers around Greenland [1]. The warming and accumulation of Atlantic Water in the subpolar North Atlantic [2] has been suggested to be the driver of the glaciers' retreat around the coast of Greenland [3]. The continental shelf regions are the obvious gateways between the glacial fjords and the open ocean and thus play a critical role for the transport of Atlantic Water towards the glaciers.

A key region for the mass balance of the Greenland Ice Sheet is the Northeast Greenland Ice Stream. This large ice stream drains the second-largest basin of the Greenland Ice Sheet and feeds three outlet glaciers [4]. The largest of the outlet glaciers is Nioghalvfjerdsfjorden Glacier (79°N-Glacier) featuring a 80 km long floating ice tongue [5]. A complex bathymetry steers the flux of warm water of Atlantic origin from the open ocean onto the continental shelf [6] and into the sub-glacial cavity of the 79°N-Glacier [5]. We analysed historic and recent hydrographic observations in the Northeast Greenland shelf region and found that these Atlantic waters, both on the continental shelf and in the cavity, have become warmer by about 0.5° C during the last two decades.

In order to study the relevant processes of glacier-ocean interaction we carry out experiments with the finite-element sea ice-ocean model (FESOM). There are two main goals in this HLRN project: First, we aim to investigate the warm water transport onto and the circulation on the Northeast Greenland continental shelf. A requirement for a realistic simulation is a good representation of the recirculating Atlantic Water in Fram Strait and of the East Greenland Current (see sketch in Fig. 1). Secondly, we will study the warm water transport into the glacier cavities and the spreading of basal melt water on the continental shelf and into the deep ocean.

FESOM consists of a finite element ocean model [7], coupled to a dynamic-thermodynamic finite-element sea ice model [8]. It uses unstructured triangular meshes in the horizontal, and tetrahedral elements in the volume. We use two different model configurations. Both configurations have a horizontal resolution of about 1° in the bulk of the global ocean, 0.5° along the coastlines, and 24 km in the North Atlantic. In the first configuration we apply a mesh with 4.5 km resolution in the Arctic Ocean and Nordic Seas to better resolve the flow of Atlantic Water into and the flow out off the Arctic. In the second configuration we use a mesh with a coarser resolution in the Central Arctic (16 km), but a finer resolution on the continental shelf of Northeast Greenland (2.5 km), in front of the glacier (1.2 km) and in the

glacier cavity (600 m). The first configuration is fully operational and has produced the results discussed below.

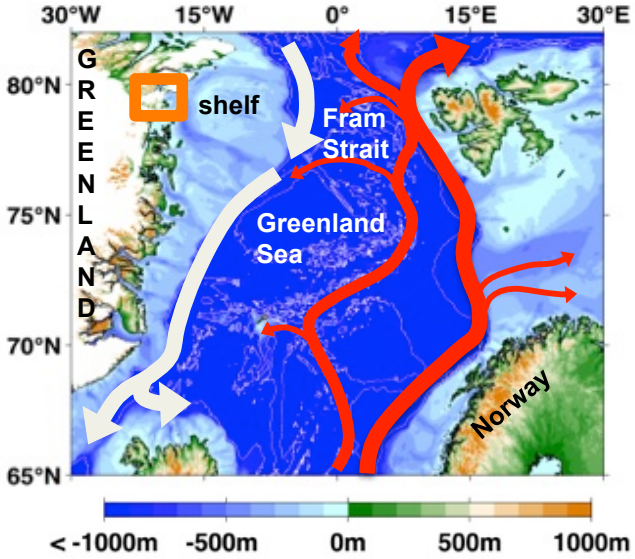

Fig. 1: Schematic of the circulation in the Nordic Seas. Red arrows indicate pathways of the flow of Atlantic Water into the Arctic, grey arrows indicate the flow of modified Atlantic and Arctic waters out of the Arctic. The orange box marks the region of the 79° N-Glacier.

Results

The 40-year FESOM run with CORE-2 forcing represents the West Spitsbergen Current and the East Greenland Current realistically. These currents are of major interest because they determine the transport of Atlantic Water through Fram Strait and onto the Northeast Greenland shelf. However, the recirculation in Fram Straitis not fully captured by the model yet and basically found one to two degrees too far north. Most striking for us is the fact that in our model results the temperatures of the modified Atlantic Water transported southward with the East Greenland Current are about one degree too warm compared to observations. This is particularly relevant with respect to glacier-ocean intercation processes, because water that is too warm may cause spuriously high basal melt rates in the 79°N-Glacier cavity.

Nevertheless, the temperature distribution on the continental shelf off Northeast Greenland shows that warm water enters the shelf area through Norske Trough, which is the south-eastern entry to the continental shelf area (Fig. 2). Following the trough system northwards towards 79°N, the modified Atlantic Water slightly cools. Similar pathways can be seen from hydrographic observations (Fig. 2). In addition, sections through Norske Trough capture the core of modified Atlantic Water at about 300 m depth in the observations as well as in the model. Our first model results suggest that warm water of Atlantic origin also enters the shelf through the northeastern entry of the trough system, namely Westwind Trough. Observations show waters of Atlantic orgin that are 1.5°C cooler compared to our model results here. This discrepancy is likely caused by the incorrect location of recirculation enabling warmer water to enter the shelf.

Currently, we work on a more realistic representation of the modified Atlantic Water flow in Fram Strait and onto the continental shelf. Not only the recirculation in Fram Strait but also the flow of warm water across the shelfbreak, which is likely provided by eddies, remain to be major challenges still to be solved.

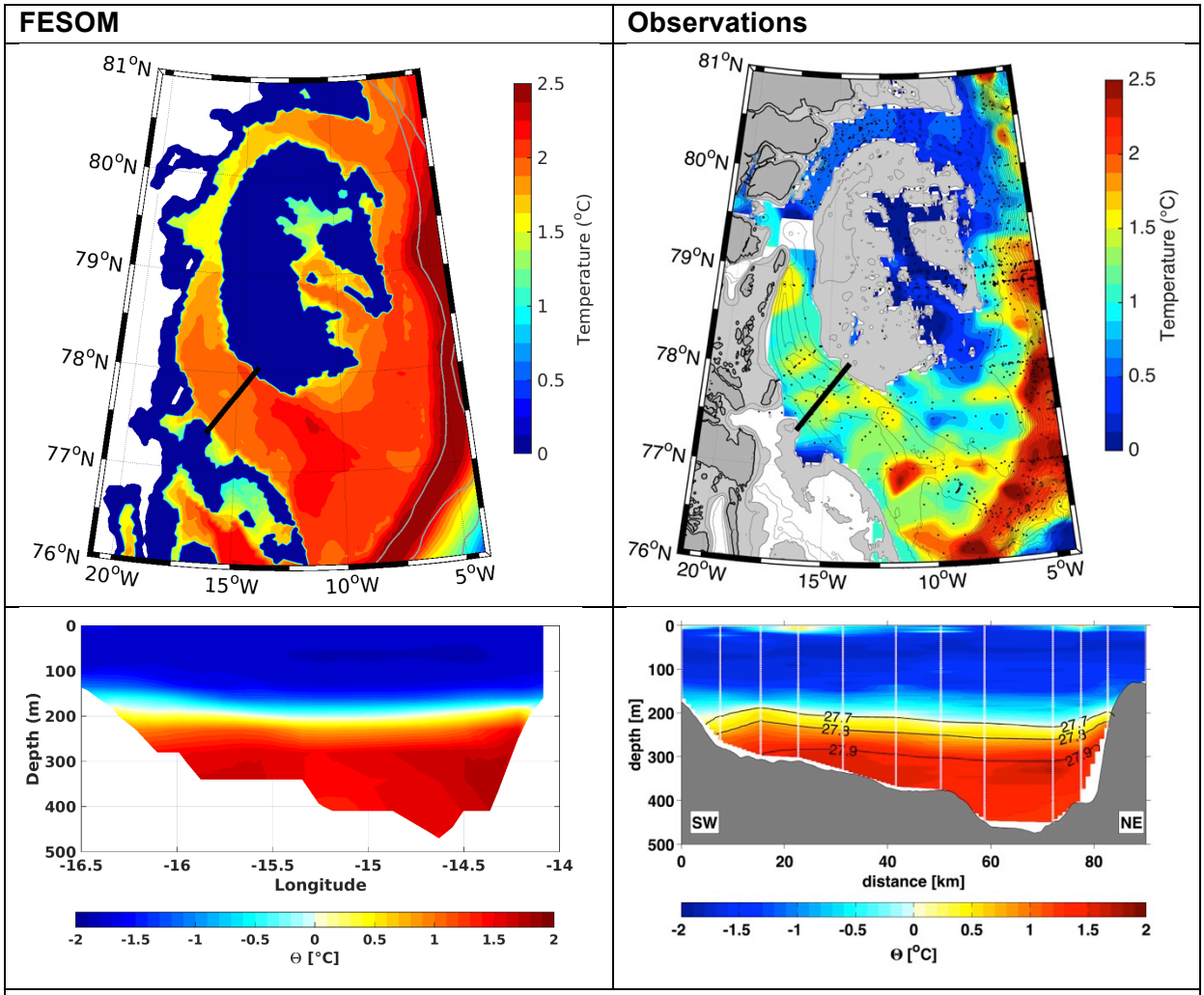

Fig. 2: Summer mean temperature distribution on the continental shelf off Northeast Greenland (top panel) and a temperature section crossing Norske Trough (lower panels). The simulated temperature at 280 m water depth was averaged over 1980-2008 (July-September), dark blue colors indicate depth shallower 280m. The mapped temperature based on observations is a compilation of all available hydrographic data between 1980-2008. The sections are example sections from September across Norske trough (see black line in maps).

Outlook

Future work concentrates on modeling the modified Atlantic Water flow onto the continental shelf and into the 79°N-Glacier cavity in a more realistic way. We aim at developing a locally-high-resolution, hybrid-coordinate configuration into an operational model. Numerical issues inherent to a mesh with a very high stretching factor in a domain with steeply sloping bathymetry and a shallow cavity need to be resolved by adjusting details of the mesh and/or the subgrid-scale parameterizations. Once we have identified a suitablemodel configuration, we plan to run a reference simulation and sensitivity experiments with identical forcing but increased/decreased viscosities and diffusivities, which address the role of eddies, small-scale currents and horizontal mixing in this system. With the high computational burden imposed by the use of a finite-element model, the project depends on resources provided through the HLRN.

References

- Vieli, A., and F. Nick (2011), Understanding and modelling rapid dynamic changes of tidewater outlet glaciers: Issues and implications, *Surv. Geophys.*, *32*, 437–458.
- Beszczynska-Möller, A., E. Fahrbach, U. Schauer, and E. Hansen, Variability in the Atlantic water temperature and transport at the entrance of the Arctic Ocean, 1997-2010 (2012), *ICES Journal of Marine Science*. doi:10.1093/icesjms/fss056.
- Straneo, F. and P. Heimbach (2013), North Atlantic warming and the retreat of Greenland's outlet glaciers, *Nature*, 504(36-43).
- Rignot, E., S. Gogineni, I. Joughin, and W. Krabill (2001), Contribution to the glaciology of northern Greenland from satellite radar interferometry, *J. Geophys. Res.*, *106*(D24), 34,007– 34,019.
- Mayer, C., N. Reeh, F. Jung-Rothenhäusler, P. Huybrechts, and H. Oerter (2000), The subglacial cavity and implied dynamics under Nioghalvfjerdsfjorden Glacier, NE-Greenland, *J. Geophys. Res.*, *27*(15), 2289–2292.
- Budéus, G., and W. Schneider (1995), On the hydrography of the Northeast Water Polynya, *J. Geophys. Res.*, *100*(C3), 4287–4299.
- Danilov, S., G. Kivman, and J. Schröter (2004), A finite-element ocean model: principles and evaluation, *Ocean Model.*, *6*(2), 125–150.
- Danilov, S., Q. Wang, R. Timmermann, N. Iakovlev, D. Sidorenko, M. Kimmritz, T. Jung, and J. Schröter (2015), Finite-element Sea Ice Model (FESIM), version 2, *Geosc. Model Dev.*, *8*, 1747-1761.

Presentations

- J. Schaffer, R. Timmermann, T.Kanzow, J. E. Arndt, C. Mayer, U. Schauer, Pathways of warm water to the Northeast Greenland outletglaciers, European Geosciences Union General Assembly 2015, Wien, Austria, 13 April - 17 April, 2015.
- J. Schaffer, P.Dodd, R. Timmermann, T.Kanzow, J. E. Arndt, C. Mayer, U. Schauer, Pathwaysof warm water to the Northeast Greenland outlet glaciers, ISAR-4 / ICARP III Program, Toyama, Japan, 27 April - 30 April, 2015.
- J. Schaffer, P.Dodd, W. J. von Appen, T.Kanzow, C. Mayer, U. Schauer, Pathways of warm water to the 79°N-Glacier, International Glaciological Society Symposium 2015, Cambridge, United Kingdom, 16 August - 21 August, 2015.

6.12 *hbk00039:* Numerische Untersuchungen zum Mineralstaubkreislauf für quartäre und rezente Klimazustände

HLRN-Projektkennung:	hbk00039
Laufzeit:	III/2014 – III/2015
Projektleiter:	Prof. Dr. Michael Schulz
Projektbearbeiter:	Dr. Ute Merkel
Institut / Einrichtung:	MARUM – Zentrum für Marine Umweltwissenschaften, Universität Bremen
Förderung	Exzellenzcluster/DFG-Forschungszentrum „Der Ozean im System Erde“ (EXC 309 / FZT 15)

Kurzfassung

- Die Rolle von Mineralstaub im Klimasystem ist immer noch mit großen Unsicherheiten behaftet.
- Beobachtungen, z.B. anhand von marinen Sedimentfallen, wie auch geologische Archive deuten auf ausgeprägte Veränderungen im Mineralstaubkreislauf auf der Zeitskala von Jahren bis Jahrtausenden hin.
- Anhand numerischer Klimamodellsimulationen mit einer aktiven Mineralstaubkomponente werden Variabilität und Rückkopplungen im Staubkreislauf auf diesen Zeitskalen untersucht.

Wissenschaftlicher Hintergrund und Ergebnisse

Mineralstaub gilt als eine Schlüsselgrösse im Klimasystem und kann als Antriebsfaktor für Klimaschwankungen fungieren, aber auch selbst auf Störungen im Klimasystem reagieren (z.B. Merkel et al., 2014). Man geht heute davon aus, dass Staub nicht nur die atmosphärische Strahlungsbilanz und Wolkenmikrophysik beeinflusst, sondern auch Auswirkungen auf Meeresoberflächentemperaturen und die Ozeanbiogeochemie haben kann. Ferner umfassen staubrelevante Prozesse einen großen Zeitskalenbereich - von meso-bis-synoptischskaligen Windfluktuationen, die für den Eintrag von Staub in die Atmosphäre sorgen, bis hin zu Eiszeit-Warmzeit-Zyklen, bei denen Staub in Wechselwirkung mit den Schwankungen der kontinentalen Eisschilde treten kann.

Geologische Archive wie Eisbohrkerne und Meeresedimente für das Quartär, aber auch zahlreiche von MARUM-Wissenschaftlern am HLRN durchgeführte Modellsimulationen legen zudem deutliche Änderungen auf Zeitskalen von Jahrhunderten bis Jahrtausenden im hydrologischen Kreislauf (Mohtadi et al., 2014), in Klimamoden (Felis et al., 2012) und Fernwirkungsmustern (Merkel et al., 2010) sowie deutliche Umstellungen der atlantischen Umwälzzirkulation nahe (Kageyama et al., 2013; Ronge et al., 2015; Zhang et al., 2014; Zhang et al., 2015). Hierbei ist von Interesse, inwieweit damit auch Veränderungen des Mineralstaubkreislaufs einhergegangen sein könnten.

Sowohl aus heutiger wie auch geologischer Perspektive benötigt man daher ein genaueres Verständnis wichtiger Prozesse im Staubkreislauf (z.B. Friese et al., 2015), insbesondere auch der Deposition von Staub über den Ozeanen, der Prozesse von Partikeln auf dem Weg durch die Wassersäule und letztlich der Sedimentation, die beispielsweise von Sedimentfallen aufgezeichnet werden kann. Inzwischen existieren erste längere Datensätze von Sedimentfallen (Fischer et al., 2015), welche es erlauben, auch zwischenjährliche Variationen des Staubeintrags in den Ozean zu untersuchen und letztlich die Interpretation der in marinen Sedimentkernen aufgezeichneten Signale zu Variationen des Staubkreislaufs zu verbessern. Es ist somit erforderlich, sowohl das heutige Klima wie auch die Klimazustände des Quartärs im Hinblick darauf genauer zu untersuchen, wie Klimafluktuationen den Mineralstaubkreislauf beeinflussen und welche Rückkopplungen dabei eine Rolle spielen. Hierzu führen wir numerische Modellstudien für das heutige Klima und verschiedene Klimazustände des Quartärs durch und verwenden dafür das komplexe Klimamodell CCSM3, welches Komponenten für die Atmosphäre, die Landoberfläche, und den Ozean einschliesslich Meereis und in erweiterter Form eine aktive Staubkomponente umfasst.

Das CCSM3-Modell ist in Fortran 90 formuliert und stellt technisch gesehen ein MPMD-Modell ('Multiple-Program-Multiple-Data') dar. Es ist somit für Hybrid-Parallelisierung unter Verwendung von MPI und OpenMP konzipiert. Das Modell wurde zusammen mit seiner aktiven Staubkomponente erfolgreich am HLRN-3 implementiert. Es arbeitet mit vier verschiedenen Größenklassen (im Bereich 0.1-10 µm) für Staubpartikel, die entsprechend der atmosphärischen Zirkulation verfrachtet und deponiert werden.

Aus einem CCSM3-Kontrolllauf mit heutigen Randbedingungen und aktiver Staubkreislaufkomponente wurde die globale Staubdeposition, die sich aus trockener und nasser Deposition zusammensetzt, bestimmt und durch lineare Korrelation mit Klimaphänomenen wie ENSO (El Niño/Southern Oscillation) und der NAO (Nordatlantik-Oszillation) in Bezug gesetzt (Abb. 1).

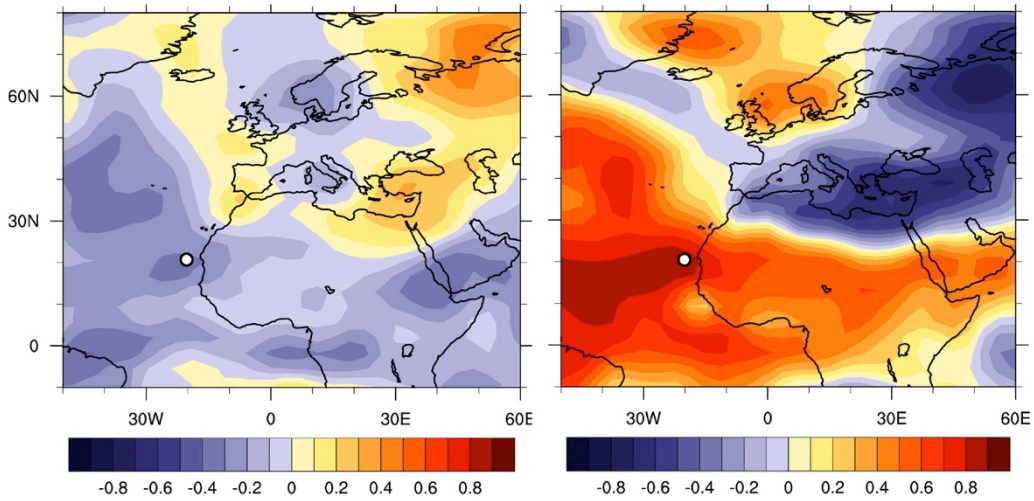

Abb. 1: Korrelation der simulierten Staubdeposition (Summe aus trockener und nasser Deposition)an jedem Modellgitterpunkt mit dem Niño3-Gebietsmittel (150°W-90°W, 5°S-5°N) für Meeres-oberflächentemperaturanomalien im tropischen Pazifik (linke Abb.) und dem Luftdruckindex der Nordatlantischen Oszillation (rechte Abb.). Gezeigt sind Werte für die nordhemisphärische Wintersaison (Dez.-Feb.) aus einem CCSM3-Kontrolllauf mit aktivem Staubmodul und mit heutigen klimatischen Randbedingungen. Die Sedimentfallenlokation vor der westafrikanischen Küste (Cap Blanc) ist mit einem weißen Punkt gekennzeichnet.

Aus der Auftriebsregion vor Cap Blanc (Westafrika) liegen für die vergangenen rund 20 Jahre Daten aus Sedimentfallen vor, u.a. zum Eintrag von lithogenem Material, welcher ausgeprägte zwischenjährliche Variationen aufweist (Fischer et al., 2015). Die mit dem Modell gewonnenen Muster verdeutlichen, dass verschiedene Phasen der ausgewählten Klimamoden unterschiedlich auf die Windverhältnisse (nicht gezeigt) und die Staubdeposition in der Fallenregion und somit auf die in den Fallen registrierten Materialeinträge wirken können. Während ein El-Niño-Ereignis im tropischen Pazifik zu reduzierter Staubdeposition vor Westafrika führt (Abb. 1 links), geht eine positive NAO-Phase mit verstärkter Staubdeposition vor Westafrika einher (Abb. 1 rechts). Zugleich verdeutlichen die Muster, dass es bei gleichzeitig auftretenden gegenläufigen ENSO- und NAO-Phasen (z.B. El-Niño-Ereignis während einer negativen NAO-Phase) in der Überlagerung nur zu einem eher schwachen Signal in den Fallenaufzeichnungen kommen könnte, was von Bedeutung für die Interpretation der Sedimentfallendaten ist. Längere Fallenzeitreihen sind hier erforderlich, um die Robustheit rein linearer Zusammenhänge und die vom Modell simulierte (multi-)dekadische Variabilität (nicht gezeigt) zu testen.

Kooperationen

Dr. Jan-Berend Stuut, NIOZ, Texel, Niederlande; Arbeitsgruppe Prof. Dr. John Burrows, Institut für Umweltphysik, Universität Bremen; Arbeitsgruppe Prof. Dr. Natalie Mahowald, Cornell University, Ithaca, NY, USA

Vorträge/Poster

1. Posterpräsentation “Mineral dust in present and past climates – simulations with a comprehensive climate model”, 2. Leipziger Staubtag, Leibniz-Institut für Troposphärenforschung (TROPOS), Leipzig, 7. Juli 2015 (U. Merkel)

Publikationen

1. Felis, T., **U. Merkel**, R. Asami, P. Deschamps, E. C. Hathorne, M. Kölling, E. Bard, G. Cabioch, N. Durand, M. Prange, **M. Schulz**, S. Y. Cahyarini, M. Pfeiffer, *Pronounced interannual variability in tropical South Pacific temperatures during Heinrich Stadial 1,* Nature Communications, *3:965, doi:10.1038/ncomms1973 (2012)*
2. Fischer, G., O. Romero, **U. Merkel**, B. Donner, M. Iversen, N. Nowald, V. Ratmeyer, G. Ruhland, M. Klann, G. Wefer, *Deep ocean mass fluxes in the coastal upwelling off Mauritania from 1988 to 2012: variability on seasonal to decadal timescales,* Biogeosciences Disc., *12, 17643-17692 (2015, in revision)*
3. Friese, C., M. van der Does, **U. Merkel,** M. Iversen, G. Fischer, J.-B. Stuut, *Environmental factors controlling the seasonal variability in particle size of modern Saharan dust deposited off Cape Blanc,* Aeolian Research *(2015, in revision)*
4. Kageyama, M., **U. Merkel**, B. Otto-Bliesner, M. Prange, A. Abe-Ouchi, G. Lohmann, R. Ohgaito, D. M. Roche, J. Singarayer, D. Swingedouw, X. Zhang, *Climate impacts of freshwater hosing under Last Glacial Maximum conditions: a multi-model study,* Clim. Past, *9, 935-953, doi:10.5194/cp-9-935-2013 (2013)*
5. **Merkel, U.**, D.-D. Rousseau, J.-B. W. Stuut, G. Winckler, L. von Gunten, T. Kiefer (Hrsg.): Dust – Special issue of Past Global Changes Magazine, *22 (2014)*
6. **Merkel, U.**, M. Prange, M. Schulz, *ENSO variability and teleconnections during glacial climates*, Quat. Sci. Rev., *29, 86-100(2010)*

7. Mohtadi, M., M. Prange, D. W. Oppo, R. De Pol-Holz, **U. Merkel**, X. Zhang, S. Steinke, A. Lückge, *North Atlantic forcing of tropical Indian Ocean climate,* Nature, *509, 76-80, doi:10.1038/nature13196 (2014)*
8. Ronge, T., S. Steph, R. Tiedemann, M. Prange, **U. Merkel**, D. Nürnberg, G. Kuhn, *Pushing the boundaries: Glacial/interglacial variability of intermediate and deep waters in the southwest Pacific over the last 350,000 years,* Paleoceanography, *30, 23-38, doi:10.1002/2014PA002727 (2015)*
9. Zhang, X., M. Prange, **U. Merkel**, **M. Schulz**, *Spatial fingerprint and magnitude of changes in the Atlantic meridional overturning circulation during marine isotope stage 3,* Geophys. Res. Lett., *42, 1903-1911, doi:10.1002/2014GL063003 (2015)*
10. Zhang, X., M. Prange, **U. Merkel, M. Schulz**, *Instability of the Atlantic overturning circulation during Marine Isotope Stage 3,* Geophys. Res. Lett., *41, 4285-4293, doi:10.1002/2014GL060321 (2014)*

6.13 *hbk00040:* Agulhas. Regional and Global Relevance

HLRNProject ID:	hbk00040
Run time:	II/2014 – II/2016
Project Leader:	Prof. Dr. Thomas Jung
Project Scientists:	Dmitry Sein, Qiang Wang
Affiliation:	Alfred Wegener Institute for Polar and Marine Research

Overview

The Agulhas Current system, comprising of various components, is of relevance for global and regional climate on all timescales. Work undertaken in this area over the last few years have highlighted that this region is sensitive to changes of the global overturning circulation. In particular, an increase in the amount of the Indian Ocean waters entering the Atlantic has been attributed to the changes in the wind pattern in the Southern Hemisphere. Such intrusion of additional heat and salt into the Atlantic may potentially impact the stability of the meridional overturning circulation and the heat transport into the North Atlantic.

Despite this local and global importance, the dynamics of the Agulhas system is not yet fully understood and, owing to the strong nonlinear interactions and temporal variability, is far from being properly quantified. The notorious under sampling of the oceans around South Africa calls for dedicated studies within ocean general circulation models and emphasizes the importance of a reasonable representation of the current system in both modern and future coupled climate models.

This project aims to improve the understanding of the Agulhas dynamics, its embedment within the global oceanic circulation, and its impact on regional and global climates. Utilized is a state-of-the-art ocean general circulation model, i.e. Finite Element Sea-Ice Ocean Model FESOM (Wang et al., 2008). The latter will serve as a blueprint for testing the numerical representation of this complicated oceanic region in the next generation of ocean and climate models. The model simulations will give robust hindcast runs of the past 60 years as well as predictive runs under future climate conditions.

Results

Due to its conceptual numerical advancements the Finite Element Sea ice Ocean Model (FESOM) developed at AWI represents the next generation of ocean models for ocean and climate modelling studies to be used within the coming years.

FESOM has matured and is currently applied to a growing set of oceanographic problems. The Agulhas region and its place within the global circulation is a well-suited and demanding test-bed for the applicability of FESOM in the global climate community due to the wide range of horizontal and temporal scales involved. The combined requirement of high temporal and spatial resolution for distinct (but not too limited) key regions (Mozambique Channel, Agulhas Current, and Agulhas ring corridor) and the global impact on longer timescales makes the Agulhas region a well-suited and demanding test-bed for FESOM. With FESOM, different grid resolution can be conveniently assigned to different local regions in a global setup.

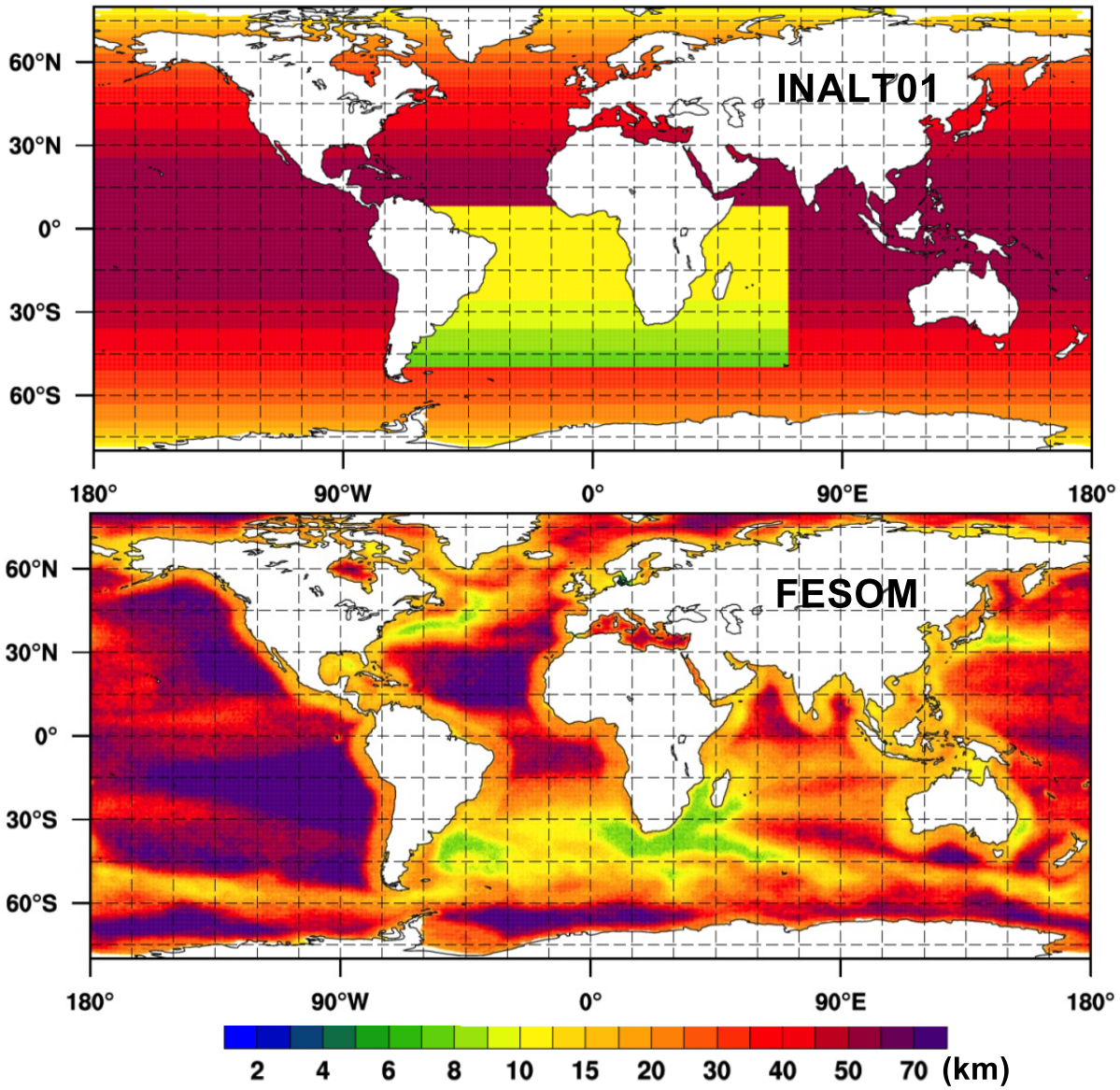

Figure 1: INALT01 (upper) and FESOM (lower) grid resolution

The use of the unstructured-mesh allows for variable grid resolution without traditional nesting. With FESOM, different grid resolution can be conveniently assigned to different local regions in a global setup. In practical applications with limited computational resources, we keep the horizontal mesh resolution relatively coarse (50-75km) in most parts of the global ocean (Fig.1), and refine (down to 4-8km) particularly chosen regions. *According to the aims of our study the grid refinement depends on observed mean sea surface height (SSH) variance. Physically it means the larger is SSH variance, the more active are ocean eddies, the higher FESOM grid resolution required.* Thus, additionally to Agulhas region we increased the model resolution along the pathways of important ocean currents, e.g. Gulf Stream, Antarctic Circumpolar Current (ACC), Kuroshio, etc. Totally the model setup has ca. 800000 horizontal nodes and 47 z-coordinate vertical levels. Having eddy permitting resolution in all the “important” regions it has very high computational performance, simulating 7-8 years per day.

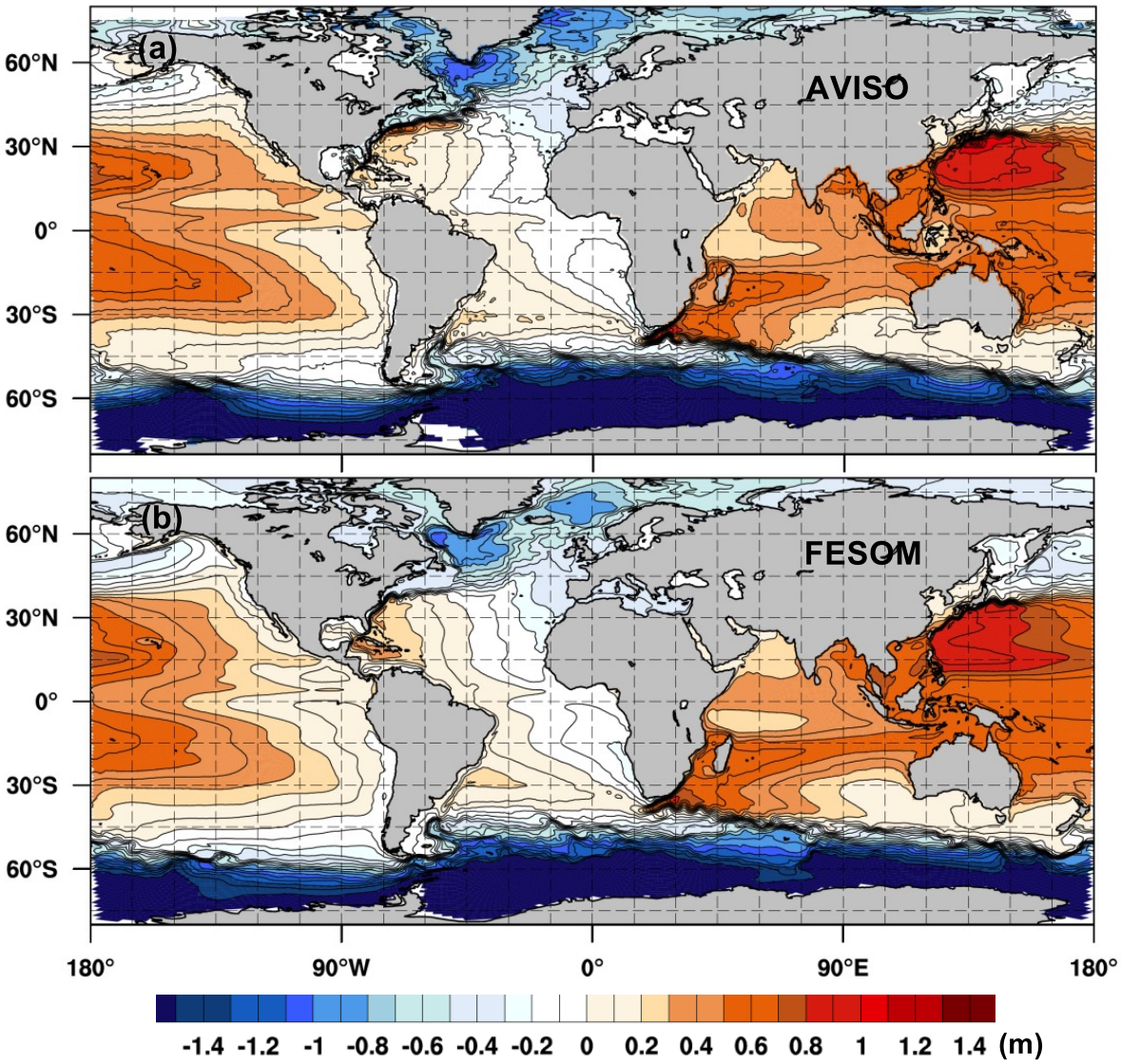

Figure 2: Observed (AVISO) and modelled (FESOM) mean 1988-2007 SSH (m)

INALT01 is a nested configuration of NEMO (Durgadoo et al 2012). It consists of a global base model at 1/2º resolution within which a 1/10º nest of the South Atlantic and western Indian Oceans is hosted (Fig 1). The model successfully simulates the intricacies of the greater Agulhas Current system. Therefore, for estimating the ability of the FESOM to represent the ocean circulation, we provide the inter-comparison between INALT01 and FESOM simulation results.

After 120 years spin-up both the models were ran for the 1948-2009 period forced with CORE 2 forcing.

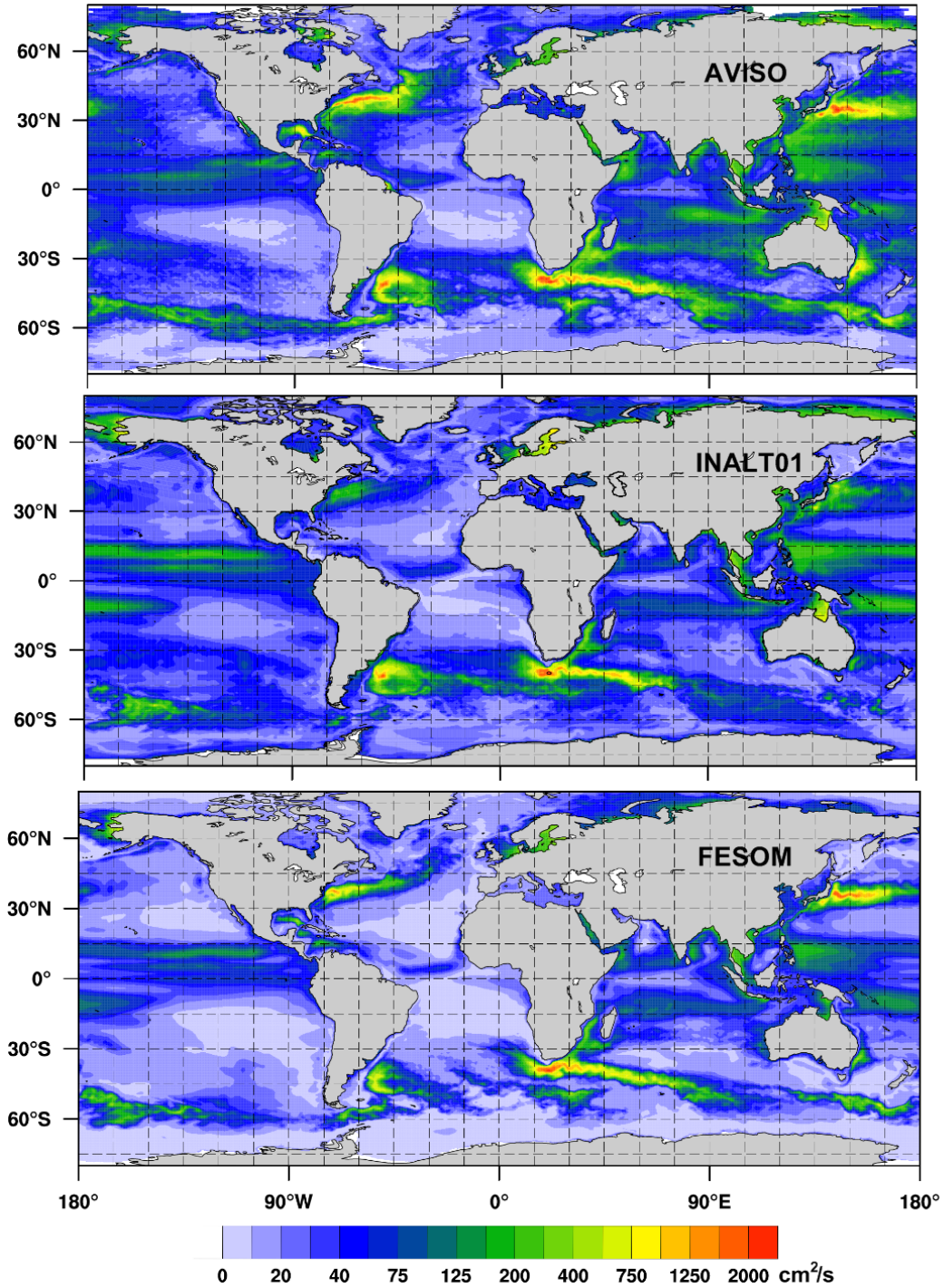

Figure 3: SSH variance calculated from 5 daily mean output. Observations (AVISO), INALT01 and FESOM

Simulated SSH and its variance were compared against AVISO data (http://www.aviso.altimetry.fr). Fig. 2 shows reasonable agreement of simulated SSH with observations. Comparing simulated and observed mean SSH variance (based on 5 daily means) we can conclude that the eddy activity simulated by FESOM reasonably agree with observations not only in the Agulhas region, but also in the regions of Gulf Stream and Kuroshio. From the other hand FESOM underestimates SSH variance in the South-East Pacific and Tropical Atlantic, i.e. in the regions where its resolution exceeds 70 km.

Comparing the cross-section velocities of the Agulhas current (Fig.5) we conclude that INALT01 and FESOM show very similar dynamics in the region.

In general the two models show very similar results. But the flexibility of FESOM to use different spatial resolution makes it a quite powerful tool in the global ocean modeling

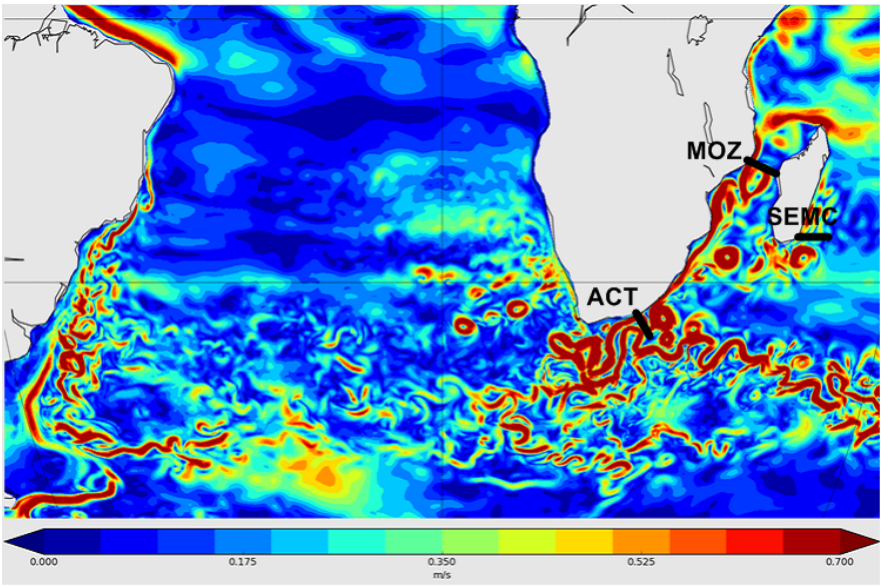

Figure 4: 50 m velocity snapshot, simulated by FESOM. MOZ, ACT and SEMC are cross-sections displayed on Fig. 5.

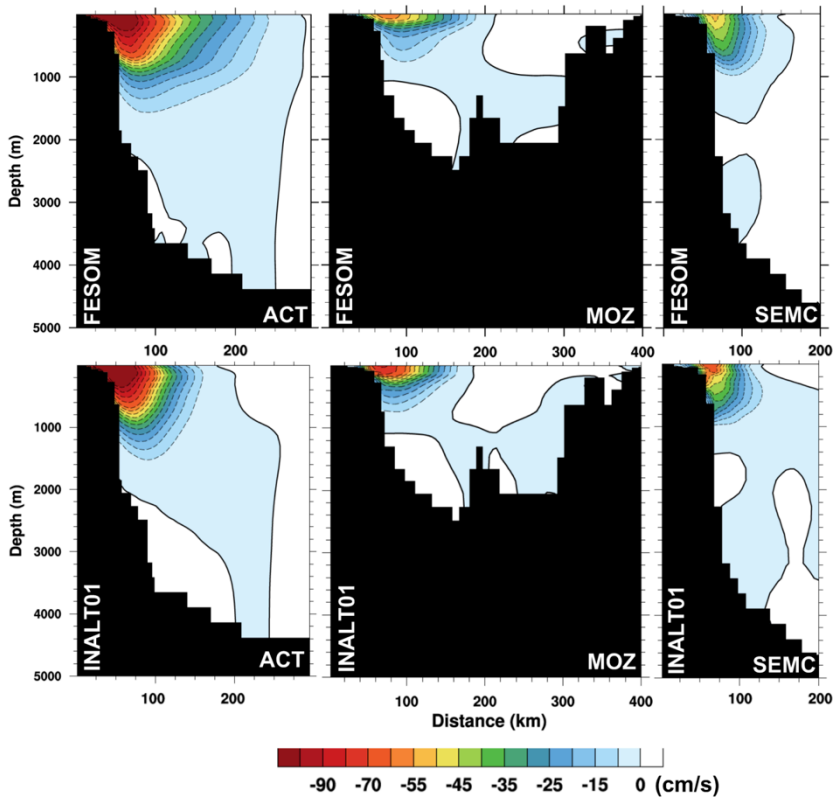

Figure 5: Mean cross-section (see Fig. 4) velocities

Outlook

After the successful model validation we plan to simulate two climate change scenarios. For this purpose we need to run FESOM with the atmospheric forcing obtained from the global climate model. For the correct estimate of the possible future changes in the ocean climate we need to make historical simulation (1911-2005) using the atmospheric forcing calculated by the same climate model which will be used to force the consequent climate change simulations.

Publications

1. Sein, D.V., Danilov, S., Biastoch, A., Durgadoo, J.V., Sidorenko, D., Harig, S., Wang, Q., 2016. Designing variable ocean model resolution based on the observed ocean variability. JAMES, accepted.
2. Wang, Q., Danilov, S., Sidorenko, D., Timmermann, R., Wekerle, C., Wang, X., Jung, T., Schröter, J., 2014. The Finite Element Sea Ice-Ocean Model (FESOM) v.1.4: formulation of an ocean general circulation model. Geosci. Model Dev. 7, 663–693. doi:10.5194/gmd-7-663-2014

6.14 *hbk00042:* Climatic evolution in the marginal seas of the Northwest Pacific Ocean since the last glacial period until present day: changes in the formation of North Pacific Intermediate Water formation and their implications on the Pacific realm

HLRN Project ID:	hbk00042
Run time:	I/2015 – III/2017
Project Leader:	Prof. G. Lohmann
Project Scientists:	Dr. P. Scholz, Dr. X. Gong
Affiliation:	Alfred Wegener Institute Helmholtz Center for Polar and Marine Research

Overview

The aim of this project is to simulate the variability of the sea ice cover, general ocean circulation and hydrology of the marginal seas in the Northwest Pacific Ocean as well as the Arctic Ocean on different time-slices since the last glacial period up to present day (e.g. last glacial maximum (LGM, 21000 years ago), mid (6000 years ago) Holocene, pre-industrial as well as present day).

A particular focus will be on the Sea of Okhotsk, which has nowadays a significant role in the climate system of the Northwest Pacific by influencing the atmospheric and oceanic circulation as well as the hydrology of the Pacific water masses. In the Sea of Okhotsk, the so called Sea of Okhotsk Intermediate Water (SOIW) is formed, which in turn contributes to the vertical ventilation in the North Pacific and to the mid-depth water masses of the North Pacific Intermediate Water (NPIW). NPIW is one of the key elements for the nutrient and oxygen supply of the low latitude Pacific Ocean realm.

As such the main question of this project is: How the role of the Sea of Okhotsk and the other marginal Seas (e.g. Bering Sea) as a source for NPIW has changed during the different climatological time-slices since the last glacial period? Beyond the regional focus on the marginal seas of the Northwest Pacific, this project should also clarify what are the large scale implications and teleconnections of the changes in NPIW.

To find a compromise between a global coverage and a regional highly increased resolution, which is necessary to adequately reproduce the deep and intermediate water formation, at relatively moderate computational costs, we will use in this project the Finite-Element Sea-Ice Ocean Model (FESOM).

Model Setup

To fulfill the project target of simulating a reliable intermediate water formation in the Sea of Okhotsk, a customized FESOM model setup (Fig. 1) for the present-day, pre-industrial and mid Holocene time-slice was created. This setup features a homogenous resolution of 17.5 km North of 50°N and 25 km South of -60°S as well as a homogenous resolution of 30 km in an equatorial belt with a width of 15°. The coastal resolution is in the order of around 0.4°, whereas the bulk resolution of the setup has a value of ~1°. The marginal Seas of the Northwest Pacific (e.g. the Yellow Sea, the Sea of Japan, the Sea of Okhotsk and the Bering

Sea) feature a homogeneous resolution of 6-8 km. This setup consists of ~550000 2d surface nodes. For the vertical discretization we use 61 vertical levels which have a stepwise increasing vertical resolution from 10 m to maximum of 150 m after a depth of 1450 m. The entire FESOM model setup has a size of ~15 x 10^6 3d node points.

The model setup runs stable at a time step of 15 minutes, which allows us to perform several long term simulations with periods of 300 to 500 years in a time span that is in the scope of our current BMBF project framework.

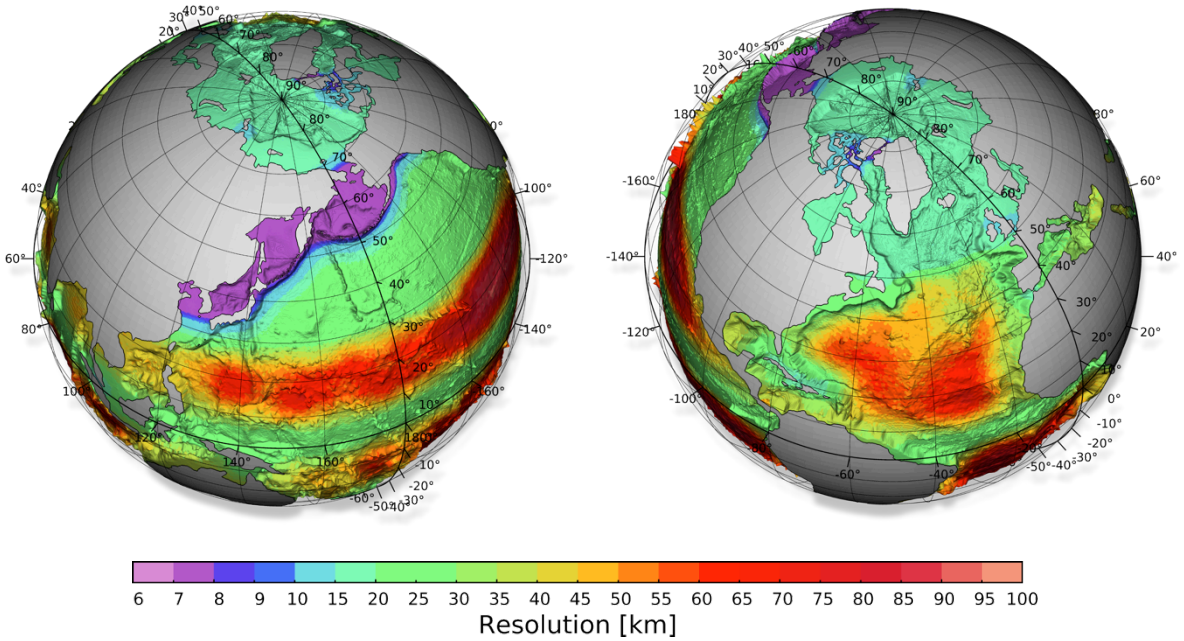

Fig 1: Approximated mesh resolution of the new customized global FESOM configuration, with a regional focus on the marginal Seas of the Northwest Pacific Ocean (e.g. Yellow Sea, Sea of Japan, Sea of Okhotsk and Bering Sea) and Northern Hemispheric deep water formation areas. The new setup has a minimum resolution of ~6 - 8 km in the Sea of Okhotsk, Sea of Japan and Bering Sea.

Results

In 2015 we finished the first simulations of the present day time-slice using the above mentioned FESOM model setup forced by the COREv2 Air-Sea Flux Dataset [1] for the period 1948 until 2009. As spinup strategy we choose to split the process in several spinup cycles: in the first cycle the model is initialized with the hydrography of the WOA 2001 and subsequently driven by the COREv2 data for the period 1948-2009 and the second spinup cycle is initialized with the last output year of the previous cycle and so on. Based on previous results with smaller mesh configurations, this spinup strategy gives a reliable ocean state which is also well comparable to observational derived data after 250 years of spinup.

We managed to simulate five present-day spinup cycles over the COREv2 period, which corresponds to 310 simulated model years. We evaluate the progress of the spinup at the example of the Atlantic Meridional Overturning Circulation (AMOC) and the Indo-Pacific Meridional Overturning Circulation (PMOC) streamfunction, where positive and negative values indicate clockwise and counter clockwise circulation. Fig. 2a shows the mean AMOC state for the period 1948-2009 for all five cycles. It is shown that the strength of the upper AMOC cell decreases, while the strength of the lower AMOC cell increases during the spinup

process. From the fourth to the fifth spinup cycle there are almost no changes anymore in the strength and structure of the upper and lower AMOC cell.

In Fig. 2b the evolution of the mean PMOC state for the period 1948-2009 through all five spinup cycles is presented. The strength of the lower PMOC cell, which refers to the Circumpolar Deep Water (CDW), decreases from the first to the fifth spinup whereas the strength of the equatorial upwelling increases slightly. Also here can be seen that from the fourth to the fifth spinup cycle a sufficient quasi equilibrium state in terms of the strength and structure of the PMOC at least for the upper and intermediate ocean is reached. Only for the very deep pacific below 5000 m there are still some minor adaption in the strength of the PMOC during the fifth spinup cycle.

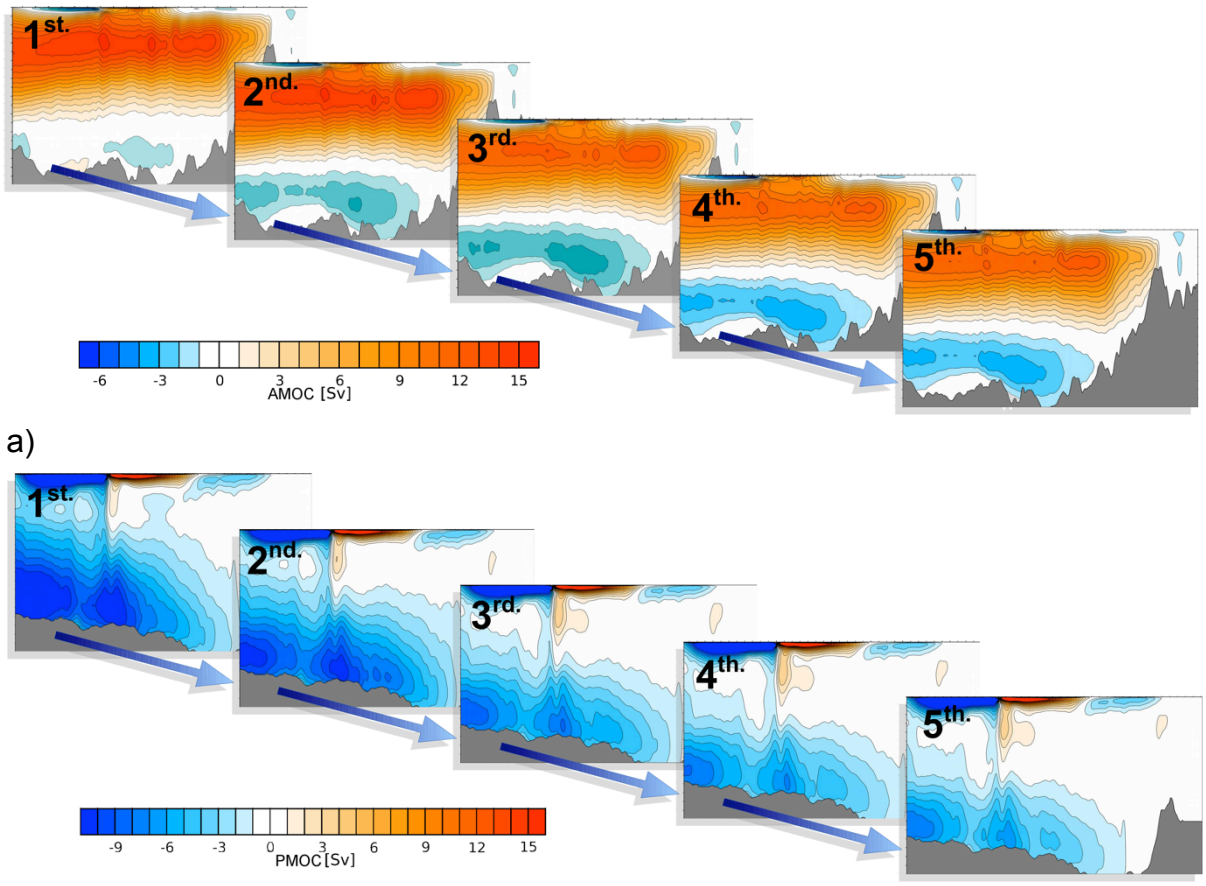

Fig. 2: Evolution of the Atlantic Meridional Overturning Circulation (AMOC) (a) and Indo-Pacific Meridional Overturning Circulation (PMOC) (b) throughout the five applied spinup cycles under COREv2 forcing.

To evaluate the reliability of the last COREv2 forced spinup cycle for the Northwest Pacific, we applied an initial model data comparison for the Sea of Okhotsk. Therefore we defined an index area (144°E<=lon<=148°E, 44°N<=lat<=48°S) in the southwestern Sea of Okhotsk and calculated the modeled (Fig. 3a,b) summer (JJA) seasonal temperature and salinity over depth and time for the period 1963 until 1991. These indices are compared with similar

indices based on observational World Ocean Database 2013 data (Fig. 3c,d) calculated over the same region. Here, we limit our analysis to the summer season, because only for this season we have enough observations to calculate a trustworthy seasonal mean.

The comparison shows a tremendous deviation between the modeled and observed temperature and salinity over depth and time in the southern Sea of Okhotsk, especially in depths below 200 m. There, the modeled temperature features a constant warming over the entire considered period of around 1.5°C to 2.0°C compared to the observed temperature. Also the modeled salinity shows to high values in depth below 200 m when compared to the observed salinity. Especially the high modelled salinity in the intermediate layers leads to an increased density which suppresses the vertical ventilation of a cold surface water layer. We could trace back this warm and salty water mass in the model throughout the entire northern branch of the Subpolar Pacific Gyre and found its origin in the delocation of the Kuroshio Current and North Pacific Current in the model. It is revealed that the position of the Kuroshio Current is shifted by around 2° to 4° degree to the north when compared to reality but also the strength of the Kuroshio Current is overestimated in the model by ~3 to 4 Sv. Due to this, too much warm and salty waters from the Subtropical Pacific Gyre reaches to the north and enters the branch of the Subpolar Pacific Gyre which causes at its end an intrusion of warm and salty waters in the intermediate layers of the Sea of Okhotsk and thus suppresses in the model the formation of SOIW.

Due to the deficiencies of the COREv2 forcing in reproducing a reliable stratification in the marginal seas of the Northwest Pacific Ocean and an extensive testing of the COREv2

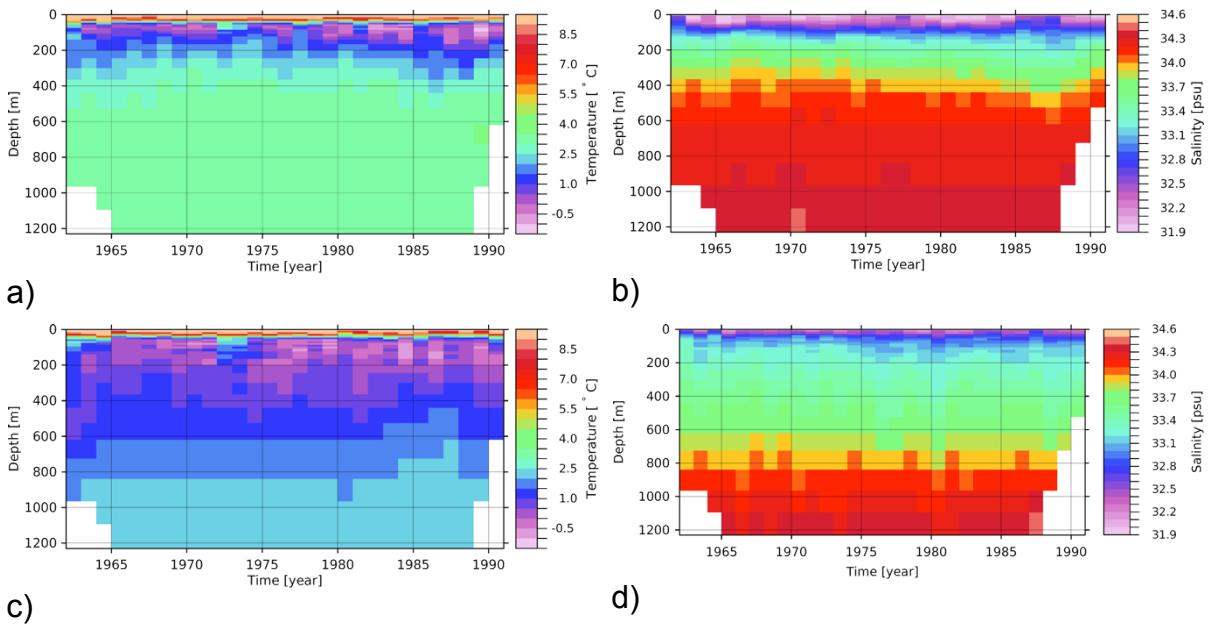

Fig. 3: Modeled seasonal June, July and August (JJA) averaged temperature (a) and salinity (b) over depth and time for a box in the southwestern Sea of Okhotsk for the last spinup cycle forced with COREv2 data. (c) and (d) from observational derived World Ocean Database 2013 JJA temperature (c) and salinity (d) over depth and time for the same area.

forcing data by comparing to other reanalysis products, we decided to try towards the end of 2015 an alternatively atmospheric forcing. Therefore we adapted the FESOM model code to use the combined ECMWF ERA 40 and ERA interim reanalysis data set, which covers the period 1958 to 2015, as atmospheric forcing. This forcing data set has the advantage that it provides a higher spacial and temporal resolution compared with COREv2 and the ERA interim data set is updated on a regular basis.

As such in a next step we want to perform several sensitivity simulations using the ERA 40/interim reanalysis data set as atmospheric forcing to test if the new forcing brings an improvement to the vertical stratification in the marginal seas of the Northwest Pacific Ocean. Further changes into the FESOM code might be necessary to adapt the model to the new forcing.

6.15 *hbk00044:* Exploring pathways of Atlantic Water into the Arctic Ocean: high resolution ocean-sea ice and biogeochemical simulations

HLRN Project ID:	hbk00044
Run time:	IV/2015 – III/2016
Project Leader:	Prof. Dr. Thomas Jung[1,2]
Project Scientists:	Dr. Claudia Wekerle[2], Dr. Vibe Schourup-Kristensen[2], Dr. Qiang Wang[2], Dr. Sergey Danilov[2], Prof. Torsten Kanzow[1,2]
Affiliation:	[1]University of Bremen, [2]Alfred Wegener Institute

Abstract

Warm, salty and nutrient-rich Atlantic Water is transported within the Norwegian Atlantic Current through the Nordic Seas into the Arctic Ocean. It enters the Arctic Ocean through the deep and wide Fram Strait, and through the shallow Barents Sea. This water contributes significantly to the heat budget and brings in the nutrients necessary for phytoplankton growth. Resolving its complex circulation structure and eddies responsible for AW lateral spreading presents a numerical challenge and requires considering scales as small as 5 km or finer. Hindcast experiments with a global configuration of the Finite Element Sea-ice Ocean Model (FESOM), with highly resolved Nordic Seas and Arctic Ocean (4.5 km), show substantial improvement of the realism of the simulated circulation as compared to simulations on a coarse (24 km) mesh. The model effectively scales to a large number of cores and provides a high throughput of about 5 model years per simulation day.

Due to the tight bio-physical coupling in the Arctic Ocean, the biological results from coupled ocean-biogeochemical models rely heavily on the state of the ocean circulation and mixing. We use the current high-resolution version of FESOM coupled to the biogeochemical model REcoM2 to gain a better understanding of the role of improved representation of ocean dynamics for the nutrient supply to the Arctic Ocean. This helps us understand the relative importance of nutrient supply and light limitation for biological production in the area, the question that is currently still open in ocean-biogeochemical models due to relatively large biases in the ocean components.

Methods

In this project we apply a global configuration of the ocean-sea ice model FESOM (e.g. Wang et al. 2014, Danilov et al., 2015). It uses unstructured triangular meshes in the horizontal, allowing for refinement in areas of interest. Our current model configuration has 1° nominal horizontal resolution in the bulk of the global ocean and 24 km in the North Atlantic. Along the coastlines, resolution is doubled. In the Arctic Ocean and Nordic Seas, the resolution is 4.5 km (mesh HIGH, Figure 1). The model is integrated from 1949 until 2009, using COREv2 atmospheric forcing (simulation HIGH). To investigate the impact of mesh resolution, a control run was performed with 24 km resolution in the Nordic Seas and Arctic Ocean (simulation CONTROL). It should be noted that FESOM is well suited for the Arctic

region given the special geometry (a large fraction of land and shelves), in contrast to structured-mesh ocean models where many grid points are covering land.

FESOM has recently been coupled to the biogeochemical model REcoM2 (Schourup-Kristensen et al. 2014), and this coupled modeling system has proved to be well suited for studies on the global scale. In this project, we run FESOM-REcoM2 on the Arctic high-resolution grid to focus on the physical controls of biology in the Nordic Seas and the Arctic Ocean.

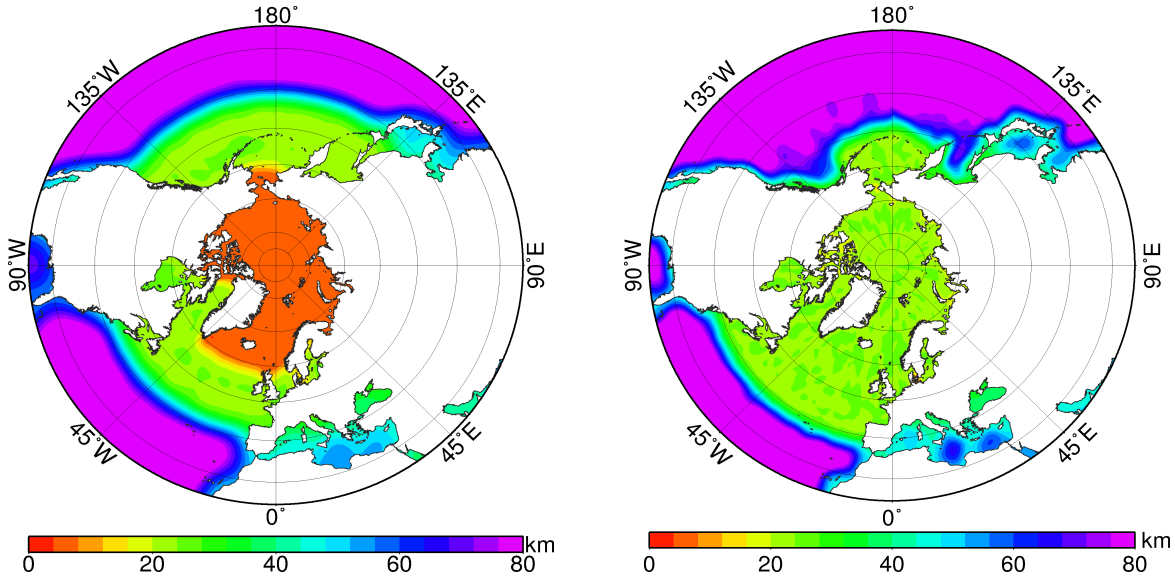

Fig. 1: Resolution in km of the global meshes used in this study: mesh HIGH (left) is highly resolved with up to 4.5 km in the Arctic Ocean and Nordic Seas (left), whereas mesh CONTROL (right) has a resolution of 24 km in the Arctic Ocean and Nordic Seas. In HIGH, 80% of all surface nodes are concentrated in areas of high mesh resolution.

Results

1. Transport of Atlantic Water through Fram Strait

Fram Strait is the only deep connection (~2500 m) between the Nordic Seas and the Arctic Ocean, and the only gate where warm Atlantic Waters enter the Arctic Ocean directly. In particular, cold and fresh polar waters and sea ice are transported southwards within the East Greenland Current on the western side of Fram Strait, while warm and salty Atlantic Water is found on its eastern side, traveling within the West Spitzbergen Current (WSC) northwards. Since 1997, the Alfred Wegener Institute and the Norwegian Polar Institute maintain an array of deep oceanographic moorings at 78° 50' N (Beszczynska-Möller et al., 2012).

Time series of Atlantic Water volume transport in the WSC computed from observations (Beszczynska-Möller et al., 2012) and model results are shown in Figure 2. Evidently, there is a good correlation between observed Atlantic Water volume transport with the one obtained by simulation HIGH (r=0.57, based on monthly means); a considerably lower correlation is found for simulation CONTROL (r=0.29). Simulation HIGH also shows an improvement regarding mean transports, as the magnitude of transports in the control run is too low. To conclude, the Atlantic Water transport in Fram Strait is one example of the improvements brought by higher mesh resolution.

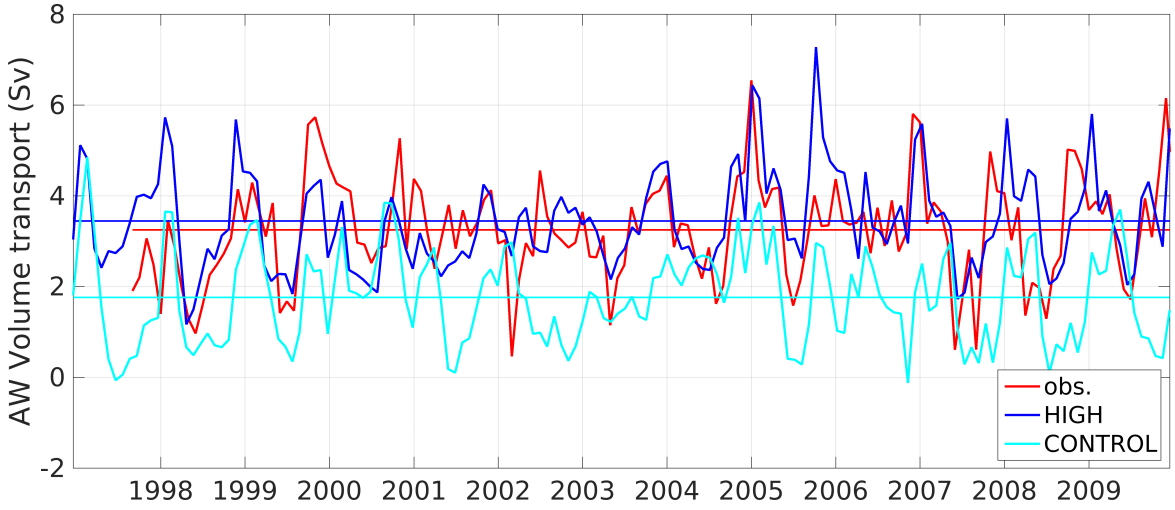

Fig. 2: Time series of monthly mean net Atlantic Water volume transport in Sv (1 Sv=10^6 m^3/s) in the eastern Fram Strait (east of 5°E) from observations (Beszczynska-Möller et al., 2012, red line) and simulations HIGH (blue line) and CONTROL (cyan line). Atlantic Water is defined by a temperature criterion (T>2°C).

2. Biogeochemical model

The biogeochemical model REcoM2 coupled to the ocean general circulation model FESOM is now running on the high resolution Arctic grid prepared by Wekerle et al. (in prep.). To prepare this setup, riverine and aeolian input of nutrients has been added to the code along with sedimentary nutrient removal. The high resolution of the grid in combination with the 21 tracers added by the biogeochemical model made it necessary to reconfigure the saving routines as the size of the individual netcdf-files otherwise became too large. All changes to the code were done on a lower resolution grid, and once it ran on that grid they were transferred to the high resolution grid.

We have performed a 60 year run with the coupled REcoM2-FESOM in the high resolution setup and are currently assessing the results of this run in terms of nutrient dynamics and primary production (Figure 3). The first results show a relatively good agreement with previous studies (e.g. Popova et. 2012).

Outlook

So far, the relatively coarse COREv2 atmospheric forcing (1.8° resolution) was used in our simulations, which only covers the years 1948-2009. To explore the effect of an atmospheric forcing dataset with a higher spatial resolution, we chose to implement data from the Japanese 55-year Reanalysis (JRA-55) which is updated until present date.

In order to assess future changes in the Nordic Seas and Arctic Ocean, we plan to perform climate projection runs for the time period present-2100 using atmospheric forcing from ECHAM6-MPIOM in the next months. A historic hindcast for the time period 1850-present will serve as a control run.

Publications (in preparation)

Wekerle, C., Q. Wang, S. Danilov, V. Schourup-Kristensen, and T. Jung, *Pathways of Atlantic Waters in the Nordic seas: locally eddy-permitting ocean simulation in a global setup*, in prep.

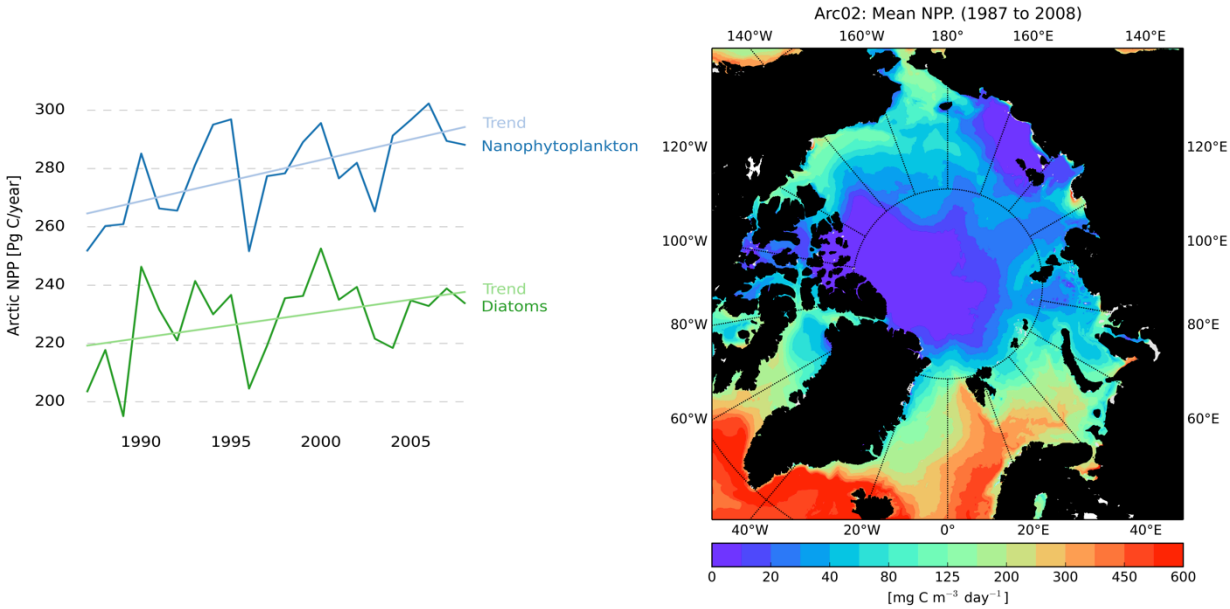

Fig. 3: Left) Total Arctic primary production for the years 1987 to 2007. Right) Spatial distribution of mean vertically integrated primary production.

Presentations

1. Schourup-Kristensen, V., *Arctic Primary Production in a multi-resolution model*, Poster, Forum for Arctic Modeling & Observational Synthesis, 3-6 Nov. 2015, Cape Cod. USA.
2. Wekerle, C., Q. Wang, S. Danilov, V. Schourup-Kristensen, and T. Jung, *Pathways of Atlantic Waters in the Nordic seas: locally eddy-permitting ocean simulation in a global setup*, Poster, Ocean Sciences Meeting, 21-26 Feb. 2016, New Orleans, USA.

References

Beszczynska-Möller, A., Fahrbach, E., Schauer, U., and E. Hansen (2012), *Variability in Atlantic water temperature and transport at the entrance to the Arctic Ocean, 1997-2010*. ICES Journal of Marine Science, 69: 852–863.

Danilov, S., Q. Wang, R. Timmermann, N. Iakovlev, D. Sidorenko, M. Kimmritz, T. Jung, and J. Schröter (2015), *Finite-element sea ice model (FESIM), version 2*, Geosci. Model Dev., 8, 1747-1761.

Popova, E. E., Yool, A., Coward, A. C., Aksenov, Y. K., Alderson, S. G., de Cuevas, B. A., & Anderson, T. R. (2010). *Control of primary production in the Arctic by nutrients and light: insights from a high resolution ocean general circulation model*. Biogeosciences 7(11), 3569–3591.

Schourup-Kristensen, V., D. Sidorenko, D. A. Wolf-Gladrow, and C. Völker (2014), *A skill assessment of the biogeochemical model REcoM2 coupled to the Finite Element Sea-Ice Ocean Model (FESOM 1.3)*, Geosci. Model Dev., 7 (6), 2769-2802.

Wang, Q., S. Danilov, D. Sidorenko, R. Timmermann, C. Wekerle, X. Wang, T. Jung, and J. Schröter (2014), *The Finite Element Sea Ice-Ocean Model (FESOM) v.1.4: formulation of an ocean general circulation model*, Geosci. Model Dev., 7, 663-693.

hbk00045: Determination of vertically resolved trends in the stratospheric ozone from SCIAMACHY limb measurements

HLRNProject ID:	hbk00045
Run time:	IV/2015 – I/2016
Project Leader:	Dr. Alexei Rozanov
Project Scientists:	J. Jia, Dr. N. Rahpoe
Affiliation:	Institute of Environmental Physics, University of Bremen

Overview

Importance of the stratospheric ozone layer has been widely discussed by the scientific community. Playing a key role in the radiative budget of the Earth's atmosphere the stratospheric ozone also protects the biosphere from the harmful UV radiation and is closely related to stratospheric circulation and meteorology. After the anthropogenic emission of several strong ozone depleting substances has been ruled out by Montreal Protocol and its amendments, the severe ozone decline discovered in early eighties of the last century (widely known as Antarctic ozone holes) began to slow down and even some indications of the ozone recovery have been inferred from observations. In the recent time the vertical distribution of stratospheric ozone trends has been moved into the focus. Analyzing vertically resolved time series of ozone in tropics the scientists agree in their conclusions that a strong ozone recovery is seen in the middle to lower stratosphere (below about 30 km) while a significant ozone depletion is observed at altitudes about 35 km. A discussion if the latter phenomenon has purely dynamic or also chemical reasons is currently ongoing in the scientific community. Being vertically integrated these opposite trends result in a slightly positive contribution which explains the signatures of a recovery seen in the observations of ozone total column.

In the framework of this project we analyze global vertical distributions of ozone obtained frommeasurements of the scattered solar lightin limb viewing geometry from the space-borne SCIAMACHY (SCanning Imaging Absorption spectroMeter for Atmospheric CHartograohY) instrument onboard the European satellite Envisat operated from August 2002 to April 2012. During the first phase of the project the retrieval algorithm is to be improved with the main focus to fix previously identified data quality issues. The global data set over the entire operation time of the SCIAMACHY instrument obtained with the improved retrieval algorithm is to be used to determine trends in stratospheric ozone with a particular focus to explain the reported discrepancies between observations from different instruments in the tropical stratosphere. The final goal is to improve our general knowledge on stratospheric ozone trends needed for a better understanding of chemical and dynamic processes in the Earth's atmosphere.

Results

During the first phase of the project a one year data set of the global vertical distributions of ozone has been processed and analyzed with the focus to assess data quality. Thereby some retrieval artefacts have been identified in the analyzed data set which raised a need for a further improvement of the retrieval algorithm. Major efforts have been put to investigate the reasons of the identified artifacts and find the way to fix the issue. The final data set re-

processed with the improved retrieval algorithm has been found to be free or any artifacts. A first validation of the obtained sub-set of the ozone data has been done using independent space-borne measurements in limb viewing geometry performed by the MLS (Microwave Limb Sounder) instrument onboard the Aura satellite of NASA.

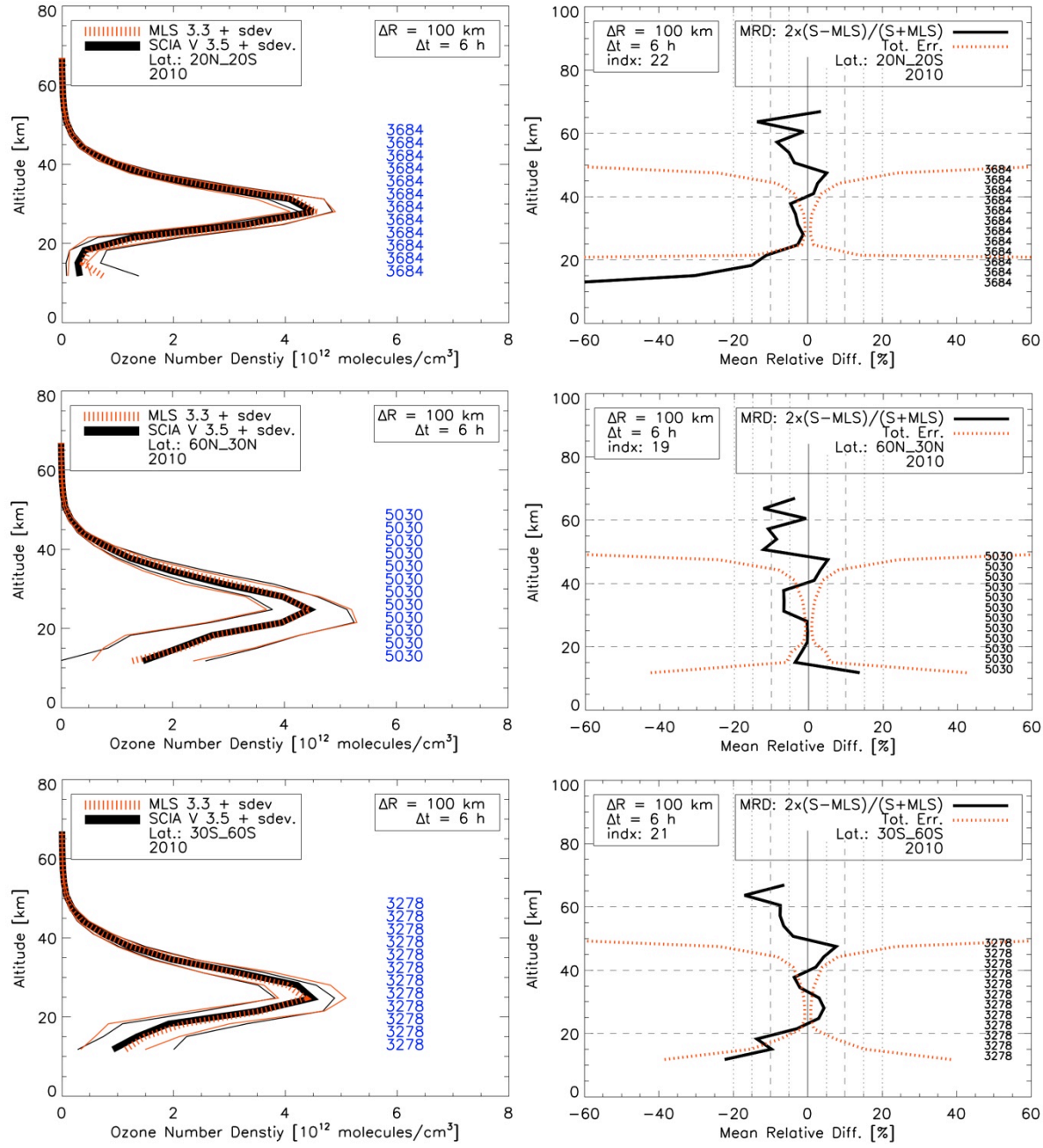

Figure 1: Left panels show average ozone number density profiles form SCIAMACHY (thick black line) and MLS instruments (dotted red line) for different latitude ranges (20S – 2ON, 30N – 60N, 30S – 60S in upper, middle and lower panels, respectively). The thin lines show the standard deviations of the SCIAMACHY and MLS results in black and red respectively. The blue numbers denote the number of co-locations. Right panels show the mean relative difference between the SCIAMACHY and MLS results (solid black lines) and the standard deviation of the relative differences (dotted red lines).

The comparisons were done for a one-year global data set (2010) using co-located data pairs with maximum distance of 100 km and maximum time difference of 6 hours. The overview of the comparison results for three latitude bands is presented in Figure 1. The upper, middle and lower panels of the plot show the results for 20°S – 20°N, 30°N – 60°N and 30°S – 60°S latitude bands respectively. Left panels show average ozone number density profiles form SCIAMACHY and MLS instruments by thick black and dotted red lines, respectively. The thin linesof the respective colors show the standard deviations of the SCIAMACHY and MLS results. The blue numbers denote the number of co-location pairs. Right panels show the mean relative difference between the SCIAMACHY and MLS results (solid black lines) and the standard deviation of the relative differences (dotted red lines).

As one can see from the plot, a very good overall agreement is seen between the two data sets. The best quality of the agreement is reached between 20 and 40 km, where the relative differences are mostly below 5% and the standard deviations of the relative differences are in a few percent range. Below 20 km the agreement is still quite good for mid-latitudes ranging from mostly below 10% in the northern hemisphere to 10 - 20% in the southern hemisphere. Below 18 km in the tropics the agreement gets as expected worse displaying very high standard deviations of the relative errors and the mean realitive error up to 60%. This is because the instruments are often looking into a highly variable troposphere where the time difference of 6 hours might be inappropriate. Furthermore very low ozone values in the tropical lower atmosphere make the retrieval much more challenging compared to middle and high latitudes. A similar increase in the standard deviation of the relative difference is observed above 45 km associated with low ozone amount and decreasing signal to noise ratio in the measured spectra. However, the mean relative difference between the two data sets remain within 10 – 15% indicating that the differences are mainly caused by the random errors (e.g. measurement noise).

With respect to obtaining a high quality vertically resolved ozone data set from SCIAMACHY limb measurements a very good agreement of mostly below 5% found for two data sets form the lower to upper stratosphere is very promising.

Outlook

After the full data set from SCIAMACHY limb measurements (August 2002 – April 2012) has been processed an evaluation of the time series is to be done with the focus to identify possible artifacts in the temporal behavior. Thereafter a trend analysis is to be performed to investigate vertically resolved changes in the stratospheric ozone. The results are to be compared with previously obtained data and results from other space-borne instruments.

6.16 *hbk00046:* Understanding Antarctic phytoplankton response to environmental change studied by a synergistic approach using modelling and satellite data

HLRNProject ID:	hbk00046
Run time:	III/2015 – III/2016
Project Leader:	Prof. Dr. Astrid Bracher[1]
Project Scientists:	Svetlana Losa[2], Martin Losch
Affiliation:	Alfred Wegener Institute Helmholtz Centre for Polar and Marine Research, Bremerhaven [1] also professor at University of Bremen [2] project administrator

Overview

The proposed project focuses on the assessment of the impact of environmental change in the Southern Ocean on phytoplankton. The phytoplankton dynamics as well as phytoplankton diversity in response to environmental changes will be simulated with the biogeochemical model Darwin (Follows et al., 2007) coupled to the Massachusetts Institute of Technology General Circulation Model (MITgcm, MITgcm Group, 2012). The model performance will be evaluated with the Southern Ocean synergetic multi- and hyper-spectral satellite phytoplankton functional group (PFT) data product covering the period of 2002-2012 (or present). Combined with modelling studies, this unique global long-term information on phytoplankton composition will be used to attribute the relative importance of anthropogenic activity and natural phenomena on the marine ecosystem of and biogeochemical cycling in the Southern Oceans during the last decades.

The project is based on the study by Taylor et al. (2013), where, following Strass et al. (2002) and Arrigo et al. (2008), the authors investigated impacts of different environmental conditions and physical factors on the variations in chl-a concentration and primary production. We further extend this study by considering the distribution and variation not only of the total biomass but also of major phytoplankton functional types (PFTs). The PFTs have very different functions within the biogeochemical cycle and the marine food web. However, because of difficulties in obtaining sufficient in-situ sampling the spatial-temporal variability of PFTs in the Polar Regions, there is still little information on PFTs' relationship with the climate variability in the Southern Ocean. Alvain et al. (2013) assessed the dynamics of diatoms in the Southern Ocean driven by environmental variability from 1998 to 2008. Analysing in-situ and satellite observation and ecosystem model simulations, the authors reported on a large-scale shift of diatoms dominance related to the positive phases of the Southern Annular Mode. However, this study was limited to investigating only the diatoms dynamics when these species dominate over the total phytoplankton biomass. Thus, the variability of other PFTs and diatoms as not a dominant PFT remains unknown. The aim of the current project is to improve our long-term knowledge of phytoplankton composition with sufficient spatial coverage in order to adequately estimate the primary production and accurately assess the different roles and contribution of the various phytoplankton types in the oceanic carbon cycle and specifically in the Southern Ocean.

Results

A version of the Darwin ocean biogeochemical model coupled to the MITgcm general circulation model (Follows et al., 2007, Prowe et al., 2014, Dutkiewicz et al., 2015) is used to simulate the dynamics of various phytoplankton functional types (Fig. 1): analogues of diatoms, other larger eukaryotes, *Synechococcus*, high and low light *Prochlorococcus*, nitrogen fixing *Trichodesmium*, unicellular diazotrophs, small eukoryotes and coccolithophores.

Following Taylor et al. (2013) we use the circulation model configuration based on a cubed-sphere grid (Menemenlis et al. 2008) with mean horizontal spacing of ~18 km and 50 vertical levels with the resolution ranging from 10 m near the surface to ~450 m in the deep ocean.

The model is forced by 6-houly atmospheric conditions from the NCEP Climate Forecast System Reanalysis (CFSR).

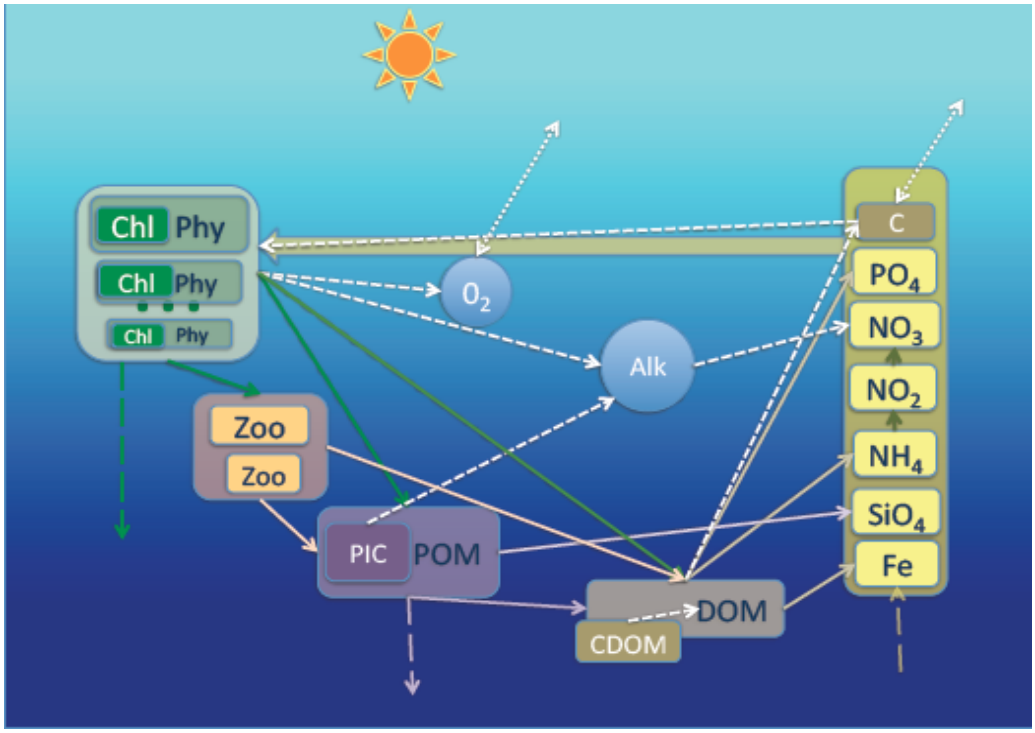

Figure 1: The schematic diagram of the DARWIN biogeochemical model (produced in accordance with the model description by Dutkiewicz et al., 2015).

Several Darwin configurations – excluding and including carbon cycling, considering various compositions of PFTs, with dynamically evolved chlorophyll and assumed constant stoichiometry, – have been tested. The currently used Darwin setup contains 6 PFTs. Figure 2 depicts spatial distribution of 6 phytoplankton types after one year of model integration. A series of experiments with different values of biogeochemical parameters has to be conducted in order to accurately calibrate and evaluate the coupled model.

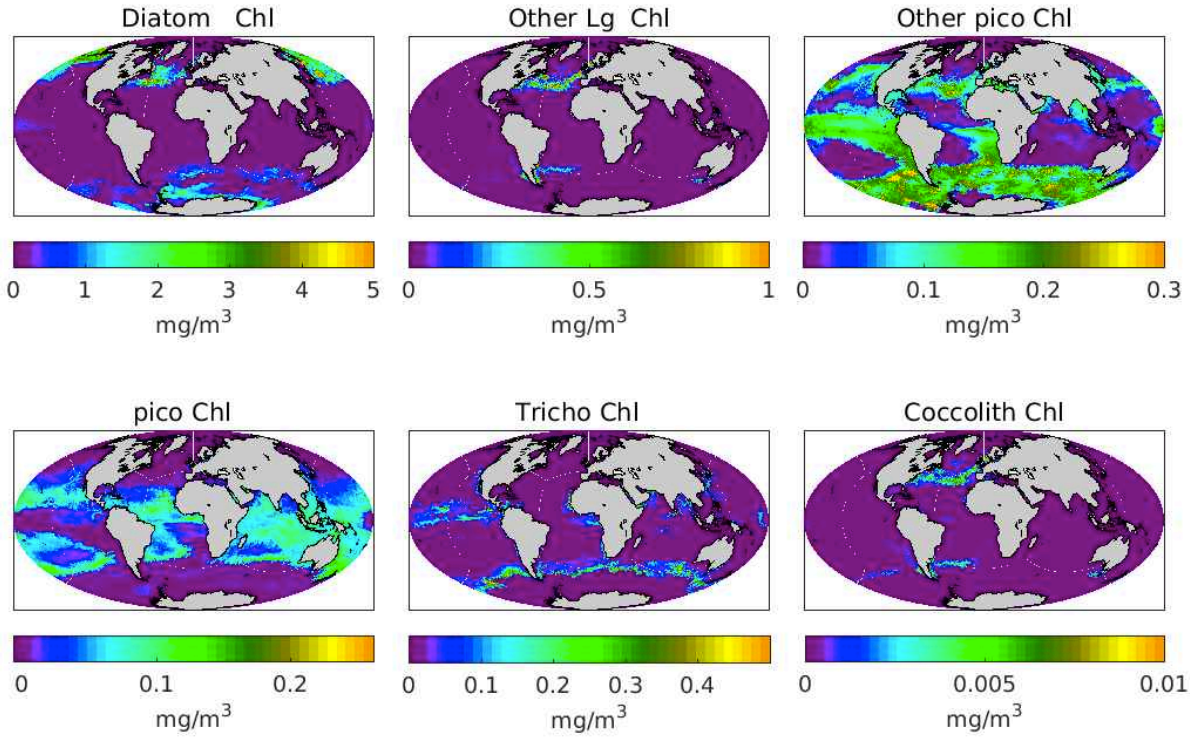

Figure 2: Spatial distribution of 6 PFTs after 1 year of Darwin-based model integration started from the same initial condition.

Outlook

The biogeochemical model sensitivity study will be further continued in order to correctly simulate the observed phytoplankton dynamics and the diversity among dominating phytoplankton groups in the Southern Ocean. The solution will be evaluated against PhySyn satellite data product. The satellite-derived information on phytoplankton composition will be obtained by a generic method based on an analytical bio-optical retrieval (PhytoDOAS from Bracher et al. 2009, Sadeghi et al. 2009 and now improved at IUP within thisproject). The methods will use all available high spectral-resolution optical satellite data, which are complemented by in-situ and multi-spectral satellite data.

The spatial and temporal variability of Antarctic phytoplankton, estimated based on the Darwin-based coupled ecosystem-ocean-ice-model simulations in/with support to/from the synergetic PFTs satellite data product, and their link to changes in the environmental conditions (e.g. sea surface temperature, mixed layer depth, surface wind speed, nutrients) will be statistically analysed.

References

- Alvain S, Le Quéré C, Bopp L, Racault MF, Beaugrand G, Dessailly D, Buitenhuis E (2013) Rapid climatic driven shifts of diatoms at high latitudes. Remote Sensing of Environment 132:195-201.
- Arrigo KR, etal (2008) Primary production in the Southern Ocean, 1997-2006. JGR 113C8: C08004.

- Bracher A., Vountas M., Dinter T., Burrows J.P., Röttgers R., Peeken I. (2009) Quantitative observation of cyanobacteria and diatoms from space using PhytoDOAS on SCIAMACHY data. Biogeosciences 6: 751-764.
- Dutkiewicz, S. , Hickman**,** A. E. , Jahn**,** O., Gregg**,** W. W., C. B. Mouw**,** C. B. , and M. J. Follows (2015) Capturing optically important constituents and properties in a marine biogeochemical and ecosystem model Biogeosciences, 12, 4447-4481.
- Follows, M. J., Dutkiewicz, S., Grant, S., and Chisholm, S. W. (2007) Emergent biogeography of microbial communities in a model Ocean, Science, 315, 1843–1846.
- Menemenlis, D., Campin, J.-M., Heimbach, P., Hill, C., Lee, T., Nguyen, A., Schodlock, M., and H. Zhang (2008). High resolution global ocean and sea ice data synthesis (2008) Mercator Ocean Quartely Newsletter, 31, 13–21.
- MITgcm Group (2012), MITgcm Manual, Online documentation, MIT/EAPS, Cambridge, MA 02139, USA.
- Prowe, A. E. F., Pahlow, M., Dutkiewicz, S., and A. Oschlies (2014) How important is diversity for capturing environmental-change responses in ecosystem models? Biogeosciences, 11, 3397–3407.
- Sadeghi, A., Dinter, T., Vountas, M., Taylor, B. B., Altenburg-Soppa, M. Peeken, I.,and A. Bracher (2012) Improvements to the PhytoDOAS method for identification of coccolithophores using hyperspectral satellite data. Ocean Sciences 8:1055-1070.
- Strass VH, Naveira Garabato AC, Bracher AU, Pollard RT, Lucas MI (2002) A 3-D mesoscale map of primary production at the Antarctic Polar Front: results of a diagnostic model. Deep Sea Res. 49: 3813-3834.
- Taylor MH, Losch M, Bracher A (2013) On the drivers of phytoplankton blooms in the Antarctic seasonal ice zone: a modelling approach. J. Geophys. Res. – Oceans 188: 63-75.

6.17 *hbp00003:* Encounters of Neutron Stars

HLRN-Projektkennung:	hbp00003
Laufzeit:	IV/2010 – IV/2016
Projektleiter:	Prof. Dr. C. Lämmerzahl, Prof. Dr. S. Rosswog
Projektbearbeiter.	Emanuel Gafton, Emilio Tejeda
Institut / Einrichtung:	ZARM, Universität Bremen; Oskar Klein Centre for Cosmoparticle Physics, Stockholm University, Stockholm, Sweden

Overview

- Mergers of two compact objects (neutron stars or black holes) are the prime targets of existing **gravitational wave** detectors. Four decades of preparatory work recently been crowned by the first ever direct detection of gravitational waves from two merging black holes.
- If at least one neutron star is involved, such mergers eject very neutron-rich matter which (via a so-called "rapid neutron capture process") produces the **heaviest elements in the Universe** (like platinum, gold or uranium).
- There is an interesting link between these two topics: the radioactive decay of freshly produced heavy elements produces an electromagnetic flash **"macronovae"** that will help to localized the gravitational wave source in the sky. Without such a transient the source is very difficult to localize: for the first detection of two merging black holes the sky localization is only known to within 600 square degrees (apparent size of the full moon: 0.3 square degrees).
- We had used a large part of our HLRN computing time to predict such macronovae. In June 2013, the first ever example of a macronova has been detected with properties close to our predictions. This observation boosts the confidence that mergers of compact objects are major sources of the heaviest elements in the cosmos.

Introduction

Stars with more than eight solar masses end their lives in cataclysmic fireworks called supernovae. During this explosion their luminosity rivals those of whole galaxies. Supernovae eject most of their mass into space where it forms the basis for the next generation of stars. The stellar centres, however, become enormously compressed and – if the star was not too massive – the explosion produces a neutron star, or otherwise a black hole of a few solar masses. Neutron stars can be thought of as gigantic atomic nuclei: with a mass of about 1.4 solar masses and radii of only 12 km their central densities substantially exceed the density in an atomic nucleus ($\rho_{nuc} = 2.7 \times 10^{14}\, gcm^{-3}$).

In some cases these exotic stars are observed in binary systems where they orbit their common centre of mass. Due to their enormous compactness, such stars can revolve around each other at very small separations and in such systems strong-field gravity effects become important, making such systems excellent laboratories to test theories such as Einstein's theory of General Relativity. In fact, the first indirect evidence for the existence of gravitational waves came exactly from such a system and it earned its discoverers, Russel

Hulse and Joseph Taylor, the Nobel Prize for Physics in 1993. One implication of the emission of gravitational waves is that the binary orbit shrinks further until the stars finally merge. This releases gigantic amounts of gravitational energy, more than the Sun could radiate away during the whole lifetime of the Universe. The final merger most likely causes (a fraction) of the brightest explosions in the Universe since its beginning in the Big Bang, so-called Gamma-Ray Bursts.

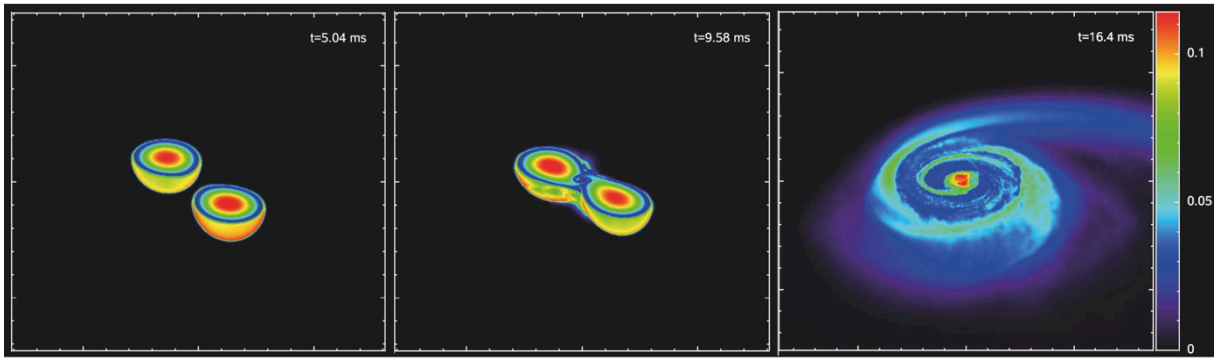

Fig. 1: Merger of a 1.4 and a 1.5 $M_\odot$ neutron star. Shown are volume renderings of the electron fraction (= number of electrons per nucleon). This quantity is pivotal for the resulting formation of heavy elements via the rapid-neutron capture process. To allow a view inside, only the lower part of the matter distribution is visualized. From Rosswog et al. in prep. (2016).

On September 14, 2015, the American LIGO detectors detected for the first time directly a gravitational wave: they saw the inspiral and final merger of 29 and an 36 $M_\odot$ blackhole. In our HLRN project we study the question how different mergers and collisions are in a) their gravitational wave, b) neutrino and c) electromagnetic emission. Moreover, we want to understand d) what their contribution to the cosmic inventory of heavy nuclei is.

Recent Results

We have performed a very large set of simulations where we have explored the parameter space of neutron star mergers with unprecedented breadth and numerical resolution. Such a merger ejects ~ 1% of a solar mass in extremely neutron rich matter: out of 100 nucleons only 3 are protons, the rest are neutrons. These are ideal conditions for the formation of heavy elements via "rapid neutron capture" or "r-process". Indeed our calculations show that in this way a very robust pattern of nuclear abundances is produced that is very similar to what is observed throughout the Universe (the solar system and various stars).

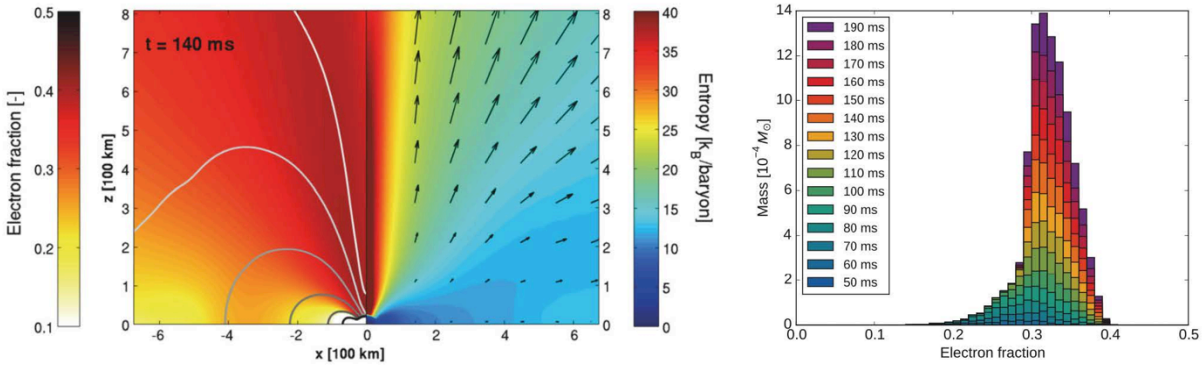

Fig. 2: Neutrino-driven wind blown of the remnant of two merged neutron stars. The left panel shows a snapshot of the electron fraction Y_e and entropy, the right one summarizes the Y_e evolution. From Martin et al. (2015).

A major focus in the last year has been this type of element formation and in particular the electromagnetic transients that are produced by the radioactive decays of the freshly produced nuclei. These transients called "macronovae" are a crucial link between ifferent phenomena: gamma-ray bursts, enormously bright flashes of gamma-rays, gravitational waves and – of course – the formation of the heaviest elements in the cosmos. The importance of macronovae comes through the complementary information they provide: from the gravitational wave signal one can extract the parameters of the merging system (masses, spins etc.), but – since the sky localisation through gravitational waves is very poor (the first ever gravitational wave detection could – due to the absence of an electromagnetic signal – only be localized to 600 square degrees; the full moon as seen from Earth has only 0.3 square degrees) – one is essentially blind with respect to the astrophysical environment in which the merger occurs. If detected coincidently in electromagnetic waves, one learns in addition to the binary parameters also about the astrophysical environment, say the type of host galaxy, the density of the surrounding medium etc. This can provide on the one hand confidence about the nature of the gravitational wave source, but on the other hand also constrains the stellar evolution of binary stars.

In the least year we have mainly focussed on the prediction of such electromagnetic transients. They are ejected via several channels: extremely neutron-rich matter is ejected via dynamic (hydrodynamic and gravitational) interaction and a second channel, somewhat proton-richer, is blown off the merged remnant via neutrinos. A remnant emits neutrinos at enormous luminosities: they are about 20 orders of magnitude(!) larger that the (electromagnetic) luminosity of our Sun. As we have found in recent studies (Perego et al. 2014, Martin et al. 2015), neutrinos emitted in one part of the remnant can be absorbed in another part and this blows off a strong wind from the remnant, see Fig 2. This wind causes a different type of electromagnetic emission, directly following a gravitational wave event.

Outlook

We have investigated in detail the fate of two compact objects, either neutron stars or a neutron star with a stellar-mass black hole, that either merge after having having been driven together by the emission of gravitational waves or that collide dynamically, say, in a Globular Star Cluster. We have predicted in detail the observable signatures in various channels: gravitational waves, neutrinos and electromagnetic emission ("macronova"). In June 2013 the first ever macronova event has been detected, with properties close to our predictions. Such predictions will substantially enhance the effective sensitivity of existing gravitational wave detector facilities such as Geo600, LIGO, VIRGO. Our current and future efforts focus on enhancing and refining further the physics input in our simulations (more General Relativity, more refined nuclear heating physics, more sophisticated neutrino treatment) and on implementing computationally more efficient gravity solvers.

Publications from 2015 HLRN results

[1] *The Role of Fission in Neutron Star Mergers and the Position of the Third r-Process*, Eichler et al., ApJ 808, 13 (2015)

[2] *Multi-messenger picture of compact binary mergers*, S. Rosswog, International Journal of Modern Physics D 24, 1530012 (2015)

[3] *SPH methods in the modelling of compact objects*, S. Rosswog, Living Reviews of Computational Astrophysics 1, 1 (2015)

[4] *The Fate of the Compact Remnant in Neutron Star Mergers*, C. Fryer, C. Belczynski, E. Ramirez-Ruiz, S. Rosswog, G. Shen, A. Steiner, ApJ, 812, 11 (2015)

[5] *Neutrino-driven Winds in the Aftermath of a Neutron Star Merger: Nucleosynthesis and Electromagnetic Transients,* D. Martin, A. Perego, A. Arcones, F.K. Thielemann, O. Korobkin, S. Rosswog, Astrophysical Journal 813, 14 (2015)

[6] *Relativistic effects on tidal disruption kicks of solitary stars* Gafton, E.; Tejeda, E.; Guillochon, J.; Korobkin, O.; Rosswog, S., MNRAS 449, 771 (2015)

[7] *The interplay of disc wind and dynamical ejecta in the aftermath of neutron star-black hole mergers* Fernandez, R.; Quataert, E.; Schwab, J.; Kasen, D.; Rosswog, S.; MNRAS 449, 390 (2015)

[8] *Magnetohydrodynamical simulations of a deep tidal disruption in general relativity*, O. ASadowski, E. Tejeda, E. Gafton, S. Rosswog, D. Abarca, MNRAS , 03, (2016)

[9] *Optical Thermonuclear Transients from Tidal Compression of White Dwarfs as Tracers of the Low End of the Massive Black Hole Mass Function* M. McLeod, J. Guillochon, E. Ramirez-Ruiz, D. Kasen, S. Rosswog, ApJ 819, 17 (2016)

Several papers from HLRN calculations are currently in preparation

Selection of scientific talks where this work was presented

- *Disruptions of stars by massive black holes*
  Jena, January 27, 2016
- *Multi-messenger signatures form neutron star mergers*
  ECT* Trento, From rare isotopes to neutron stars, Sept 14 - 18, 2015
- *Gravitational waves, electromagnetic transients and cosmic nucleosynthesis*
  EWASS Meeting, Teneriffa, June 24, 2015
- *Towards a multi-messenger picture of compact binary mergers*
  Turku, Finland, March 26, 2015
- *Electromagnetic transients from compact binary mergers*
  Lund, Sweden, Feb 10, 2015
- *Synergy of gravitational waves and electromagnetic signals*
  Leiden, Netherlands Feb 04, Compact Objects as Astrophysical and Gravitational Probes Feb 02-06, 2015

Public Outreach

Some of the simulations and visualizations produced on HLRN have been selected for the **Multimedia performance "The Warped Side of the Universe"** with **Kip Thorne** (Caltech), **Paul Franklin** (Academy Awards/Oscar for the Best Visual Effects for the movies "Inception" (2011) and "Interstellar" (2015)) and **Hans Zimmer** (Academy Award/Oscar for Best Music "Lion King" (1995) plus 8 additional Oscar nominations)

6.18 *hbp00019:* Dynamics and Interactions of Semiconductor Nanowires for Optoelectronics

HLRN Project ID:	hbp00019
Run time:	II/2012 – II/2016
Project Leader:	Prof. T. Frauenheim
Project Scientists:	Dr. M. Lorke
Affiliation:	Bremen Center for Computational Material Science (BCCMS), University of Bremen

Overview

Surface modifications have been shown to alter electronic and optical properties of ZnO nanostructures. The electronic structure of europium doping in ZnO has been investigated

We could identify the defect complex responsible for the emission of europium in ZnO.

Results

The aim of this project is to investigate the electronic and optical properties of semiconductor nanowires via surface modification and doping by using first principles density-functional theory (DFT) and many body approaches (GW and Bethe-Salpether equations). These investigations are embedded in the DFG research unit For1616: Dynamics and interaction of Semiconductor nanowires for Optoelectronics.

One possible strategy for surface modification involves attachment of functional groups to the nanowire surfaces. Furthermore, the electronic and optical properties of such nanowires will be modified by doping with rare-earth and transition metal elements and the potential of these systems for applications in optoelectronics devices will be investigated. There is considerable technological interest in functionalizing the surface of semiconductor nanostructures with organic molecules in order to obtain hybrid materials with novel properties, which include sensors with high selectivity and sensitivity, solar cells and light-emitting diodes (LEDs). In the last project period, we have investigated the electronic properties of ZnO surfaces and NWs modified by several functional groups. We found that the behavior of the investigated molecules is very similar on both surfaces and NWs. After structural optimization, we observe that both -COOH and -SH molecules adsorb in a dissociative manner, while -NH2 obeys a non-dissociative regime. Our results suggest that functionalization with carboxylic acids or amines does not alter the transport and conductivity properties of ZnO nanostructures due to the presence of almost flat band conditions. In contrast, the functionalization with thiols might offer a route for modification of optical properties of ZnO nanomaterials due to the appearance of molecular states in the energy gap. Our results provide new insights to improve the physical properties of oxidenanostructures and surfaces for device applications. The band alignment for the structures was done with respect the vacuum level, setting the bare surface as reference. This was done after the alignment of bare surface considering the bulk potential has shown that the VBM does not shift significantly between the bulk and the bare surface.

We have investigated Eu-doped ZnO in the presence and absence of intrisic defects. The correct position of the Eu-f states in the band gap is of paramount importance for the understanding of carrier transfer into the Eu states, as well as how defect complexes effect these energetic positions and the emission. For this purpose the many-body GW0 method is appropriate, as it stems from a systematic approximation scheme to many-particle effects. We find that the position of Eu-f states is strongly dependent on the environment around the Eu atom. We also investigated in detail the energetics of the defect complexes. The formation energy for all defect complexes both under oxygen rich and oxygen poor conditions is shown in Fig. 1. We clearly see, that under experimentally relevant oxygen rich conditions, the octrahedral interstitial, that we previously found to be likely responsible for the europium emission from ZnO, is one of the most stable defect complexes.

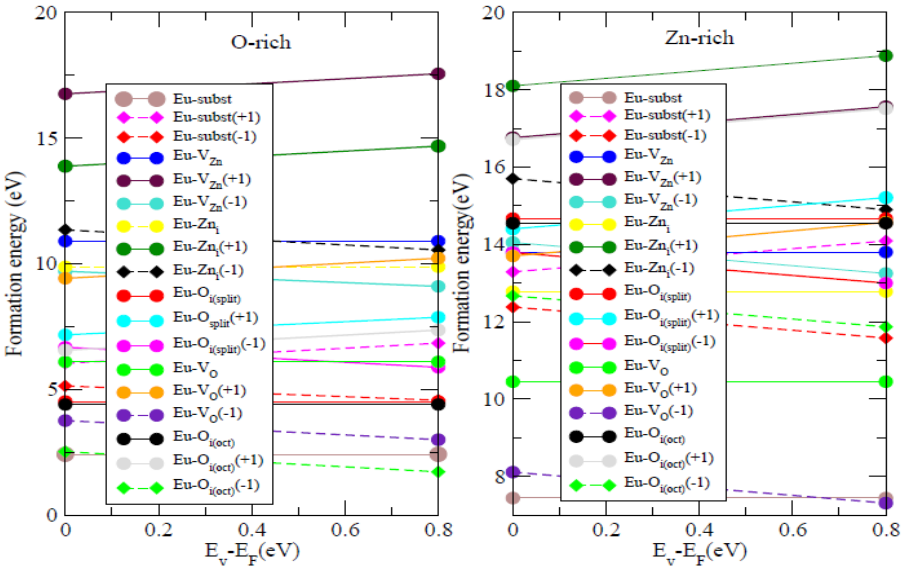

Figure 1: Formation energy of various defect complexes in europium doped ZnO

Moreover, we investigated the electronic structure of all defect complexes using many-body methods, such as the GW0 approximation. An example is shown in Fig. 2, where we show the density of states for an europium+oxygen vacancy defect complex in ZnO. Clearly visible are both the Eu f states in the upper half of the band gap as well as the oxygen vacancy state at 0.8eV above the valence band maximum. Also the ZnO bandgap is found at 3.6eV, in good agreement with the experiment.

In Fig. 3 we show the electronic structure for the europium+oxygen interstitial defect complex in ZnO. Six europium f-states are occupied and one is unoccupied, which directly tallies with the experimentally observed ground state.

Outlook

In the future, we will investigate the second main material system of the research group For1616 which is GaN. As for ZnO we will investigate defects for their potential for single photon emission as well as surface functionalizations.

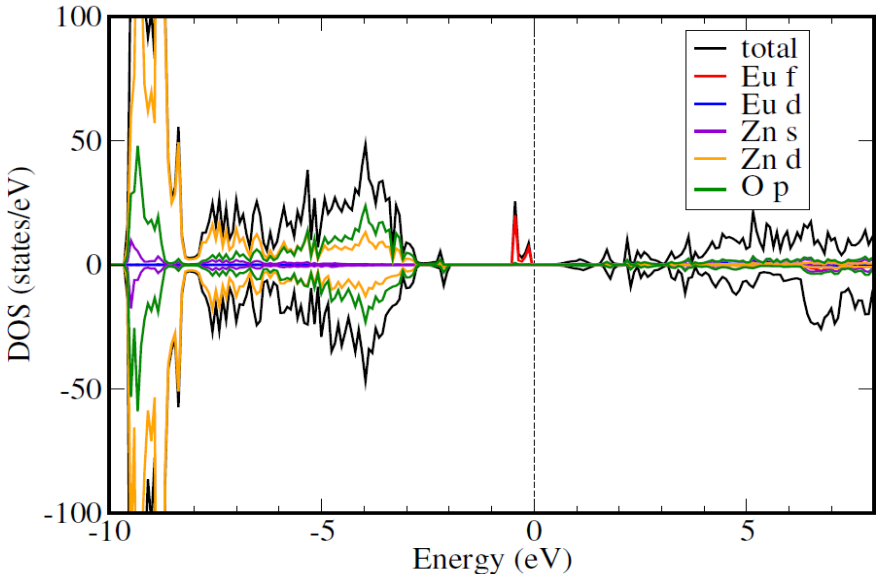

Figure 2: Density of states for an europium+oxygen vacancy defect complex in ZnO

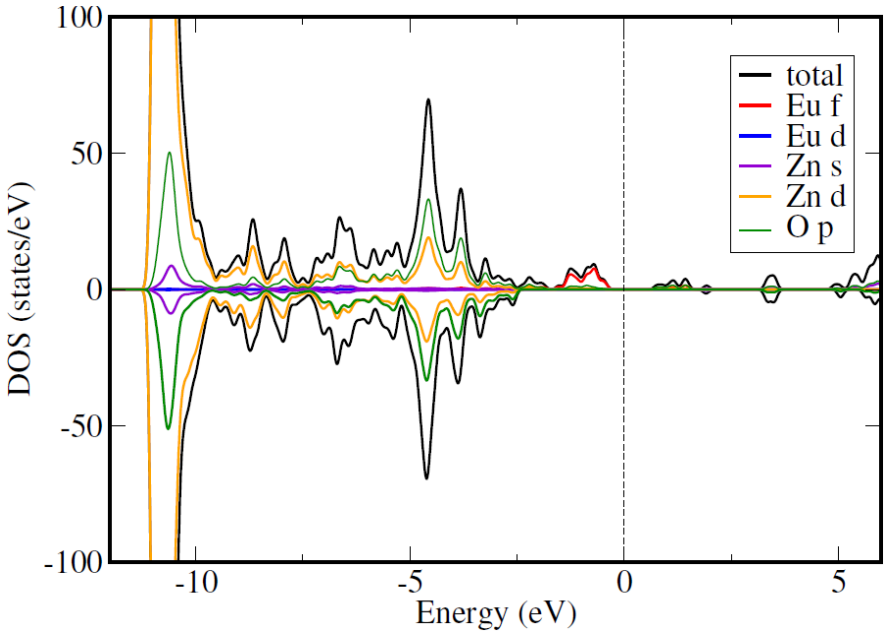

Figure 3: Density of states for an europium+oxygen interstitial defect complex in ZnO

Publications

Lorke M, Frauenheim T, Rosa A, Many-body electronic structure calculations of Eu-doped ZnO, Physical Review B (2016)

Presentations

Lorke, M. Frauenheim T, Rosa A, Many-body electronic structure calculations of Eu doped ZnO, invited talk, Jena 2015

6.19 *hbp00024*: Correlation and Interaction Effects in Low Dimensional Systems

HLRNProject ID:	hbp00024
Run time:	IV/2014 – III/2016
Project Leader:	Prof. Dr. Tim O. Wehling
ProjectScientists:	Dr. S. Barthel, M. Rösner, G. Schönhoff, M. Schüler
Affiliation:	Institut für theoretische Physik and Bremen Center for Computational Material Science, Universität Bremen

Overview

The project aims at studying the competition between local and non-local Coulomb terms and pronounced electron-phonon interactions in real material contexts. First, we aimed to consider many-body instabilities in extended two dimensional systems like transition metal dichalcogenides (TMDCs), which are triggered by a complex interplay of electron-phonon and electron-electron interactions. Secondly, we studied the problem of competing interactions in impurity systems, such as magnetic transition metal atoms on substrates and in bulk materials, which present model systems to understand local correlation effects induced by different Coulomb terms like on-site repulsion or Hund's exchange. Both parts are meant to serve the long term goal of understanding how interactions determine excitations and thermodynamic phases of realistic low dimensional electron systems.

Results

Impurity Systems

We have studied impurity systems in bulk host materials and on surfaces by combining ab-initio density functional theory (DFT) and quantum Monte Carlo (QMC) simulations of resulting Anderson impurity models (AIM). In the course of the project we have focused on two sets of systems, namely Fe impurities in Au and on alkali surfaces (Li and Na).

In the context of Fe impurities in Au, we have extensively investigated the nature of the electronic ground state of the impurity in different flavors of density functional theory. Besides plain DFT calculations, we have also used local Coulomb matrix elements treated in mean field (LDA+U) with different strengths of the local interaction. Thereby the so called double counting problem arises which we studied using different methods. The different approaches lead to different ground states, all very close in energy but with distinct magnetic properties as seen in form of vast different amounts of local spin moments. Our results indicate that quantum mechanical fluctuations between these groud states likely determine the physical properties of this system.

Experiments concerning Fe impurities on alkali surfaces have shown that the magnetic susceptibility of Fe adatoms on alkali surfaces is quenched when going from Na to Li substrates. In order to address the microscopic mechanisms behind this observation by theoretical means we performed combined DFT and QMC calculations. A natural scenario in which the experimentally observed quenching of the susceptibility from Li to Na can be explained is the so-called Kondo effect, i.e. screening of the local magnetic moment by bath electrons. And indeed, detailed analysis of the hybridization function and the effects of the Coulomb tensor at different temperatures show that the Kondo effect plays an important role

in the physics of these systems. We found the scenario that the quenching of the susceptibility is due to Kondo screening is very likely here.

Many-body instabilities and collective excitations in Two Dimensional Systems

In the context of electron-electron interactions we developed a parallelized code to calculate response functions and to derive corresponding collective electronic modes for doped transition metal dichalcogenides (based on former results published in Nano Lett. [3]) in the so-called random phase approximation (RPA) [4]. Using this code, we were able to calculate the effective Coulomb repulsion parameter μ* which is a major ingredient to the so-called Allen-Dynes theory to describe superconducting properties like corresponding transition temperatures. Previously, this parameter was assumed to be fixed μ*=0.13 for thin flakes of MoS_2. However, our calculations show that this parameter strongly depends on the electron doping level as it can be seen in Fig. 1. We find values of the order μ*=0.30 for small doping concentrations and μ*=0.15 for high doping levels. As enhanced Coulomb scattering which corresponds to an enhanced parameter μ* supresses superconductivity we thus found a possible reason for decreased superconductivity transition temperatures in measured in doped TMDC monolayer as compared to bulk systems.

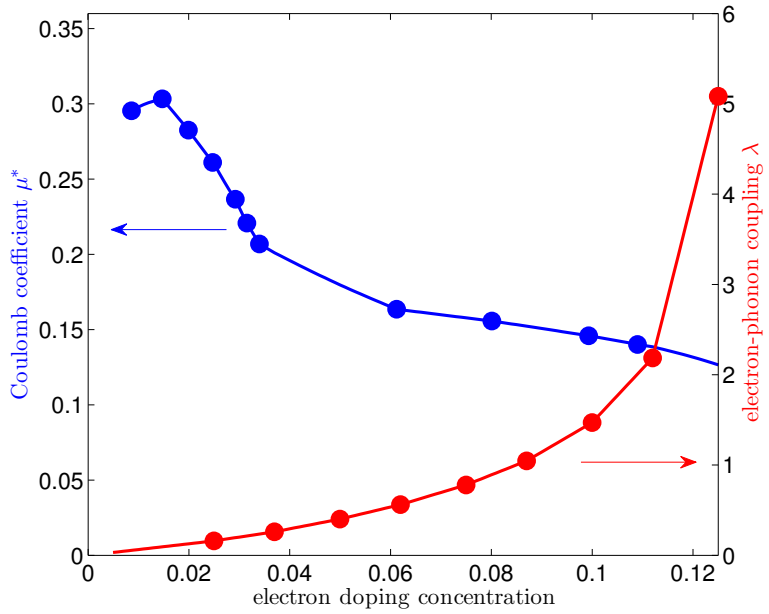

Fig. 1: Effective Coulomb repulsion μ* (blue) and effective electron-phonon coupling constant λ (red) in dependence of the electron doping level for free standing monolayer MoS_2..

Recently, we extended our RPA code to include important spin-orbit coupling effects and screening effects due to the environment. The latter is derived based on a former study published in Phys. Rev. B [5] and allows for a description of realistic experimental setups including substrates and adsorbates of 2d materials. With these developments we are now able to calculate electron-energy loss spectra as measured in corresponding experiments which can be used to investigate plasmonic excitations. In Fig. 2 we show corresponding energy loss spectra for MoS_2 monolayers in varying dielectric surroundings for different doping levels. We find a strong dependence of the plasmonic properties (dark line) to both, the dielectric surrounding and the doping level.

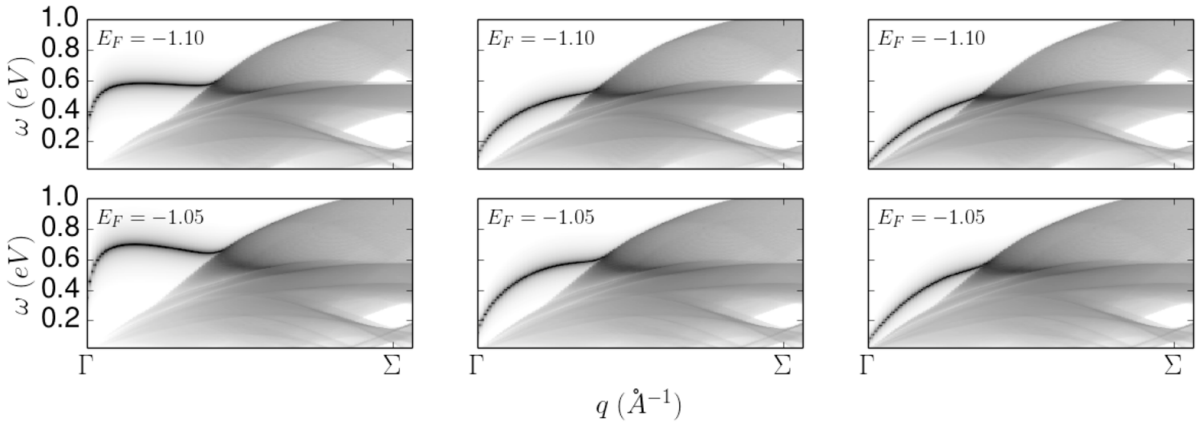

Fig. 2: Electron-energy loss spectra (EELS) for MoS_2 monolayer in varying dielectric environments (ε = 1, ε = 10, ε = 50 from left to right) and for different doping concentrations (upper row: small doping concentration, lower row: increased doping concentration).

Outlook

Altogether, we arrived now at a point at which we are able to calculate all of the four model ingredients (i.e. electronic band structures, phonon band structures, screened Coulomb interactions, electron-phonon coupling) to describe layered materials accurately in a variety of different doping / screening situations. In the upcoming project phase we will investigate the combined effects of all ingredients within the so-called Eliashberg theory (a generalization of the Allen-Dynes description). Thereby, we will be able to realistically describe superconductivity and competing further instabilities like charge density waves. Hence, we will gain a comprehensive picture of interaction induced correlation effects in these low-dimensional systems.

Publications

1. S. Yuan, M. Rösner, A. Schulz, T. O. Wehling, and M. I. Katsnelson, Phys. Rev. Lett. **114**, 047403 (2015)
2. M. Rösner, S. Haas, and T. O. Wehling, Phys. Rev. B **90**, 245105 (2014)
3. A. Steinhoff, M. Rösner, F. Jahnke, T. O. Wehling, and C. Gies, Nano Lett. **14**, 3743 (2014)
4. R. E. Groenewald, M. Rösner, G. Schönhoff, S. Haas, and T. O. Wehling, arXiv: 1601.01707 (2016)
5. M. Rösner, E. Şaşıoğlu, C. Friedrich, S. Blügel, and T. O. Wehling, Phys. Rev. B **92**, 085102 (2015)

Presentations

1. M. Rösner, *Electronic excitations in transition metal dichalcogenides under the influence of dielectric environments*, DPG-Frühjahrstagung, Regensburg (2016)
2. M. Rösner, *Description and Tuning of Many-Body Effects,* Workshop of the WP3 of the "Graphene Flagship" program, Zürich (2016)
3. M. Rösner, *Many-body and disorder effects: The role of fluorination and dielectric substrates*, Workshop of the DFG Priority Program 1459 "Graphene", Kremmen (2015)

6.20 *hbp00027:* Computational prediction and control over opto-electronic properties in novel 2D semiconductors by defect and interface engineering

HLRNProject ID:	hbp00027
Run time:	I/2015 – I/2016
Project Leader:	Prof. Dr. Thomas Frauenheim
Project Scientists:	Dr. Liujiang Zhou, Dr. Bin Shao
Affiliation:	Bremen Center for Computational Materials Science, University of Bremen

Overview

Graphene, a two-dimensional one-atom-thick honeycomb-like layered material, possesses intriguing electronic and mechanical properties and is highly desired in the field of next generation of faster and smaller electronic devices. However, the feature of zero band gaps makes it unsuitable for the controlled and reliable transistor operation and consequently limits its widespread applications in optoelectronic devices. So far, graphene or graphene-like two-dimensional (2D) nanomaterials with mediate band gaps (i.e., 1.0−2.0 eV) that are highly desired by the field effect transistor and solar cell are still practically difficult to be realized.[7] It is therefore highly desired to open an energy gap in graphene. Subsequently, a whole new class of 2D materials has been studied and prepared in experiment, such as the transition metal dichalchogenides, transition-metal carbides (MXenes), monolayer black phosphorus (1L-BP) (termed as phosphorene), etc. More importantly, the electronic and optoelectronic properties can be modulated through a variety of ways, such as doping, point and line defects, layer-by-layer, or hetero-structures mapping, chemical adsorption, strain, and external electric field, further broadening its widespread applications in optoelectronic devices, such as light-emitting diodes, field effect transistors, and solar cells.

Current Results

In project hbp00027, we mainly employ density-functional theory and many-body methods to investigate structural, electronic, optical properties and exciton dynamics of siligraphene and phosphorene-based heterostructures. Up to now, we have mainly finished two works: (1) the electronic, mechnamic and optical properties of novel g-SiC_7 siligraphene; (2) the electronic structure, charge transfer, optoelectronic properties, as well as exciton carrier dynamic of phosphorene-TiO_2 heterostructures.

- **g-SiC_7 siligraphene**

The stoichiometry and bonding structure of the 2D Si-C monolayers can greatly affect the electronic properties of siligraphene. For example, with the same stoichiometry, pt-SiC_2 shows metallic but g-SiC_2 is a semiconductor due to their different bonding structures [1]. From graphene to 2D-SiC, the band gap of siligraphene can vary in the range of 0−3 eV, independent of the increasing content of silicon. Among them, the g-SiC_2 has exhibited great potential as novel donor materials in excitonic solar cells [2]. And another siligraphene, g-SiC_3 can serve as topological insulators (TIs) superior to graphene [3].

Based on the previous investigations, we find thata novel stable-existed siligraphene g-SiC_7 also shows remarkable optoelectronic properties. The structure, stability, electronic and optical properties of g-SiC_7 have been exploited based on *ab initio* calculations. Such a g-SiC_7 siligraphene is a semiconductor with a direct band gap of 1.13 eV(Table 1), which can be easily tuned by applying biaxial strain or perpendicular electric field.

Table 1: Comparison of the symmetry, binding energy, band gaps, optical band gaps ($\mathbf{E_g^{opt}}$), as well as exciton binding energy of graphene, silicene, single-layered SiC (SL-SiC) and the reported siligraphenes. The exciton binding energy is defined as the difference between the energy of the optical band gap and the quasiparticle band gap.

	Symmetry Group	Binding energy (eV/atom)	Band gap (eV)	E_g^{opt} (eV)	Exciton binding energy (eV)
Graphene	P3m1	8.66	0	NA	NA
g-SiC_7	P-6m2	7.07	0.76[a] 1.13[b] 1.55[c]	1.0	0.55
g-SiC_3	P6/mmm	6.70	0	NA	NA
g-SiC_2	P6□2m	6.46	0.60[a] 1.09[b] 1.38[c]	0.75	0.65[7]
SL-SiC	P-6m2	5.99	2.56[a] 2.90[b] 4.42[c]	3.25	1.17[37]
Silicene	P3m1	3.93	0	NA	NA

[a, b, c] Calculation results based on PBE, HSE06 and G_0W_0, respectively. Data of g-SiC_2[7]and SL-SiC[37] are obtain from relevant references.

The direct band gap of 1.13 eV of g-SiC_7 siligraphene indicates a preferable efficiency of light absorption. The light absorbance with electron-hole interaction obtained via GW plus Bethe-Salpeter equation (GW + BSE) is shown in **Figure 1**. Such g-SiC_7 siligraphene has an enhanced light absorbance with an average value beyond 10% on near infrared and visible photon energies in the 0.7–3.0 eV range of key relevance for photovoltaics. The superior light absorbance against the sunlight can be apparently inferred by the more overlap with solar flux than phosphorene, as depicted in **Figure 1**. The calculated absorbed Photon Flux J_{abs} in g-SiC_7 siligraphene is 4.64 mA/cm^2, obviously larger than that in g-SiC_2 siligraphene (4.06 mA/cm^2) and phosphorene (3.15 mA/cm^2), and also larger than the reported graphene and transition metal dichalcogenides (TMDs) monolayers (2–4.5 mA/cm^2). The extraordinary adsorption performance to sunlight suggests g-SiC_7 siligraphene a promising donor material for the photovoltaics applications.

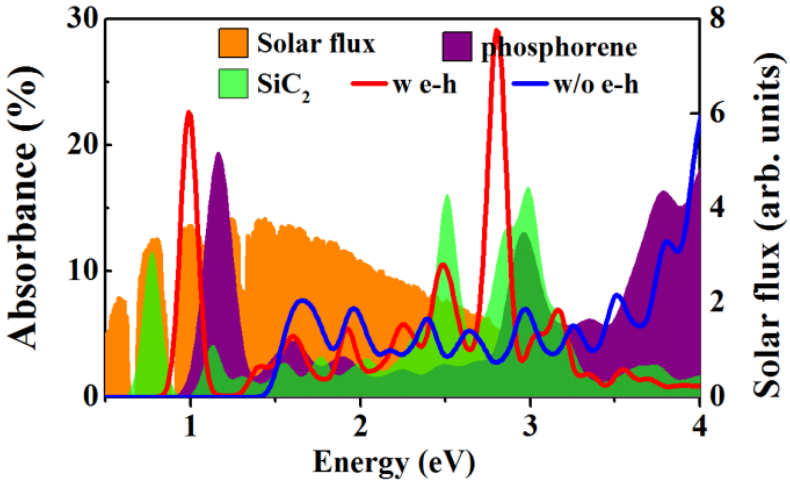

Figure 1: The absorbance spectrum of g-SiC_7 siligraphene (with and without electron-hole interaction), g-SiC_2 siligraphene, as well as phosphorene (along the armchair direction), overlapped to the incident AM1.5G solar flux.

- **Phosphorene/TiO2 heterostructures**

Phosphorene, has demonstrated extraordinary properties, including its highly anisotropic effective masses, high electron mobility (> 1000 $cm^2/V{\cdot}s$), a direct band gap of ~2.0 eV, significantly remedies graphene's shortcoming in optoelectronic devices. Considering the fact that van der Waals (vdW) heterostructure formed by stacking 2D atomic monolayers is one of the best approaches to protect the active layers against environmental contamination without affecting their electrical performance, or to modulate the band offsets at the interfaces, which provides a highly effective approach for the manipulation of charge carriers. The type-II band alignment between interfaces is a prerequisite to achieve the efficientelectron-hole pairs (excitons) separation, which has been achieved in various 2D layered transition metal dichalchogenides-, carbon- or silicon-based heterostructures.

By utilizing the large-scale density functional theory and GW + Bethe-Salpeter equation (BSE) calculations, we first systemically investigate the heterostructure consisting ofphosphorene monolayer interfaced with TiO_2 (110) surface (1L-BP/TiO_2) (Figure 2). 1L-BP/TiO_2shows a type-II band alignment, and large built-in potential for carrier separation. The constructed XSC based on 1L-BP-TiO_2 possesses a PCE of about 1.5% and ultrahigh power density of ~16.7 MW/L at the atomical level, dozens of times higher than conventional GaAs (290 kW/L) and Si (5.9 kW/L) solar cells, and comparable with MoS_2/WS_2 XSC. Nonadiabatic molecular dynamics simulation provides important insights into the charge separation and electron−hole recombination processes, showing an ultrafast electron transfer time, and slow electron−hole recombination time (Figure 3), and further guaranteeing the practical PCE. Moreover, doping in phosphorene layer has a tunability on built-in potential, charge transfer, light absorbance, as well as electron dynamics.

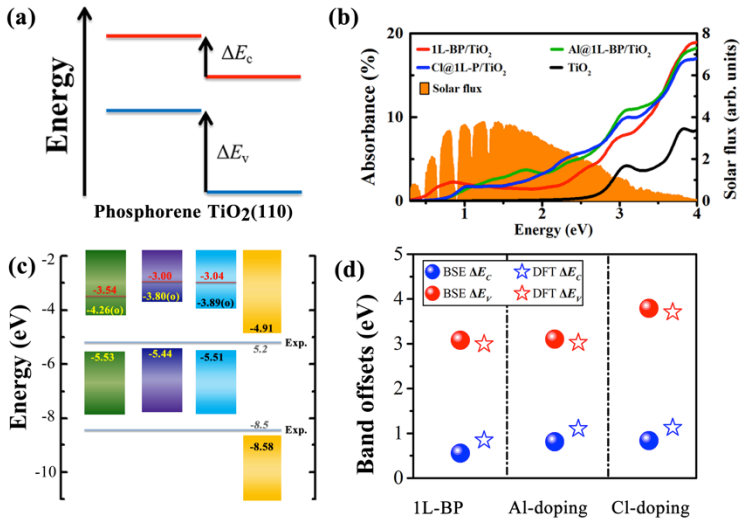

Figure 2: (a) Schematic type-II Band alignment at the 1L-BP/TiO_2(110) interface. (ΔEV) and ΔECare referred to Valence and conduction band offsets. (b) Absorbance of threeheterostructures, 1L-BP/TiO_2, Al- and Cl@1L-BP/TiO_2, as well as TiO_2(110) surface, overlapped to the incident AM1.5G solar flux. (c) Variation of VBM and CBM with respect to the vacuum level for phosphorene layers from G_0W_0 (red) and G_0W_0plus BSE (GW+BSE)(“o”) calculations, as well as for the TiO_2 structures from HSE06. Gray lines: experimentalVBM and CBM energies. (d) VB offsets (ΔEV) and CB offsets (ΔEC) based on GW+BSE and DFT calculations.

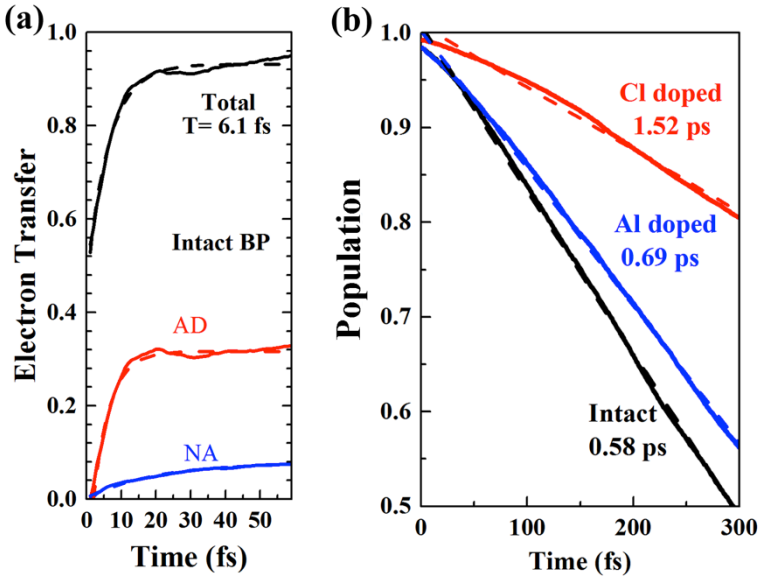

Figure 3: (a) Electron transfer dynamics of photoexcited states phosphorene. The solidblack, red and blue lines represent the total adiabatic and nonadaiabatic electron transfer. Thee total, adiabatic (AD) and nonadiabatic (NA) ET are indicated by the black solid, red solid and blue solid lines, respectively. The dashed lines show the exponential fits ofeach line. (b) Electron-hole recombination dynamics from phosphorene CBs to TiO_2VBM. Intact, Al- and Cl-doped interfaces are indicated in solid black, blue, red lines, respectively. The dashed lines are fitted by linear functions.

Outlook

These extraordinary sunlight absorptionof g-SiC_7 and tunable optical band gap, type-II interface band alignment, as well as PCE in 1L-BP/TiO2 heterostructures, enable siligraphene- and phosphorene-based heterostructures being promising for next-generation flexible optoelectronic devices. Our results presented here may stimulate further efforts on the rational design of future solar cell devices based on the combinations of 2D materials and 3D wide band gap semiconductors.

Publications

1. Li, Y.; Li, F.; Zhou, Z.; Chen, Z. SiC_2 Siligraphene and Its One-Dimensional Derivatives: Where Planar Tetracoordinate Silicon Happens. J. Am. Chem. Soc., 2011, 133, 900–908
2. Zhou, L. J.; Zhang, Y. F.; Wu, L. M. SiC_2 Siligraphene and Nanotubes: Novel Donor Materials in Excitonic Solar Cell. Nano Lett., 2013, 13, 5431–5436.
3. M. Zhao and R. Zhang, Two-dimensional topological insulators with binary honeycomb lattices: SiC_3 siligraphene and its analogs. *Phys. Rev. B*, 2014, 89, 195427
4. Dong, H.; Zhou, L.; Frauenheim, T.; Hou, T.; Lee, S.T.; Li, Y. SiC_7 Siligraphene: Novel Donor Material with Extraordinary Sunlight Absorption. Nanoscale, 2016, 8, 6994-6999.
5. Liu, P.-F.; Zhou, L.; Frauenheim, T.; Wu, L.-M. New Quantum Spin Hall Insulator in Two-Dimensional MoS_2 with Periodically Distributed Pores. Nanoscale, 2016, 8, 4915–4921.
6. Zhou, L.**;** Kou, L.; Sun, Y.; Felser, C.; Hu, F.; Shan, G.; Smith, S. C.; Yan, B.; Frauenheim, T. New Family of Quantum Spin Hall Insulators in Two-Dimensional Transition-Metal Halide with Large Nontrivial Band Gaps. *Nano Lett.,* 2015, *15,* 7867–7872.

Presentations

L. Zhou, *Black Phosphorus (BP) Interfaced with TiO_2(110) Surface: An Novel Photovoltaic Heterojunction,* Conference on Atomic structure of nanosystems from first-principles simulations and microscopy experiments (AS-SIMEX 2015), Helsinki, Finland, June 10, 2015

Support

The research was supported by the University of Bremen.